



This is to certify that the

# thesis entitled Factors Controlling The Occurrence And Distribution Of Hematite And Goethite In Soils And Saprolites Derived From Schists And Gneisses In Western North Carolina presented by

Debra Sue Bryan

has been accepted towards fulfillment of the requirements for

M. S. degree in Geology

Department Of Geological Sciences

Muchas tother Weller

Date July 10, 1994

O-7639

MSU is an Affirmative Action/Equal Opportunity Institution

## LIBRARY Michigan State University

PLACE IN RETURN BOX to remove this checkout from your record.
TO AVOID FINES return on or before date due.

The service delie due,			
DATE DUE	DATE DUE	DATE DUE	
MSI Je An Affirmethio Anti			

MSU is An Affirmative Action/Equal Opportunity Institution characteristics.pm3-p.1

## FACTORS CONTROLLING THE OCCURRENCE AND DISTRIBUTION OF HEMATITE AND GOETHITE IN SOILS AND SAPROLITES DERIVED FROM SCHISTS AND GNEISSES IN WESTERN NORTH CAROLINA

Ву

Debra Sue Bryan

#### A THESIS

Submitted to
Michigan State University
in partial fulfillment of the requirements
for the degree of

MASTER OF SCIENCE

Department of Geological Sciences

1994

#### ABSTRACT

FACTORS CONTROLLING THE OCCURRENCE AND DISTRIBUTION OF HEMATITE AND GOETHITE IN SOILS AND SAPROLITES DERIVED FROM SCHISTS AND GNEISSES IN WESTERN NORTH CAROLINA

By

#### Debra Sue Bryan

Controls on the occurrence and distribution of hematite and goethite near Otto, North Carolina were identified by determining the interrelationships between climatic, geologic and pedologic factors of first- and second-order watersheds and the redness ratings of their soils and saprolites. Hematite has formed from almandine garnet and magnetite. Goethite has formed from almandine garnet, hornblende, chlorite, and biotite. Soil maturity and temperature control hematite and goethite proportions in soils of watersheds underlain by a single rock formation. Percent total carbon in soils and parent rock differences control hematite and goethite proportions in soils of watersheds underlain by two rock formations. Precipitation, temperature, and local variations within rock formations control hematite and goethite proportions in multiple watersheds underlain by the same formation. Greater amounts of precipitation, milder temperatures, increased parent rock stability, and larger primary mineral size render the soils of the Coweeta Basin more goethitic than nearby North Carolina study areas.

#### **ACKNOWLEDGEMENTS**

I am grateful for the guidance and support of M. Velbel, S. Anderson, and R. Schaetzl, the assistance of D. Schulze, S. Flegler, D. Mokma, C. Basso, W. Swank and the staff at Coweeta, and the patience and understanding of my husband and family. This study was funded in part by a grant from the Clay Minerals Society.

#### TABLE OF CONTENTS

Introduction	1
Study Area	3
Study Design	6
Chapter 1. WEATHERING OF IRON-BEARING MINERALS	8
Review	8
Methods	13
Results	15
Discussion	28
Summary	39
Chapter 2. Distribution and Occurrence of Hematite and	d
Goethite.	42
Review	42
Methods	45
Results	47
Discussion	49
Summary	53
Chapter 3. General Discussion	54
Chapter 4. Conclusions	64
Appendix	67
List of References	118

#### LIST OF TABLES

Table 1.	Environmenatal Variables At Each of the Nine	
	Study Sites.	67
Table 2.	Parent Rock Point Count Data.	68
Table 3.	Soil pH.	70
Table 4.	Total Soil Carbon.	70
Table 5.	Soil Particle Size Analyses.	71
Table 6.	Soil Munsell Colors.	72
Table 7.	Redness Ratings of NaOH-treated Clays.	73
Table 8.	Goethite and Hematite in the Blue Ridge	
	Front Study Area.	73
Table 9.	Comparison of the Coweeta Basin and Blue	
	Ridge Front Study Areas.	74

#### LIST OF FIGURES

Study Area and Sample Site Locations.	75
Embayed, Inclusion-rich Garnet Grain with	
Radial Fractures Around Quartz Inclusions	
(# 2A92).	76
Continuous Surface Layers Around Euhedral	
Inclusion-poor Garnet Grains (# 36A92).	76
Fractures Formed In Garnet As A Result of	
Directed Pressure (# 17A92).	77
Garnet Weathering In Contact with Biotite.	
(Fractures Formed as A Result of Directed	
Pressure. # 2A92)	77
Limonitic Surface Layer In Contact with	
Garnet Remnant (# C80-2-4-4).	78
Embayed, Inclusion-rich Garnet Grain	
Weathering In Contact with Chlorite	
(# 34B92).	78
Limonitic Surface Layer Not In Contact with	
Garnet Remnant (# C80-2-4-4).	79
Limonitic Pseudomorph After Garnet	
(# C80-2-4-4).	79
"Onion skin-like Appearance of Type 1	
Protective Surface Layers On Garnet.	80
Garnet Type 2 Surface Layer.	80
	Continuous Surface Layers Around Euhedral Inclusion-poor Garnet Grains (# 36A92).  Fractures Formed In Garnet As A Result of Directed Pressure (# 17A92).  Garnet Weathering In Contact with Biotite.  (Fractures Formed as A Result of Directed Pressure. # 2A92)  Limonitic Surface Layer In Contact with Garnet Remnant (# C80-2-4-4).  Embayed, Inclusion-rich Garnet Grain Weathering In Contact with Chlorite  (# 34B92).  Limonitic Surface Layer Not In Contact with Garnet Remnant (# C80-2-4-4).  Limonitic Pseudomorph After Garnet  (# C80-2-4-4).  "Onion skin-like Appearance of Type 1

Figure	12.	Close View of Garnet Type 2 Surface Layer	
		Showing Microporosity.	81
Figure	13.	Inner Surface of A Garnet Grain with A Type	2
		Surface Layer.	81
Figure	14.	Strong Parallelism In Etch Pits and Product	
		"Casts" On Garnet.	82
Figure	15.	Dodecahedral Etch Pits On Garnet.	82
Figure	16.	Etch Pits Covered By Secondary Products On	
		Garnet.	83
Figure	17.	Elongate Strings On Garnet.	83
Figure	18.	Mammillated Surfaces On Garnet.	84
Figure	19.	Boxwork and Central Partings On Garnet.	84
Figure	20.	Boxwork and Faceted Surfaces On Garnet.	85
Figure	21.	Boxwork and Lace-like Secondary Products	
		On Garnet.	85
Figure	22.	Boxwork and Void Space On Garnet Grains	
		Removed From the Upper Horizons.	86
Figure	23.	Lace-like Secondary Products On Garnet.	86
Figure	24.	Spheroidal Secondary Products Forming	
		Boxwork Septa On Garnet.	87
Figure	25.	External and Internal Structure of	
		Spheroidal Secondary Products On Garnet.	87
Figure	26.	Skeletal Secondary Products Forming	
		Fracture Fillings On Garnet.	88
Figure	27.	X-ray Diffraction Pattern of Garnet From	
		Site 36A.	89

## viii

Figure 28.	X-ray Diffraction Pattern of Garnet From	
	Site 18B.	90
Figure 29.	EDS Spectra of Garnet.	91
Figure 30.	EDS Spectra of Garnet.	91
Figure 31.	EDS Spectra of Garnet.	92
Figure 32.	EDS Spectra of Garnet.	92
Figure 33.	Vuggy Surface Layer On Magnetite.	93
Figure 34.	Exsolution Lamellae On Magnetite.	93
Figure 35.	Exsolution Lamellae On Magnetite.	94
Figure 36.	Exsolution Lamellae On Magnetite.	94
Figure 37.	Exsolution Lamellae On Magnetite.	95
Figure 38.	Exsolution Lamellae On Magnetite.	95
Figure 39.	Leaf-like Secondary Products	
	On Magnetite.	96
Figure 40.	Lace-like Secondary Products	
	On Magnetite.	96
Figure 41.	Coated Magnetite Grain.	97
Figure 42.	EDS Spectra of Magnetite.	97
Figure 43.	X-ray Diffraction Pattern of Chlorite.	98
Figure 44.	X-ray Diffraction Pattern of Biotite.	99
Figure 45.	EDS Spectra of Chlorite.	100
Figure 46.	EDS Spectra of Biotite.	100
Figure 47.	X-ray Diffraction Pattern of Pyribole.	101
Figure 48.	EDS Spectra of Amphibole.	102

Figure 49	. Schematic Representation of Garnet	
-	Weathering In Contact with Iron-rich	
	•	103
Figure 50	. Schematic Representation of Garnet Weatheri	na
	-	103
Figure 51	. Schematic Representation of Embayed,	
rigure 31	•	104
	_	104
Figure 52	. Schematic Representation of Type 1 Surface	
	Layer and Peripheral Void Space	
	Formation.	104
Figure 53	. Etch Pits Under Type 1 Protective Surface	
	Layer On Garnet.	105
Figure 54	. X-ray Diffraction Pattern of Untreated Clay	s
	From the Middle Horizons of Site 2A.	106
Figure 55	. X-ray Diffraction Pattern of Untreated Clay	s
	From the Saprolite of Site 2B.	107
Figure 56	. X-ray Diffraction Pattern of NaOH-treated	
	Clays From the Middle Horizons	
	of Site 17A.	108
Figure 57	. X-ray Diffraction Pattern of NaOH-Treated	
-	Clays From the Saprolite of Site 2A.	109
Figure 58	. X-ray Diffraction Pattern of NaOH-Treated	
	Clays From the Middle Horizons of	
	-	• • •
	Site 36A.	110

Figure 5	9.	X-ray Diffraction Pattern of NaOH- and DCB	_
		Treated Clays From the Middle Horizons	
		of Site 17A.	111
Figure 6	0.	X-ray Diffraction Pattern of NaOH- and DCB	-
		Treated Clays From the Saprolite	
		of Site 2A.	112
Figure 6	1.	X-ray Diffraction Pattern of NaOH- and DCB	-
		Treated Clays From the Middle Horizons	
		of Site 36A.	113
Figure 6	2.	Redness Ratings vs. Aspect.	114
Figure 6	3.	Redness Ratings vs. Percent Clay.	114
Figure 6	4.	Redness Ratings vs. pH.	115
Figure 6	5.	Redness Ratings vs. Mean Annual	
		Precipitation.	115
Figure 6	6.	Redness Ratings vs. Elevation.	116
Figure 6	7.	Redness Ratings vs. Percent Total Carbon.	116
Figure 6	8.	Redness Ratings vs. Percent Slope.	117

#### INTRODUCTION

The factors controlling the occurrence and distribution of hematite and goethite under laboratory conditions have been well documented. Changes in pH, organic matter content, temperature, moisture content, and aluminum activity affect the stabilities of hematite and goethite, and therefore their relative proportions in soils and saprolites (Langmuir, 1971; Fischer and Schwertmann, 1975; Schwertmann and Murad, 1983; Torrent et al., 1983; Yapp, 1983; Schwertmann, 1988; Schwertmann and Taylor, 1989). Field studies of hematite and goethite occurrences have been largely concentrated in the southern hemisphere and/or arid climates where red beds and oxidic soils are common (Nahon et al., 1977; Torrent et al., 1980; Kämpf and Schwertmann, 1982b; Campbell and Schwertmann, 1984, Fitzpatrick, 1988). Exceptions are studies in the North Carolina Blue Ridge Front (Graham et al., 1989a, b; 1990a, b) and in the North Carolina Piedmont (Calvert et al., 1980; Buol and Weed, 1991).

Goethite occurring within the Piedmont is derived from the weathering of biotite, opaques, and ferromagnesian minerals (Calvert et al., 1980; Buol and Weed, 1991). Where in situ (residual) weathering predominates, both hematite and goethite can form from iron-bearing primary minerals (Calvert et al., 1980; Buol and Weed, 1991).

Graham et al. (1989a, b; 1990a, b) found that in the Blue Ridge Front, magnetite and almandine garnet weather to hematite. Hematite abundance and distribution in the Blue Ridge Front are controlled by the presence of almandine garnet in the parent material. Almandine garnet in the Blue Ridge Front also weathers to goethite and gibbsite (Graham et al., 1989a, b; 1990a, b). Redness ratings (Torrent et al., 1983) of the soils in the Blue Ridge Front directly correlate with the amount of hematite in the soils.

Previous North Carolina studies (Calvert et al., 1980; Graham et al., 1989a, b; 1990a, b; Buol and Weed, 1991) did not determine whether the factors that affect hematite and goethite occurrences under laboratory conditions also affect their occurrences in nature.

The purpose of this study is to document the environmental conditions and the hematite and goethite distributions of several sample sites within a North Carolina study area, and to determine their interrelationships, if any. The study has two parts. The goal of the first is to determine the parent rock mineralogy and to determine the weathering products of primary iron-bearing minerals. The goal of the second is to determine the hematite and goethite distributions and their relationship to the climatic, geomorphic, pedologic and geologic conditions of each sampling site.

#### STUDY AREA

The study area is located within the Coweeta Creek Basin of the Coweeta Hydrologic Laboratory, Otto, North Carolina and lies in the Nantahala Mountain Range of the Blue Ridge Physiographic Province. The Coweeta Hydrologic Laboratory is an outdoor forest ecology and hydrology research site established in 1932 by the U. S. Forest Service. Elevations range from 675 m (2214 ft) to 1592 m (5223 ft). The Coweeta Basin is east-facing, bowl-shaped and drained by two fourth-order streams which join to form Coweeta Creek (Swank and Crossley, 1988). Stream hydrologic data are available from 1938 to present. The hydrologic data indicate that stream response in the Coweeta Basin is controlled by watershed elevation, precipitation amount and timing of the precipitation events (Swift, et al., 1988). Precipitation data (Climate Station 01, elevation 685 m) have been continuously recorded since 1934; air and soil temperature, relative humidity, wind travel, evaporation, and cloud cover have been collected since 1936. Average annual precipitation at Climate Station 01 (CS01) is 1652 mm; average annual temperature is 12.6 °C with extreme monthly averages of 23.0 °C and -4.0 °C (Swift et al., 1988). Climate in the higher elevations of Coweeta is classed as Marine, Humid Temperate (Cfb) due to high precipitation and cool temperatures. Lower elevations alternate between Marine and Humid Subtropical climates. Precipitation increases with elevation (highest elevations

are at the western edge of the Coweeta Basin), and average annual precipitation exceeds average annual evapotranspiration throughout the entire basin (Swift, et al., 1988; Buol and Weed, 1991).

The Coweeta Hydrologic Laboratory is underlain by rock units which were metamorphosed during the middle Paleozoic to the staurolite-kyanite subfacies (lower-middle amphibolite facies). The geologic structure of Coweeta is composed of two early thrust faults, Shope Fork and Soque River thrusts, which were later refolded by northeast-trending, isoclinal folds. The Coweeta Basin is overlain by Quaternary colluvial deposits which move downslope both as debris avalanches and in creeping, intact masses (Hatcher, 1988).

Three major rock formations underlie the Coweeta Basin: the Tallulah Falls Formation (biotite paragneiss and biotite schist), the Coweeta Group (quartz-diorite gneiss, biotite-garnet schist, metasandstones and quartz-feldspar gneiss), and the Carroll Knob Ultramafic Complex (amphibolite and hornblende gneiss). The Tallulah Falls Formation members are coarse-grained rock units which contain quartz, plagioclase, orthoclase, biotite, muscovite, garnet, sillimanite, and minor amounts of zircon, epidote, and opaque minerals (Hatcher, 1980). The Carroll Knob Ultramafic Complex units are predominantly amphibolite and hornblende gneiss, with some metadiorites, dunites and metagabbros (Hatcher, 1980). Garnet-bearing amphibolites occur but are not common (Hatcher, 1980).

The Coleman River Formation was the only member of the Coweeta Group examined in this study. The Coleman River Formation is predominantly metasandstone and quartz-feldspar gneiss with some interlayered pelitic schist and calcsilicate quartzite. The Coleman River Formation contains quartz, plagioclase, staurolite, kyanite, green and brown biotite, epidote, chlorite after biotite, garnet, and minor amounts of epidote, clinozoisite, hornblende, opaque minerals, zircon and magnetite (Hatcher, 1980).

Soils of the Coweeta Basin are either Inceptisols or older, more developed Ultisols (Swank and Crossley, 1988). The soil temperature regime is mesic, the soil moisture regime is udic, and soil textures range from fine/coarse loamy, micaceous to fine/coarse loamy, mixed (Browning and Thomas, 1985). Most Coweeta soils are either well- or extremely well-drained. Umbric Dystrochrepts, Typic Dystrochrepts and Typic Haplumbrepts (Inceptisols) occur at high elevations on steep, rocky north- and south-facing aspects, on south-facing slopes underlain by the Tallulah Formation, and on colluvium in hollows and coves, respectively. Ultisols have formed in residuum of weathered schists and gneisses and include Typic Hapludults and Humic Hapludults. Typic Hapludults are the most prevalent soil type at Coweeta and are found on sloping ridges and sideslopes. Humic Hapludults are found on cooler, steep, northfacing slopes (Swank and Crossley, 1988).

The Coweeta Basin has a number of first- and secondorder watersheds. Control watersheds are paired with other watersheds which have been manipulated by the U. S. Forest Service to determine the impact of planned anthropogenic disturbances such as prescribed burns, logging, grazing, and vegetation alteration (Swank and Crossley, 1988). Control watersheds have remained undisturbed since 1932 and are covered with mixed hardwood stands.

#### STUDY DESIGN

Seven sample sites from four control watersheds (#2A, 2B, 18A, 18B, 34A, 34B, and 36A) and two sample sites from disturbed watersheds (#1A and 17A) were selected for study (Figure 1). Primary iron-bearing minerals were sampled from the >1 mm fraction of the saprolite (>60 cm in depth), the upper (0 - 10 cm in depth) and the middle soil horizons (17 - 60 cm in depth) of each sample site. The primary iron-bearing minerals were identified and analyzed with energy dispersive spectroscopy, X-ray diffractometry, light microscopy, and scanning electron microscopy to determine the degree of weathering, the weathering textures and the weathering products of each mineral. Secondary iron-bearing and clay minerals in the <2  $\mu$ m fraction were analyzed with X-ray diffractometry.

A description of each sample site is given in Table 1. Sample sites were chosen so that a range of environmental variables (pH, percent total carbon, average annual precipitation, soil color, particle size, percent slope, aspect, vegetation cover, parent rock type and parent rock

mineralogy), on both disturbed and undisturbed watersheds, could be measured and their interrelationships with hematite and goethite distributions determined.

#### CHAPTER 1

#### WEATHERING OF IRON-BEARING MINERALS

#### REVIEW

There has been much research in the field of chemical weathering during the last few decades. Early workers utilized "batch" or "open" laboratory experiments in which minerals were exposed to various solutions to determine chemical weathering pathways. These experiments resulted in the formation of the hypothesis that chemical weathering rates are governed by diffusion of reactants through a "leached" or "protective surface" layer (Correns and Von Englehardt, 1938, in Banfield and Eggleton, 1988; Wollast, 1967; Helgeson, 1971, 1972; Luce et al., 1972). Reactions whose rates are limited by diffusion or advection through a "leached" layer are said to be transport-limited reactions. Reactions which are governed by the rate at which ions detach from the mineral surface during dissolution are said to be surface- or interface-limited. Dissolution in mixed kinetic regimes is intermediate between these two extremes (Berner, 1978; 1981). Workers who observed naturally weathered minerals with scanning electron microscopes failed to find evidence of "leached" or "protective surface" layers. Instead "well-formed corrosion figures" (Tchoubar, 1965, in Wilson, 1975) or "etch pits" (Wilson, 1975) were observed. The presence of etch pits on the surfaces of

naturally weathered minerals supported mineral dissolution by interface-limited reactions (Wilson, 1975; Berner and Holdren, 1977; 1979; Berner, 1978; Holdren and Berner, 1979; Berner et al., 1980; Berner and Schott, 1982; Lasaga and Blum, 1986). One exception was noted by Velbel (1984a) who observed that naturally weathered almandine garnet can undergo both transport-limited and interface-limited reactions depending on environmental conditions. Velbel has since (1993) determined that protective surface layers can only form if: 1) immobile elements (Al, Fe) behave conservatively; and 2) the volume of products formed during weathering are greater than the volume of reactants. conditions are necessary to ensure that the amount of products formed is sufficient for continuous, non-porous surface layers to form on the surface of weathering mineral crystals.

The chemical weathering studies relevant to this study are those of almandine garnet, magnetite, biotite, chlorite, amphibole, pyroxene, and epidote. Biotite weathering may produce interstratified biotite and vermiculite, interstratified chlorite and vermiculite, vermiculite, kaolinite, and goethite (Walker, 1949; Coleman et al, 1963; Wilson, 1966; 1970; Meunier and Velde, 1979; Gilkes and Suddhiprakarn, 1979; Velbel, 1985; Banfield and Eggleton, 1988). Banfield and Eggleton (1988) determined that biotite weathering occurs in a two stage process: 1) removal of K<sup>+</sup> and addition of water to form interstratified biotite and vermiculite without an overall volume increase, and 2) the formation of kaolinite-goethite with an estimated 20% volume

increase. Velbel (1985) determined that biotite grains of the same composition weather at different rates in different parent materials and estimated that a minimum of 140,000 years would be required to alter all the biotite in 20 ft. (depth) of metamorphic rock to hydrobiotite (interstratified biotite/vermiculite).

Chlorite weathers to vermiculite by transformation reactions and to goethite by oxidation of ferrous iron (Gilkes and Little, 1972; Bain, 1972; Bain, 1977; Churchman, 1979; Anand and Gilkes, 1984a). Bain (1972) observed that chlorite persists in all horizons of the soils in Argyllshire, Caithness and the Southern Uplands of Scotland. In these locations, chlorite weathering is limited to oxidation of ferrous iron and transformation to vermiculite near grain edges. In the soils of the Loch Awe region of Scotland, however, chlorite does not persist in the  $A_2$  horizon (Bain, 1977). Bain (1977) theorized that chlorite is dissolved from the  $A_2$  horizon by percolating organic solutions which form complexes with the iron and aluminum in the chlorite structure and remove them to the B horizon.

Almandine garnet weathering produces gibbsite, goethite, and hematite (Embrechts and Stoops, 1982; Velbel, 1984a; Graham et al., 1989a, b). Velbel (1984a) noted that the weathering of almandine garnet in the oxidized vadose zone of soils and saprolites is transport-limited due to the presence of continuous, non-porous protective surface layers which form on garnet surfaces. Etch pits are absent on grains with protective surface layers (Velbel, 1984a). In the rooting zone of soils, protective surface layers do not

form and pre-existing layers are dissolved due to biochemical processes (Embrechts and Stoops, 1982; Velbel, Biochemical processes in this environment also cause almandine garnets to undergo interface-limited reactions which produce etch pits (Velbel, 1984a; Hansley 1987), and therefore weathering occurs at a faster rate (Velbel, 1984a). In laboratory studies, Hansley (1987) noted that the presence of oxalate in both low and neutral pH solutions produced etch pits and faceted surfaces on garnet within six days of exposure. After fourteen days, low pH solutions of humic acids produced "ragged edges" on garnet but neither etch pits nor faceted surfaces (Hansley, 1987). Both Velbel (1984a) and Embrechts and Stoops (1982) observed that almandine garnet weathering below the rooting zone begins at grain boundaries and along fractures, and proceeds by centripetal replacement until only a pseudomorph of iron and aluminum oxides remains. The fractures exploited by chemical weathering processes originate near inclusions (Wendt et al., 1992; Embrechts and Stoops, 1982). Ghabru et al. (1989) identified other almandine garnet weathering surface features including several different etch pit morphologies, mammillated surfaces, elongate strings, and hillocks. Ghabru et al. (1989) also identified a curled, vein-like secondary product which is thought to be a primitive clay precursor similar to that reported by Tazaki and Fyfe (1987).

Magnetite weathering produces hematite (martite) and maghemite (Gilkes and Suddhiprakarn, 1979; Morris, 1980; Anand and Gilkes, 1984b). Gilkes and Suddhiprakarn (1979)

and Anand and Gilkes (1984b) observed that weathering of magnetite begins at grain boundaries and along internal fractures and proceeds until a porous, hematitic pseudomorph is formed. Graham et al. (1989a) observed that magnetite in the saprolite is unaltered, but is coated with oxidation crusts and etched in the soil. Velbel (1993) predicted that magnetite weathering directly to hematite could form a protective surface layer if the iron behaved conservatively.

Amphibole and pyroxene weathering textures are varied and complex. Amphibole can alter to chlorite, biotite and other silicates (Nesse, 1986). In well-leached weathering environments, amphibole and pyroxene dissolve stoichiometrically which ultimately results in cleavage-parallel, lenticular etch pits, and denticulated terminations (Berner and Schott, 1982; Velbel, 1989). Denticulated terminations on hornblende remnants occur within peripheral voids formed by ferruginous microboxwork (Velbel, 1989). Hornblende weathering produces goethite, gibbsite, and kaolinite by dissolution-reprecipitation reactions (Velbel, 1989).

The mechanisms and products of epidote weathering have not been reported in previous studies.

The purpose of this portion of the study is to characterize further the aspects of amphibole, pyroxene, epidote, almandine garnet, magnetite, biotite and chlorite weathering at Coweeta Hydrologic Laboratory.

#### **METHODS**

#### Light Microscopy

Rock thin sections from outcrops at each soil/saprolite sample location and from other sites in the control watersheds were examined under a petrographic microscope.

Abundances of primary and accessory minerals were determined at 500 points on linear transects across each thin section.

Point count data are given in Table 2. Magnetite was first identified as an opaque mineral in thin section and later verified by energy dispersive spectroscopy and by magnetic properties. Weathering textures were photographed with a 35mm camera mounted to a petrographic microscope.

#### Scanning Electron Microscopy

Thirteen soil and saprolite samples were collected from the four undisturbed watersheds by hand-augering. Parent rock was collected from outcrops. Soil samples from deeply weathered saprolite (>60 cm in depth), from the upper horizons (0 - 10 cm in depth), and from one or two intermediate points in each profile were washed with deionized water through a 1 mm sieve. The >1 mm fraction was then dried at 60 °C. Garnet, magnetite (separated by hand magnet), pyribole, biotite and chlorite grains from the >1 mm fraction and from rock outcrops were hand picked under a binocular microscope. Both whole and fractured (by gentle crushing) grains were mounted to SEM stubs with SEM press-on adhesive tabs. SEM stubs were gold coated four minutes at 7

nm per minute with an Emscope sputter coater and examined in a JEOL JSM-35CF scanning electron microscope in the secondary electron imaging mode. Over 200 micrographs were taken of mineral weathering textures. Representative micrographs will be discussed later.

#### Energy Dispersive Spectroscopy

Energy dispersive spectroscopy (EDS) data on mineral grains were obtained using a JEOL JSM-35C scanning electron microscope equipped with an EDS detector. Samples were mounted to SEM stubs with SEM press-on adhesive tabs and carbon-coated. Spectra were obtained for 100 seconds with an average of 15 - 20% down time.

#### X-ray Diffractometry

Chlorite, biotite/muscovite, and pyribole grains were hand picked from the >1 mm fraction with the aid of a binocular microscope. Chlorite, biotite/muscovite, and pyribole grains from all sample sites were crushed in an agate mortar and mounted to glass slides with double-stick tape. Two to four garnet grains from the saprolite, the middle, and the upper horizons of each control watershed sample site were also crushed and mounted. X-ray diffraction data were obtained using CuKa radiation (35 kv, 20 mA) and a Philips goniometer equipped with a 1° divergence slit, a 0.2 mm receiving slit, a 1° scatter slit, and a graphite monochromator. Chlorite, biotite/muscovite, and pyribole samples were step-scanned from 2 to 62 °20 at 0.05 °20 steps using a counting time of 2 sec/step. Garnet

samples were step-scanned for various intervals at 0.05 20 steps using a counting time of 2 sec/step.

#### RESULTS

#### Garnet

#### Light Microscopy

Garnet grains from Coweeta exhibit a variety of textures and shapes in thin section. Garnet in thin section is often more weathered than epidote, pyroxene, biotite, and magnetite, and less weathered than hornblende and chlorite. Most garnet grains fall into one of the following categories:

- Embayed, highly fractured, and inclusion-rich grains that are larger than (poikiloblastic), or equal in size to the surrounding matrix (Figure 2);
- 2. Euhedral, inclusion-poor grains that are smaller than, or equal in size to the surrounding matrix (Figure 3); and
- 3. Euhedral to subhedral, highly fractured, inclusion-rich poikiloblasts.

Inclusions in garnet are (listed in order of decreasing abundances) quartz, magnetite, biotite, muscovite, chlorite and epidote. Many internal fractures originate near inclusions (Embrechts and Stoops, 1982) and radial fractures (Wendt et al., 1992) occur near some quartz inclusions (Figure 2). Other fractures occur across embayments and as

a result of directed pressure (Figures 4, 5). Fractures that form as a result of directed pressure occur on grains in rocks with strong preferred orientation and compositional banding. The fractures are perpendicular to foliation and are parallel to each other.

Limonitic surface layers have formed on most weathered garnet grains. Continuous surface layers are more prevalent on euhedral, inclusion-poor grains and on grains that are extremely weathered (Figures 3, 6). Discontinuous surface layers are more prevalent on embayed, inclusion-rich grains and on grains which border iron-rich mica (chlorite or biotite) (Figures 5, 7).

Orange, red and yellow-brown limonitic deposits form surface layers and form boxwork along internal fractures. On most garnet grains, limonitic boxwork and surface layers form three advanced weathering textures: 1) grains in which limonite is in contact with the garnet remnant (Figure 6); 2) grains in which limonite is not in contact with the garnet remnant (formation of a peripheral void around remnant) (Figure 8); and 3) grains in which limonite has formed a porous pseudomorph after garnet (Figure 9). In some thin sections, limonitic deposits occur in rock fractures and stain surrounding minerals, suggesting that some garnet weathering products are being transported away from garnet grain boundaries.

#### Scanning Electron Microscopy

The micromorphological aspects of garnet weathering at Coweeta appear to be dependent on both sample locality and

- depth. A summary of important micromorphological features of garnet weathering is given below.
  - 1. Surface Layers. Surface layers on garnet grains at Coweeta are divided into two types. The first (type 1) is continuous over the entire grain surface, has no microporosity perpendicular to grain surfaces, no microporosity parallel to grain surfaces in outcrop samples, and minor (0.8 - >5.0  $\mu$ m in width) microporosity parallel to grain surfaces in profile samples. Type 1 surface layers are thickest in the saprolite and decrease in thickness higher in the soil profile. Type 1 surface layers may become discontinuous, probably due to dissolution and abrasion. Type 1 surface layers have an "onion skinlike" appearance in which successive layers are deposited in contact with previous layers (Figure 10). The second surface layer (type 2) is continuous over the entire grain surface, has microporosity perpendicular to grain surfaces (pores of 8.0 - 10.0  $\mu$ m in diameter), and little or no microporosity parallel to the grain surface. Type 2 surface layers are thickest in the upper horizons and decrease in thickness lower in the soil profile (Figures 11, 12). Grains with type 2 surface layers occur only in watershed 2 sample site B.
  - Etch Pits. Etch pits occur on most garnet grains.
     Etch pits were not observed on garnets with type 2
     surface layers (Figure 13). Etch pits occur under type
     surface layers, under fracture fillings and on both

outer and inner (fractured for this study) grain surfaces. Etch pits increase in abundance higher in the soil profile. A limited number of grains have strong parallelism in etch patterns (Figure 14). Most etch pits are dodecahedral (Figure 15) except for a few isolated triangular etches on garnet grains sampled from watershed 34 sample site B and watershed 2 outcrop. Etch pits on grains from watershed 2 outcrop and sample site A, and watershed 34 sample site B are filled with a subsequent layer of secondary products (Figure 16).

- 3. Elongate Strings. Elongate strings (Ghabru et al., 1989) are dissolution textures which were observed in samples from the upper (site B) and middle (site A) horizons of watershed 18, and the middle horizons and saprolite of watershed 36 (Figure 17). Elongate strings coexist with etch pits, mammillated surfaces, and boxwork.
- 4. Mammillated Surfaces. Mammillated surfaces occur in the saprolite of watershed 34 sample site B, and the middle horizons of watershed 18 sample site A, watershed 2 sample site B (type 1 surface layers only), and watershed 34 sample site B (Figure 18).

  Mammillated surfaces coexist with etch pits, elongate strings, and boxwork.
- 5. Boxwork. Boxwork on garnet occurs in the saprolite the upper and the middle horizons of all sampled profiles. Minor boxwork also occurs in some outcrop samples. Boxwork formation on grains of the same size

occurs to different extents in different watersheds. Watershed 36 has only minor boxwork formation in the middle horizons, while watershed 2 sample sites A and B, and watershed 34 sample site A have advanced boxwork in saprolite (Figures 19, 20). The smaller grains of watershed 18, sample sites A and B, have advanced boxwork in the middle horizons. Boxwork can enclose secondary products, secondary products and void spaces (Figure 21), garnet fragments (Figure 19), or, in the most advanced state, void spaces only (Figure 22). Boxwork occurs first along grain boundaries and proceeds to interior regions via grain fractures. Boxwork can coexist with etch pits, mammillated surfaces, and elongate strings, but does not appear to form on garnets with type 2 surface layers.

- 6. Lace-like Secondary Products (Ghabru et al., 1989). Lace-like secondary products occur in the saprolite of watershed 34 sample site A, and the middle horizons of watershed 18 sample site B (Figures 21, 23). These features are very small (<1.0  $\mu$ m) and occur on relatively fresh, inner (fractured for study) surfaces.
- 7. Secondary Product Morphology. Secondary product morphologies vary widely. Spheroidal secondary products occur within boxwork (Figure 21) or form boxwork septa (Figure 24). The outer surface of the spheroids is composed of small (<1.0  $\mu$ m) interlocking crystals (Figure 25). The internal structure of the spheroids is made of radiating fibers which originate from a central point (Figure 25). Neither the internal

nor external structures are porous (Figures 24, 25). Spheroidal secondary product occurs on garnet grains with type 1 surface layers. Another non-porous secondary product morphology occurs predominantly as type 1 surface layers (Figure 10) and occasionally as boxwork septa (Figure 19). This secondary product is made of fibers oriented at right angles to the plane of the septa or surface layer (Figures 10, 19, 20, 22). Fibers forming boxwork septa appear to nucleate on preexisting microboxwork (Figure 19). It is not clear from the SEM studies if these two morphologies represent differing product compositions. Other, less prevalent, secondary product morphologies include: highly porous spheroidal aggregates which form type 2 surface layers and occur on inner surfaces of garnets in watershed 2 sample site B (Figure 11, 12); 2) skeletal, highly porous fracture fillings of outcrop samples (Figure 26); and 3) skeletal, microporous surface deposits of outcrop samples (Figure 16). 8. Other Features. Crystallographically-controlled facets occur on garnet surfaces in the saprolite of watershed 34 sample site A (Figure 20). Internal fractures lined with porous, skeletal secondary material intersect grain surfaces in the outcrop samples of watershed 2 (Figure 26). Growth terraces occur on most outcrop samples. Blocks of weathering products (Figures 14, 16) occur in the upper horizons of watershed 34 sample site B and in watershed 2 outcrop. The blocks formed when the garnet surface

that surrounded product-filled etch pits was fractured (for mounting) and removed, leaving the product "casts" exposed. Garnet grains from many sample locations contain euhedral quartz and magnetite inclusions.

#### X-ray Diffractometry

Crushed garnet from all sample locations provided X-ray diffraction patterns representative of end-member almandine (Figures 27, 28) (file #9-427, JCPDS, 1980). The (hkl) (211) peak is not detectable in pure end-member almandine garnet (file #9-427, JCPDS, 1980). The detection of (hkl) (211) peaks from two sample locations most probably reflects manganese (4.77 Å, site 34A) and magnesium (4.64 Å, site 18A) substitution (file #33-658 and 15-742, respectively, JCPDS, 1980). The 0.06 Å shift (to the left) of peak (hkl) (211) in the patterns obtained from sites 2A, 2B, 34B, and 18A may also reflect manganese substitution (file #33-658, JCPDS, 1980). This is consistent with the formula for Coweeta garnets reported by Velbel (1985), which was based on electron microprobe analyses. X-ray patterns indicate that garnet grains sampled from sites 36A, 18A, 34B, and 2B are more crystalline and therefore less weathered than garnet grains sampled from sites 34A, 2A and 18B (Figures 27, 28). Garnet grains from sample site 18B are the least crystalline and therefore the most weathered (Figure 28). Other peaks obtained indicate the presence of quartz (all sample sites), hematite (18B, 2B), gibbsite (2A), and goethite (34A, 34B, 36A, 18A, 18B).

#### **Energy Dispersive Spectroscopy**

EDS spectra of garnet grains contain large iron peaks representative of end-member almandine garnet and smaller manganese, magnesium, and calcium peaks indicating some elemental substitution (Figures 29 - 32). This is also consistent with findings of Velbel (1985). The chlorine and potassium peaks are due salt contamination and the presence of micaceous minerals, respectively.

#### Magnetite

#### Light Microscopy

Magnetite grains in thin section are most often anhedral, embayed, inclusion-poor and of equal size to the surrounding matrix. Less often, magnetite occurs as very small, euhedral inclusions in quartz, garnet and other primary minerals. Magnetite in thin section does not appear to be weathered.

#### Scanning Electron Microscopy

The micromorphological aspects of magnetite weathering textures are varied and largely independent of their location within the profile. Many grains from the upper horizons, for example, are entirely isolated from the surrounding soil by a layer of weathering mica. Often these grains have a less weathered appearance than grains exposed to their surroundings in the saprolite. Although earlier workers have reported that magnetite weathering is aided by the presence of internal fractures (Anand and Gilkes, 1984b), these were not observed. This is perhaps due to the

mechanical separation from surrounding mica, however, many grains were retrieved intact. Features of magnetite weathering include the following:

- Vuggy, pitted surface layers on grains 4 100 cm
   in depth from watersheds 2 sample sites A and B, 18
   sample sites A and B, and 34 sample site A (Figure 33),
- 2. Radiating, parallel, geometric, sheaf-like, and curved compositional lamellae on grains 0 100 cm in depth in watersheds 2 sample site A, 18 sample sites A and B, 36, and 34 sample site B (Figures 34 38 respectively),
- 3. Lace-like and leaf-like secondary products on relatively fresh, inner (fractured for study) surfaces on grains 30 120 cm in depth from watersheds 34 sample site B, and 2 sample site A (Figures 39 and 40 respectively), and
- 4. Thin coatings of weathering products on grains 17 111 cm in depth from all sampled locations (Figure 41).

#### Energy Dispersive Spectroscopy

The EDS spectrum of the magnetic fraction of watershed 18, sample site B, contains large iron peaks, smaller titanium peaks, silica peaks which are internal to the EDS detector, aluminum peaks from the SEM stub, and chlorine peaks from salt contamination (Figure 42). Magnetic minerals containing iron and/or titanium are ulvöspinel (FeFeTiO<sub>4</sub>), magnetite (FeFe<sub>2</sub>O<sub>4</sub>), and ilmenite (FeTiO<sub>3</sub>).

clinochlore-IIb (Mg,Al)<sub>6</sub>(Si,Al)<sub>4</sub>O<sub>10</sub>(OH)<sub>8</sub> (JCPDS, 1986) (Figure 43). Other peaks detected indicate the presence of quartz, mica, and spinels. No weathering or alteration products were detected.

Mica grains provided X-ray patterns representative of muscovite-2M1 (JCPDS, 1986) and biotite (Brown and Brindley, 1980) (Figure 44). Other peaks detected indicate the presence of quartz and spinels. Although no peaks matched any known alteration products of mica, the presence of an 11.68 Å peak suggests that the mica is interlayered with either smectite or vermiculite (Brown and Brindley, 1980). Velbel (1984b) reported widespread alteration of biotite to hydrobiotite, with pronounced (002) peaks at approximately 11.60Å to 12.0Å.

# **Energy Dispersive Spectroscopy**

EDS spectra of chlorite contain large iron, aluminum, and silica peaks and smaller magnesium and potassium peaks (Figure 45). The magnitude of the aluminum peaks represent both the composition of the SEM stub and the composition of the chlorite. The magnitudes of the iron peaks relative to the magnesium peaks indicate a composition in the clinochlore-chamosite solid solution series closer to the chamosite (iron-rich) end-member. The potassium peaks are likely due the presence of other micaceous minerals. The chlorine peak in the spectra is due to salt contamination.

EDS spectra of biotite contain large aluminum and silica peaks with smaller peaks of potassium, iron and magnesium (Figure 46). The chlorine peak is due to salt

Chlorite and Biotite
Light Microscopy

Chlorite and biotite are euhedral to subhedral and are the same size as the surrounding matrix. Chlorite in thin section is often more weathered than epidote, magnetite, pyroxene, garnet, and biotite, and is often less weathered than hornblende. As weathering proceeds, orange-red (on biotite) to red (on chlorite) limonite forms on grain boundaries and along cleavage planes. Exfoliation along cleavage planes and loss of birefringence occurs as weathering continues. Where biotite or chlorite is in contact with garnet or hornblende, limonitic deposits are thicker and weathering appears to be more advanced. In thin sections that contain both weathered chlorite and biotite, chlorite weathering is often more advanced.

# Scanning Electron Microscopy

Chlorite is present in significant amounts in watershed 2, sample sites A and B. Biotite is present in virtually all of the sample locations. Chlorite and biotite grains persist in the saprolite, the upper and the middle horizons. Exfoliation is the only weathering texture discernible via scanning electron microscopy. Micrographs of chlorite and biotite weathering from this study offered no new mica weathering information and are not included here.

# X-ray diffractometry

Randomly mounted chlorite grains provided X-ray diffraction peaks that matched reported data for

contamination. The magnitude of the aluminum peak represents both the composition of the SEM stub and the composition of biotite. The iron peaks are slightly larger than the magnesium peaks suggesting that biotite is more iron-than magnesium-rich.

# Amphibole and Pyroxene Light Microscopy

Amphibole and pyroxene are present in significant amounts in watershed 34 sample site B. Amphiboles occurring in the sample area were identified by their optical properties as hornblende and anthophyllite (Nesse, 1986). Augite was identified as the most prevalent pyroxene (Nesse, 1986). All three minerals are anhedral, contain no inclusions, are matrix-sized, and have weak to moderate preferred orientation. Anthophyllite and augite in thin section are not weathered. Augite in watershed 36, however, has altered to epidote (metamorphic reaction corona). Hornblende is often the most weathered iron-bearing mineral in thin section. Hornblende weathering occurs as orange-red limonitic deposits form on grain boundaries and along cleavage-parallel internal fissures. Surrounding grains of other minerals also become stained with limonitic deposits suggesting that some products of hornblende weathering are being transported away from hornblende grain boundaries.

# Scanning Electron Microscopy

Amphibole grains in the saprolite have cleavageparallel etch pits, ferruginous microboxwork, and denticulated terminations. Amphiboles in the upper and middle horizons are very highly weathered and their abundances decline sharply moving up through the profile. Micrographs of amphibole weathering from this study offered no additional information to that which has been reported by Velbel (1989) for the same sample site and are not included here. Pyroxene grains were not isolated for SEM study.

# X-ray Diffractometry

Grains thought to be amphibole provided peaks representative of both amphibole (end-member anthophyllite) and pyroxene (end-member augite) (JCPDS, 1986) (Figure 47). Other peaks detected indicate the presence of quartz and mica.

## Energy Dispersive Spectroscopy

EDS spectra of pyribole grains contain large silica, aluminum, calcium, and iron peaks and smaller magnesium and potassium peaks (Figure 48). Pyriboles that contain these elements are the pyroxene augite (no potassium) and the amphibole hornblende (all elements) (Nesse, 1986). The chlorine peak is due to salt contamination.

# **Epidote**

# Light Microscopy

Epidote is anhedral to subhedral, matrix-sized, and zoned. Inner portions of individual epidote grains are clinozoisite-rich or, less often, contain quartz inclusions. Many quartz inclusions in both clinozoisite and epidote are

surrounded by radial fractures. In some thin sections, epidote, clinozoisite, quartz and garnet form fine-grained "veins" between larger plagioclase feldspar, potassium feldspar, and quartz grains. In these thin sections, epidote is often stained by orange-red limonite from the weathering of nearby garnet, but epidote itself is not weathered. Epidote was not observed via scanning electron microscopy.

## DISCUSSION

Data obtained from EDS and by X-ray diffractometry indicate that garnet composition in the study area is closest to end-member almandine garnet with some calcium, manganese and magnesium substitution. These findings mirror those of Velbel (1984a, 1985).

Garnet grains weather first at grain boundaries with the formation of limonitic surface layers. Scanning electron microscopy shows that type 1 surface layers meet all the criteria of "protective" surface layers in that they are: 1) continuous over the entire grain surface; 2) appear to be non-porous; and therefore diffusion through them is the weathering rate-limiting step (Berner, 1978, 1981). Type 2 surface layers have micropores leading from the garnet surface to the surrounding environment and are therefore not protective.

There is some question as to whether surface layers are precipitated onto garnet surfaces from external sources or if the surface layers originate as a result of replacement during garnet weathering. Embrechts and Stoops (1982) suggested that the first stage of garnet weathering is characterized by the precipitation of iron oxides, produced by biotite weathering, onto garnet fracture walls. Velbel (1984a), however, noted that there is no void space between garnet and the surrounding matrix in outcrop for biotite weathering products to precipitate into. Therefore, surface layers can form only if the garnet grain boundaries themselves retreat to form the necessary space. This study found textural evidence to support both hypotheses. layers and limonitic deposits on fracture walls are thickest, and weathering is more advanced, where garnet grains are in contact with iron-rich mica (chlorite or biotite). This observation suggests that the weathering, iron-rich mica is contributing to the iron oxide deposits on garnet. If the iron-rich mica provides sufficient amounts of weathering products to the garnet grain surface, then garnet solid solutions, which normally would not produce enough product to form protective surface layers (Velbel, 1993), could do so. The garnet grain boundary still must weather and retreat to provide the needed void space for the surface layer to precipitate into. Where garnet is in contact with quartz or feldspar, iron oxide deposits are of a uniform thickness both in fractures and on the surface of the grain. In the absence of other sources of iron oxides, the garnet grains must weather to supply the needed

materials to form surface layers, and to create the void space necessary for the surface layer to precipitate into. The presence of protective surface layers on garnet grains with no external source for iron oxides (no nearby iron-rich mica) and the absence of rock fracture porosity (means for transporting iron and aluminum oxides in from the surrounding matrix), indicates that precipitation of fracture linings and surface layers from the dissolution of other minerals is not the first step in all garnet weathering processes, as was suggested by Embrechts and Stoops (1982). Their model does seem valid for iron-rich mica gneisses and schists, however (Figures 4, 5, 49).

As weathering proceeds, iron oxides are deposited along internal grain fractures (Figures 2, 4, 5, 6, 49 - 52). Fracture linings observed under the scanning electron microscope are oriented at right angles to the plane of the septa (central partings). Central partings have been observed in high-temperature alteration studies (Wicks and Whittaker, 1977), in ferromagnesium silicate weathering studies (Berner and Schott, 1982; Velbel, 1984a; 1989), and are formed as primary minerals undergo congruent dissolution-reprecipitation weathering reactions (Cressey, 1979; Velbel 1989).

Embrechts and Stoops (1982) reported that garnet undergoes congruent dissolution during the second stage of weathering which is marked by loss of contact between garnet remnants and the surrounding boxwork (fracture linings). Some surface layers on garnet grains observed under the scanning electron microscope are in contact with the garnet

remnant. Most surface layers and garnet remnants observed under the scanning electron microscope, however, are separated by microporous peripheral void space as suggested by Embrechts and Stoops (1982) (Figure 52). The advancing limonite front may continue to be separated from the garnet remnant by micropores, or may eventually be separated by void space large enough to be seen in thin section (Figures 8, 49 - 52). The presence of central partings and the loss of contact between the garnet remnant and the surrounding limonite support the conclusions of Velbel (1984a) and Embrechts and Stoops (1982) that garnet dissolves congruently.

As iron oxides are deposited in the fractures, subsequent layers of iron oxides are also being deposited in contact with previous layers of type 1 surface layers, creating an "onion skin-like" appearance near the garnet surface (Figure 52). This texture suggests that as garnet dissolution proceeds, a zone of supersaturation with respect to iron and aluminum products forms near the garnet surface. When the conditions required for nucleation are met, the products reprecipitate onto the garnet surface, creating the continuous protective "shell" of type 1 surface layers. As the garnet grain boundary dissolves and retreats, contact with the protective layer is lost creating microporosity parallel to the grain surface. The dissolutionreprecipation process then repeats itself, causing surface layers to take on the "onion skin-like" appearance of more weathered grains.

Garnet grains in the study area also form etch pits. Etch pits are the result of interface-limited dissolution (Berner, 1978; 1981). Interface-limited dissolution reactions are characterized by ion (or molecule) detachment at a rate slower than the rate at which reactants are transported to the grain surface. Therefore, the ion detachment rate becomes the rate-limiting step during mineral dissolution and increased flow or advection of reactants to the grain surface does not cause a corresponding increase in interface-limited dissolution rates (Berner 1978; 1981). Garnet grains in environments dominated by biochemical processes or advective flow (located in stream beds) undergo interface-limited dissolution characterized by the absence of protective surface layers and the presence of etch pits (Velbel, 1984a). However, garnet grains in environments not dominated by biochemical processes or advective flow undergo transport-limited dissolution and form protective surface layers (Velbel 1984a). The garnet grains that develop protective surface layers weather more slowly than the grains which do not (Embrechts and Stoops, 1982; Velbel, 1984a). The differences in weathering rates indicates that the rate of diffusion is the weathering rate-limiting step in garnet grains with protective surface layers (Velbel, 1984a). The differences in weathering textures between these environments suggests that garnet weathering mechanisms are more dependent on the rate at which products diffuse away from the grain surface rather than the rate at which reactants diffuse to the grain surface.

importance of product transport during garnet dissolution has been previously noted by Velbel (1993).

Some garnet grains from saprolites and soils have welldeveloped etch pits under type 1 surface layers (Figure 53). There are two plausible explanations for this texture: Some garnet grains are weathering to goethite/gibbsite at a product diffusion rate slower than the rate reactants diffuse through type 1 surface layers, allowing interfacial reactions to occur and etch pits to form on grain surfaces; or 2) Some garnet grains are weathering first to hematite and hematite is subsequently hydrating to goethite (Schwertmann, 1971; Campbell and Schwertmann, 1984). first of these explanations would allow etch pits to form under some type 1 surface layers and would cause etch pits to become filled or covered each time the dissolutionreprecipitation process repeats itself. The second would allow interface-limited reactions to take place until the hematite hydrated to goethite. The increase in product volume caused by the hydration process would fill or cover pre-existing etch pits and (because of the lack of porosity associated with goethitic surface layers) would prevent additional etch pits from forming.

These two explanations of the occurrence of etch pits under type 1 surface layers offer plausible explanations for the unique weathering texture observed in Figure 16. In this micrograph, etch pits are covered by a subsequent layer of secondary products. The garnet grain was removed directly from rock outcrop. The garnet surface layer is discontinuous and may be so because of mechanical separation

from the surrounding matrix or because the surface layer is still forming. The surface layer did form well below the rooting zone and is not discontinuous due to biochemical dissolution. Also, because the garnet was removed from outcrop, the etch pits were not covered by products as a result of direct introduction into the rooting zone followed by reburial. The most probable explanations are that the etch pits formed during preliminary dissolution of the garnet surface and were later filled by the products of the dissolution-reprecipation process, or formed while the garnet surface was covered by a porous, hematitic surface layer and were later filled as the hematite hydrated to a goethite.

Weathering regimes which form both etch pits and protective surface layers are intermediate between transport- and interface-limited kinetic regimes (Berner 1978; 1981). Where type 1 surface layers are discontinuous, interface-limited weathering reactions intensify causing a subsequent increase in etch pits, elongate strings, mammillated surfaces, and, ultimately, boxwork.

Type 2 surface layers increase in thickness higher in the soil profile (Figures 11, 13). This observation indicates that garnets with type 2 surface layers weather by centripetal replacement. Garnet grains with type 2 surface layers appear to have no dissolution features (etch pits, elongate strings, mamillated surfaces, etc.) on their surfaces. Etch pits and other dissolution features, however, may be covered by the oxides which form type 2 surface layers. As previously reported by Velbel (1984a)

and Embrechts and Stoops (1982), garnet weathering (in grains with type 1 or type 2 surface layers) concludes with the formation of a porous pseudomorph of iron and aluminum oxides.

In virtually all sample sites, garnet is weathering to goethite. Garnet is weathering to gibbsite and goethite at sample site 2A. Goethite has been identified as a primary weathering product of garnet (Embrechts and Stoops, 1982; Velbel, 1984a; and Graham, et al. 1989a). Gibbsite has also been identified as a weathering product of garnet by previous workers (Velbel, 1984a; and Graham, et al. 1989a). Velbel (1993) noted that the conservation of iron and aluminum, and the formation of gibbsite and goethite during garnet weathering can result in the formation of protective surface layers. Although gibbsite was detected in only one sample location, petrographic and SEM evidence indicate that protective surface layers exist on garnet grains from all sample locations. Therefore, it is likely that gibbsite is more widespread than the X-ray diffraction patterns of crushed garnet samples indicate. Some reasons why gibbsite was not detected in all locations include abundances below the minimum detection limit of the diffractometer, orientation of sample mount, and the method of sample preparation.

Hematite was the only weathering product detected on garnet grains collected in sample site 2B. Petrographic and SEM evidence indicate that sample site 2B contains some garnet grains that have formed protective surface layers (type 1 surface layers) and some which have not (type 2

surface layers). Velbel (1993) theorized that garnet weathering to hematite would not be able to form protective surface layers because the volume of products could not exceed the volume of reactants. Since site 2B contains garnets with type 1 surface layers and garnets with type 2 surface layers, and since type 1 surface layers are composed of goethite (Velbel, 1984; 1993), both hematite and goethite should have been detected in site 2B. The reasons why goethite was not have been detected by the X-ray diffractometer are similar to those noted previously.

EDS data of the magnetic portion of the samples indicate that it contains both iron and titanium. Magnetic minerals with iron and/or titanium are ulvöspinel (FeFeTiO<sub>4</sub>), magnetite (FeFe<sub>2</sub>O<sub>4</sub>), and ilmenite (FeTiO<sub>3</sub>). Haggerty (1991) described three stages of oxidation in Fe/Ti oxides. Stage C1 is characterized by homogeneous ulvöspinel solid solutions. Stage C2 is characterized by magnetiteenriched solid solutions interlayered with some "exsolved" ilmenite lamellae. Stage C3 is characterized by Ti-poor magnetite and densely crowded "exsolved" ilmenite lamellae. SEM micrographs produced during this study suggest that the magnetic composition of the samples are most like those described in stage C2 of Fe/Ti oxidation in which there are some exsolved ilmenite lamellae. Ilmenite lamellae morphologies observed in this study are most like the trellis and composite types described by Haggerty (1991).

Although magnetite does not appear weathered in thin section, magnetite weathering textures are apparent via scanning electron microscopy. Weathering occurs primarily

by centripetal replacement by iron oxides (Figure 41). Like garnet, some magnetite grains have lace-like and leaf-like secondary products (Figures 39, 40). Many magnetite grains contain ilmenite lamellae which weather more readily than the host (Figures 34 - 38). The pitted and exsolved nature of the more weathered ilmenite lamellae suggest that they are weathering by interface-limited reactions.

Velbel (1993) determined that the weathering of pure magnetite to hematite could produce the necessary volume of product to form protective surface layers. Many magnetite grains in soils and saprolites have thin continuous coatings of weathering products. Although the coatings were not thick enough to be examined closely, they appear to be non-porous. As noted previously, surface layers are considered to be protective if they are continuous and non-porous. Magnetite was not crushed and analyzed with X-ray diffraction and therefore the weathering products of magnetite were not identified.

The chlorite composition determined by X-ray diffractometry (magnesium end-member clinochlore-IIb) differs from that determined by EDS (iron end-member chamosite). The EDS composition was determined from single grains, while the X-ray diffraction pattern represents several grains from different locations. The X-ray diffraction pattern most likely represents a range of solid solutions occurring within the study area. However, since the results are inconsistent, no conclusions can made regarding the composition of chlorite occurring in the Coweeta Basin.

Mica grains from several sample locations provided X-ray diffraction patterns closest to muscovite and biotite.

The EDS analysis is consistent with the biotite composition proposed by Velbel (1985) for this study area.

Although chlorite and biotite appear to be weathering to iron oxides in thin section, interstratifed vermiculite or smectite were the only weathering products detected on grains analyzed with X-ray diffraction. Previous workers have reported that in the first stage of weathering, mica alters to vermiculite by removal of interlayer cations and addition of water to the overall structure (Gilkes and Little, 1972; Bain, 1972; Bain, 1977; Churchman, 1979; Anand and Gilkes, 1984a; Banfield and Eggleton, 1988). During the second stage of weathering, mica/vermiculite alters to goethite by the oxidation of ferrous iron (Gilkes and Little, 1972; Bain, 1972; Bain, 1977; Churchman, 1979; Anand and Gilkes, 1984a; Banfield and Eggleton, 1988). Mica grains in thin section appear to be in the second stage of weathering. Mica grains in the soil appear to be in the first stage of weathering. Some reasons why the weathering process seems reversed are that: 1) mica aggregates survive throughout the soil profile and those in the interior of these aggregates are protected from weathering agents by the outermost grains; and 2) second stage, goethite (limonite), alteration that is optically distinct in microscopy, may not be detectable by X-ray diffractometry.

Hornblende is also weathering to iron oxides in thin section. However, iron oxides were not detected by X-ray diffractometry. As noted previously, the amount of iron

oxides present may have been below the minimum detection limit of X-ray diffraction.

### SUMMARY

Garnet in outcrop develops surface layers as garnet grain boundaries retreat during congruent dissolution. Surface layers may form from the weathering of other primary minerals, or by the weathering of garnet. Garnet grains can develop either protective or non-protective surface layers dependent on the garnet composition, type of secondary products formed, and environmental conditions. Garnet and limonite in thin section form three distinct textures: grains in which limonite is in contact with the garnet remnant; 2) grains in which limonite is not in contact with the garnet remnant (formation of a peripheral void around remnant), and; 3) grains in which limonite has formed a porous pseudomorph after garnet. Garnet grains in environments dominated by biochemical processes and advective flow undergo interface-limited reactions. Garnet grains in environments not dominated by these processes experience supersaturation with respect to iron and aluminum products near the grain surface. When the requirements for nucleation are met, the products reprecipitate to form protective surface layers. Some garnet grains have etch pits under protective surface layers. The etch pits under protective surface layers may become filled or covered.

Filled etch pits under protective surface layers may be the result of hematitic surface layers hydrating to goethitic surface layers or the result of dissolution-reprecipiation processes. Although the garnet surface under protective surface layers may be undergoing interfacial reactions, the dissolution rate of the garnet is limited by the rate at which products diffuse through the protective surface layer. Garnet dissolution processes which form protective surface layers and etch pits are intermediate between transport- and interface-limited kinetic regimes (Berner, 1978; 1981). Discontinuous surface layers permit the formation of advanced dissolution textures such as increased etching, elongate strings, mammillated surfaces, and boxwork.

Garnet compositions are closest to end-member almandine with some calcium, manganese and magnesium substitution.

Garnet is weathering predominantly to goethite, as well as to hematite and gibbsite.

Magnetite weathering is independent of depth or location due to the presence of mica coatings. Magnetite weathering occurs primarily by centripetal replacement by iron oxides, but significant weathering also occurs by preferential dissolution of ilmenite lamellae. Chlorite, biotite, and hornblende are weathering to form orange-red limonitic products in thin section. Limonitic products from the weathering of all three minerals are being transported away from their grain boundaries and deposited on other primary minerals.

Chlorite and biotite are weathering to interstratified vermiculite and iron oxides, and persist throughout the soil

profile. Hornblende is weathering to iron oxides and declines in abundance moving upwards in the soil profile. Under the scanning electron microscope, weathered chlorite and biotite are exfoliated and amphibole has cleavage-parallel etch pits, ferruginous microboxwork, and denticulated terminations. Pyroxene and epidote are not weathered in thin section and were not observed by scanning electron microscopy.

## CHAPTER 2

## DISTRIBUTION AND OCCURRENCE OF HEMATITE AND GOETHITE

### REVIEW

Hematite  $(\alpha\text{-Fe}_2O_3)$  and goethite  $(\alpha\text{-Fe}OOH)$  are the most abundant secondary iron oxide minerals forming at the Earth's surface (Schwertmann, 1988). Although thermodynamic data indicate that only one or the other can be stable for a given set of environmental conditions (Mohr et al., 1972), they often coexist (Schwertmann, 1985). Thermodynamic studies also do not explain their relative proportions within study areas (Schwertmann, 1985). Several workers have tried to explain goethite and hematite proportions by empirical observation and laboratory studies. Langmuir (1971) suggested that goethite crystals smaller than 76 nm are unstable relative to hematite. This observation does not, however, describe soil conditions in which most goethite crystals are smaller than 76 nm and yet still coexist with hematite (Taylor, 1987). Nahon et al. (1977) and Yapp (1983) noted that aluminum substituted goethite is more stable than unsubstituted goethite relative to hematite, but not all soil goethites have aluminum substitution (Schwertmann, 1985). Schwertmann (1988) theorized that goethite and hematite proportions could best be explained by their processes of formation. Goethite forms by dissolution of iron-bearing primary and secondary

minerals (hematite), followed by reprecipitation from solution (neoformation) (Fischer, 1971, in Fischer and Schwertmann, 1975; Schwertmann, 1971; Campbell and Schwertmann, 1984). Hematite was once believed to form from goethite by dehydration (Fischer and Schwertmann, 1975), however, long-term laboratory studies of hematite and goethite formed at room temperature from amorphous iron hydroxides indicates that their relative proportions do not change with time (Schwertmann, unpublished results, in Fischer and Schwertmann, 1975; Schwertmann, 1985). Hematite is now believed to form by dehydration (transformation) of ferrihydrite (Fe<sub>2</sub>O<sub>3</sub>·2FeOOH·2.6H<sub>2</sub>O) (Schwertmann and Murad, 1983; Schwertmann, 1988; Schwertmann and Taylor, 1989). Schwertmann and Murad (1983) found that storage of ferrihydrite in aqueous suspensions (24.0 °C and pH 2.5-12.0) for up to three years resulted in the formation of hematite and goethite. Both ferrihydrite and goethite precipitating from solution (depending on whether the higher solubility of ferrihydrite is exceeded) might explain why both hematite and goethite can co-occur (Schwertmann, 1988; Schwertmann and Taylor, 1989).

Several workers have identified climatic, pedologic, and geologic factors that may control the relative abundance of goethite and hematite. Higher temperatures and drier conditions promote the dehydration of ferrihydrite, and therefore, the formation of hematite (Kämpf and Schwertmann, 1982b). High soil organic matter promotes the occurrence of goethite (Schwertmann, 1971; Kämpf and Schwertmann, 1982b). At pH 12 and 4, Fe(OH)<sub>4</sub> and Fe(OH)<sub>2</sub> ions (respectively)

are favored. The presence of these ions in solution favors the formation of goethite (Schwertmann and Murad, 1983). Hematite is favored when Fe(OH)<sub>4</sub> and Fe(OH)<sub>2</sub> ions are absent and pH levels are at the zero point for ferrihydrite: pH 7-8 (Schwertmann and Murad, 1983). Ferrihydrite (hematite) is also favored by higher rates of iron(III) release from parent minerals (Schwertmann, 1988). Laboratory studies show that small amounts of aluminum supress the formation of goethite (Schwertmann, 1985), however, this relationship has not been demonstrated in field studies (Schwertmann, 1985).

Soil color is largely a reflection of iron oxide mineralogy (Torrent et al., 1980; Torrent and Schwertmann, 1987). Soils containing only goethite have Munsell colors of 7.5YR to 2.5Y (yellow to brown). Hematite yields soil colors of 5YR and redder. The redness rating of soils (Torrent et al., 1983), determined from the dry Munsell colors of soils, shows a direct, linear relationship to hematite content (Torrent et al., 1983; Graham et al., 1989b). In soils with both goethite and hematite, even small amounts of hematite will mask the yellowness of goethite (Schwertmann and Taylor, 1989). Oxalate treatment of soils containing goethite and ferrihydrite causes soil colors to become more yellow, suggesting that amorphous iron oxides (ferrihydrite) also contribute to the redness of soils (Schwertmann and Lentze, 1966, in Schwertmann et al., 1982; Schwertmann et al., 1982b).

Environmental factors which influence the relative proportions of hematite and goethite are precipitation,

temperature, slope (moisture), aspect (temperature, moisture, organic matter), parent rock mineralogy (pH, rate of iron(III) release), pH and vegetation cover (pH, organic matter, rate of iron(III) release) (Schwertmann, 1988). Based on these observations, it is expected that sample sites in the western portion of the Coweeta Basin will be more goethitic than those in the eastern portion, due to the cooler temperatures and increased precipitation. Northfacing slopes are expected to be more goethitic than the south-facing slopes due to cooler temperatures and increased organic matter content. Finally, it is expected that the disturbed watersheds will be more hematitic than the control watersheds because: 1) white pine stands transpire more moisture than mixed hardwood stands and may create drier soil conditions; and 2) logging and clearing the disturbed watersheds may have caused underlying soils to increase in temperature temporarily during more direct exposure to the sunlight.

## **METHODS**

# Soils

Soils from the four undisturbed and the two disturbed watersheds were selected for study. Soil pH was determined in a 1:1 oven-dried (60 °C, non-circulating) soil:water slurry using an Orion 701A/Digital Ionalyzer pH meter.

Total soil carbon was determined on oven-dried soil using a

Rosemount Analytical/Dohrmann DC-190 Carbon Analyzer in the total carbon/boat sample mode. Total carbon values reported in the total carbon/boat mode reflect the sum of both organic and inorganic carbon present in the samples. However, since the parent and secondary mineralogy of the sites do not indicate the presence of inorganic carbon-rich minerals, the values reported here are considered to be an accurate reflection of the organic carbon present in the samples. Soil color was determined on wet bulk soils in bright afternoon sun utilizing a Munsell Soil Color Chart. Dry colors were determined for treated clays. Particle size analyses were determined by the hydrometer method (Bouyoucos, 1962). Due to the micaceous nature of the study soils, silt and sand size fraction data should be regarded as minimum values. Aspect, percent slope, and depth to bedrock in each sample site was determined by an azimuth Brunton compass, an Abney level, and by hand-augering to paralithic contacts, respectively. Elevation and average annual precipitation for each site were taken from Hatcher (1980) and Swift et al. (1988).

# X-Ray Diffraction

Soil samples were wet sieved to <53  $\mu m$  and heated in an 80 °C water bath with an approximately 50:50 ratio of  $H_2O:H_2O_2$  to remove organic matter (Soil Conservation Service, 1967). The soil samples were then suspended in 1000 ml of distilled water and dispersed with 2 to 10 ml of sodium hexametaphosphate to separate (by siphon) the clay (<2  $\mu m$ ) fraction. The clay fraction was centrifuge-washed

in 60 - 90% acetone and oven dried at 60 °C. A portion of each washed clay fraction was then boiled in 5 M NaOH and 0.2 M Si solution to concentrate the iron oxides present and to enhance the possibility of determining the aluminum substitution of goethite (Kämpf and Schwertmann, 1982a). The concentrated samples were centrifuge-washed once in 5 M NaOH and 0.2 M Si solution, once in 0.5 M HCl solution, twice in 1 N (NH<sub>4</sub>)<sub>2</sub>CO<sub>3</sub> solution and dried at 60 °C. After X-ray diffraction data were obtained on the NaOH-treated samples, the iron oxides of four NaOH samples were selectively dissolved by dithionite-citrate-bicarbonate (DCB) extraction (Mehra and Jackson, 1960). The untreated, and the NaOH- and DCB-treated clay samples were analyzed by X-ray diffraction in random powder mounts. X-ray diffraction data for all of the clay samples were obtained using CoKa radiation (35 kv, 25 mA) and a Phillips goniometer equipped with a 1° divergence slit, a 0.2 mm receiving slit, and a 1° scatter slit. The NaOH- and the DCB-treated samples were step-scanned from 22 to 30 °20 at 0.05 '20 steps using a counting time of 10 sec/step. The untreated samples were step-scanned from 8 to 53 '29 at 0.05 20 steps using a counting time of 2 sec/step.

## RESULTS

The results of the soil analyses are listed in Tables 3
- 7. The X-ray analyses of the untreated clay samples

obtained from the middle horizons indicate the presence of kaolinite (most abundant), muscovite, biotite, goethite, quartz, and magnetite/maghemite at all sample locations (Figure 54). X-ray analyses of saprolite from selected locations indicates the presence of the minerals listed for the middle horizons as well as vermiculite and gibbsite (Figure 55). Hematite was not detected in any untreated samples (Figures 54, 55).

The NaOH-treated goethite 24.8 °20 peak was detected in saprolite and middle horizons of all sample locations (Figures 56, 57, and 58). The magnitude of the goethite 24.8 °20 peak varies with sample location. The presence of goethite was confirmed by selective dissolution of iron oxides in four NaOH-treated samples. Patterns obtained from samples in which iron oxides were selectively dissolved do not contain the goethite 24.8 °20 peak (Figures 56, 57, 58, 59, 60, and 61). Although the goethite peaks are well-developed, peak widths are too broad to measure the shift due to aluminum substitution.

Hematite was not detected in any of the NaOH-treated samples due to the precipitation of synthetic sodalite  $(Na_4Al_3Si_3O_{12}Cl)$  during sample preparation. The sodalite formed as kaolinite  $[Al_2Si_2O_5(OH)_4]$  dissolved in the boiling NaOH and then reacted with NaCl. (NaCl had been used in an earlier step to flocculate the clay and was not completely washed from solution prior to boiling in NaOH.) Sodalite peaks correspond to all hematite peaks not masked by goethite. Therefore, the relative proportions of hematite

and goethite in each sample area can not be determined from the diffraction patterns.

The dry colors (Table 6) and the redness ratings (Table 7) (Torrent et al., 1983) of the NaOH-treated clays indicate that sample site 2B is at least partially hematitic (Torrent et al., 1980; Torrent and Schwertmann, 1987). All other sample locations are more goethitic (Torrent et al., 1980; Torrent and Schwertmann, 1987).

#### DISCUSSION

The clay mineralogy of the untreated samples (middle horizons and saprolite) does not vary significantly from sample site to sample site. Apparently the differences in soil, geologic and geomorphic variables in this study area are too small to produce major differences in the types of crystalline weathering products, although differences in the relative abundances of secondary minerals were found. The X-ray diffraction peaks for goethite differ in magnitude in the NaOH-treated clays of the middle horizons of sites 17A and 36A) (Figures 56, 58). It is likely that variations in the soil, geologic and geomorphic conditions within the Coweeta Basin affect the relative abundances of clay minerals, rather than the clay mineral assemblage at each sample location.

The <2  $\mu m$  size fraction of the middle horizons contain kaolinite, muscovite, biotite, quartz, and

magnetite/maghemite. The saprolite contains the minerals listed for the middle horizons plus vermiculite and gibbsite. Vermiculite in the clay fraction is derived from the weathering of the micaceous primary minerals (Bain, 1972; Bain, 1977; Churchman, 1979; Gilkes and Suddhiprakarn, 1979; Anand and Gilkes, 1984a; Velbel, 1985; Banfield and Eggleton, 1988). Kaolinite can be derived from the weathering of micaceous primary minerals, vermiculite and feldspar. Also, the presence of gibbsite in the saprolite and not in the middle horizons of the profiles suggests that qibbsite may have undergone resilication to form kaolinite in the middle horizons. Calvert et al. (1980) and Buol and Weed (1991) reported the resilication of gibbsite within profiles of the North Carolina Piedmont. The gibbsite in the saprolite is derived from the weathering of feldspars and garnet (Embrechts and Stoops, 1982; Velbel, 1984a; Velbel, 1985; Graham et al., 1989a, b; Buol and Weed, 1991). Muscovite, biotite, quartz, and magnetite/maghemite are primary minerals disaggregated from the parent rock. Goethite is derived from most of the iron-bearing primary minerals occurring in the study area (Gilkes and Little, 1972; Bain, 1977; Gilkes and Suddhiprakarn, 1979; Embrechts and Stoops, 1982; Berner and Schott, 1982; Velbel, 1984a; Anand and Gilkes, 1984a; Banfield and Eggleton, 1988; Graham et al., 1989a, b). Goethite may also be forming from hematite found on garnet grains in sample site 2B (Schwertmann, 1971; Campbell and Schwertmann, 1984). Hematite can form from garnet weathering, magnetite weathering, and from the dehydration of ferrihydrite (Gilkes

and Suddhiprakarn, 1979; Morris, 1980; Embrechts and Stoops, 1982; Anand and Gilkes, 1984b; Velbel, 1984; Schwertmann, 1988; Graham et al., 1989a, b; Schwertmann and Taylor, 1989). Ferrihydrite was not detected by X-ray diffraction in any clay or mineral samples. However, peak overlap with other iron oxides, and the poorly crystalline nature of ferrihydrite can prevent its detection.

The clay mineralogy for this study area differs from the clay mineralogy of the nearby North Carolina Blue Ridge Front. Graham et al. (1989b) reported the presence of gibbsite, muscovite, chlorite, biotite, vermiculite, interstratified biotite/vermiculite, hematite, goethite, and kaolinite in profiles sampled on the Blue Ridge Front. Gibbsite was the most abundant clay mineral forming on Blue Ridge Front residuum, in contrast with the Coweeta soils, in which kaolinite is the most abundant secondary mineral. Gibbsite in the Blue Ridge Front is more abundant in residual soils and saprolite and declines in abundance moving upwards in the soil profile (Graham et al., 1989b). Gibbsite is present in the saprolite at Coweeta and also declines in abundance upward in the soil profile. Barshad (1966) reported that, in soils derived from acid igneous rocks, an increase in precipitation caused increases in gibbsite abundances and decreases in kaolinite abundances. However, it is the wetter Coweeta sites that have more kaolinite relative to gibbsite, while the drier Blue Ridge Front sites have more gibbsite relative to kaolinite. Perhaps the predicted relationship between gibbsite and precipitation (Barshad, 1966) was not observed in these

sites because the rocks in both the Blue Ridge Front and the Coweeta sites are not acid igneous rocks, but mica schists and gneisses (Graham et al., 1990; Hatcher, 1980). also likely that other variables such as slope, vegetation, aspect, and soil temperature complicate the simple relationship between precipitation and gibbsite abundance proposed by Barshad (1966). In the North Carolina Piedmont, Buol and Weed (1991) and Calvert et al. (1980) theorized that gibbsite can form as a direct weathering product of aluminous minerals if pH and water movement conditions allow for the precipitation of aluminum and the leaching of silica. Gibbsite will alter to kaolinite if those conditions allow silica to become available for resilication. The pH range at the Blue Ridge Front site, however, does not differ from the range at Coweeta. movement" at Coweeta is occurring in well- to extremely well-drained soil profiles. Well-drained conditions would seem to favor the leaching of silica and disfavor the formation of kaolinite.

The change in gibbsite abundances from the saprolite to soil regions of both locations may be due to changes in pH (4-5 in the middle horizons and 5-6 in the saprolite) (Buol and Weed, 1991). Also, the increase in clay content, and therefore the decrease in permeability in the middle horizons, may cause gibbsite to be more stable in the saprolite and kaolinite to be more stable in the middle horizons (Buol and Weed, 1991).

## SUMMARY

The variability among the soil, geologic and geomorphic conditions within the Coweeta Basin does not drastically alter the clay mineral assemblage occurring at each sample The differences between sample sites in clay mineral abundances are, however, likely due to these environmental variances. The clay mineralogy of the Coweeta Basin differs from the clay mineralogy of the Blue Ridge Front in that kaolinite, rather than gibbsite, is the most abundant clay mineral, for reasons other than precipitation amount and soil pH. Drainage conditions and pH levels seem to render gibbsite more stable in the saprolites than in overlying soil horizons of Coweeta, the North Carolina Blue Ridge Front and the North Carolina Piedmont. Kaolinite is more abundant in the middle horizons than the saprolite at all of these study areas. All minerals detected in the clay fraction are either clay-sized primary minerals or weathering products of the primary minerals occurring in the study area. Redness ratings and dry clay Munsell Colors of NaOH-treated soils indicate that most Coweeta soils are goethitic rather than hematitic.

### CHAPTER 3

### GENERAL DISCUSSION

The environmental factors that influence the distribution and occurrence of hematite and goethite are reported to be slope, aspect, parent rock mineralogy, precipitation, pH, temperature, organic matter content and vegetation cover (Schwertmann, 1988). Scatter plots of elevation, pH, total carbon, slope, clay, aspect, and precipitation versus redness ratings for the middle horizons of each sample site are included as Figures 62 to 68. The plots indicate that, in the middle horizons, there is a direct correlation between redness ratings and clay  $(R^2 =$ 0.46), an inverse correlation between redness ratings and precipitation ( $R^2 = 0.73$ ), and no correlation ( $R^2 = 0.00$ ) between redness ratings and aspect, slope, and total carbon content (Figures 62 - 68). The correlations between redness ratings and pH ( $R^2 = 0.16$ ) and elevation ( $R^2 = 0.14$ ) are not statistically significant (P> 0.15). Redness ratings of the sampled saprolites do not vary significantly, and therefore no correlations with environmental factors and redness ratings were found. Also, the redness ratings of control and disturbed watersheds do not differ significantly, and therefore no correlations between redness ratings and watershed type could be found.

The lack of correlation between aspect and redness ratings (Figure 62) suggests that variations in aspect do not affect soil temperature, moisture and organic matter

content enough to affect hematite abundance. Insufficient time to develop measurable differences in the study variables (soil immaturity) is the most probable reason for the lack of correlations between redness ratings and the environmental conditions of the saprolites.

The correlation between percent clay and redness ratings (Figure 63) reflects the soil process of clay translocation. Iron oxides are most abundant in the clay fraction (Schwertmann, 1988) and accumulate, with other clay minerals, in B horizons. A larger amount of clay-sized particles, therefore, may reflect a larger iron oxide concentration. As iron oxides concentrate in the middle horizons, the redness of hematite will mask the yellowness of goethite, causing an increase in redness ratings (Torrent et al., 1983; Graham et al., 1989b; Schwertmann and Taylor, 1989).

The lack of a significant relationship between pH and redness ratings (Figure 64) differs from laboratory findings. Schwertmann and Murad (1983) found that hematite abundances increase with increasing pH in the range from pH 4 to pH 7-8. Goethite declines in abundances in this pH range. Redness ratings reflect the amount of hematite present (Torrent et al., 1983; Graham et al., 1989b). If the laboratory predictions regarding pH and hematite abundances are accurate, the redness ratings of this study should have a direct correlation with pH. The relationship between pH and redness ratings may reversed because: 1) the pH range in the Coweeta Basin may not vary enough to demonstrate a true trend between pH and redness ratings; and

2) an as yet unidentified, stronger soil variable may be masking the true trend between pH and redness ratings.

The inverse correlation between redness ratings and precipitation (Figure 65) is as expected. Kämpf and Schwertmann (1982b) found that increasing precipitation minus evapotranspiration caused an increase goethite abundance and a corresponding decrease in hematite abundance. The plot of precipitation versus redness ratings at Coweeta does not account for losses in soil moisture due to evapotranspiration, however, the evapotranspiration rate on control watersheds is considered to be relatively constant due to similar vegetation and environmental conditions. Therefore the trend between redness ratings and precipitation is an adequate reflection of the trend between redness ratings and precipitation minus evapotranspiration.

Although the correlation between redness ratings and elevation (Figure 66) is not statistically significant, the plot shows a weak inverse trend. The higher elevations in the Coweeta Basin receive greater amounts of precipitation and have cooler temperatures (Swift et al., 1988). Changes in elevation at Coweeta, then, reflect changes in precipitation and temperature. Previous studies have found that hematite abundances decline as temperature decreases and as average annual precipitation increases (Kämpf and Schwertmann, 1988). Therefore, a stronger inverse correlation was expected. The weakness of the trend may be due to: 1) the range of elevation data points not varying enough to demonstrate the true trend between elevation and redness ratings; and 2) other, more dominant variables

masking the true trend between redness ratings and elevation.

The lack of correlation between percent organic matter and redness ratings is not as expected (Figure 67). Kämpf and Schwertmann (1982b) reported that, in Brazilian soils, increasing organic matter content caused an increase in the [goethite / (goethite + hematite)] ratio. An increase in this ratio would correspond to a decrease in the redness rating of soils. The lack of correlation in this study may be caused by: 1) organic matter contents too low to affect hematite and goethite proportions; and/or 2) other, more dominant soil variables masking the true trend between redness ratings and percent total carbon.

There is no correlation between slope and redness ratings (Figure 68). This observation differs from findings in the Blue Ridge Front Study. The percent goethite and the percent goethite + hematite in residual soils of the Blue Ridge Front studies (Graham et al., 1989a, b; 1990a, b) is greater than in colluvial soils (Table 8). Residual and colluvial soils derived from almandine-poor parent material have lower percentages of goethite and goethite + hematite than soils derived from almandine-rich parent material. These trends are also duplicated for hematite abundances in the translocated (Bt) horizons. Greater amounts of goethite and hematite in the residual versus colluvial soils suggests that iron oxide formation in the Blue Ridge Front is favored in the more stable and more mature residual soils. The soils formed on the steeper, less stable slopes of Coweeta, then, would be expected to have lower redness ratings

yielding an inverse correlation between redness ratings and percent slope (if all other variables remain equal).

There is no clear relationship between parent rock mineralogy and redness ratings. The soils with the highest redness ratings are from the middle horizons of sample sites 2B (Tallulah Falls Formation, tf), 2A (tf), 17A (tf), 18A (tf) and 34A (Carroll Knob Ultramafic Complex, ck). The least red soil sample is from the middle horizons of site 36A (tf). Soils underlain by the Tallulah Falls Formation (tf) represent extremes of redness ratings. There are several possible reasons for this observation: 1) watershed 36 receives more 45 cm more precipitation per year than watershed 2 (Table 1), and is expected to be less red despite parent rock similarities (Kämpf and Schwertmann, 1989b); 2) sample site 36A is higher in elevation than sample site 2B and may have cooler temperatures; and, 3) redness ratings may be due to local variability in ironbearing mineral abundance within the Tallulah Falls Formation. The first and second of these possibilities are supported by this study (Table 1, and Figures 62 - 68) and previous studies (Kämpf and Schwertmann, 1982b). The third possibility is supported by thin section and X-ray diffraction data from this study. The thin section of parent rock at sample site 36A contains 31% iron-bearing minerals, 19% of which is unweathered epidote (Table 2). Watershed 2 ranges from 1 - 14% iron-bearing minerals and contains an abundance of weathering iron-rich chlorite (see chapter 1) not included in the point counts from watershed 2 (Table 2). Schwertmann (1988) found that the rate of iron

release from parent minerals can affect the relative proportions of hematite and goethite. Since watershed 2 has more iron-bearing minerals weathering to products than watershed 36 has, the flux of iron(III) may be causing an increase of hematite proportions and a corresponding increase in redness ratings.

Redness ratings indicate that the soils at Coweeta Basin are less hematitic than the soils of the Blue Ridge Front (Table 7 and Graham et al., 1989b). Graham et al. (1989a) concluded that in the Blue Ridge Front, hematite abundances and redness ratings are controlled by geologic variables (the presence or absence of almandine garnet in the parent material). In the Coweeta Basin, the Carroll Knob Ultramafic Complex has the most iron-bearing minerals to weather (Table 2) and the least stable (most weathered) iron-bearing minerals observed in this study (see chapter The Coweeta Coleman River Formation has the least iron-1). bearing minerals to weather (Velbel, 1985; Table 2). If parent rock mineralogy is the most significant factor controlling hematite occurrence within a study area, then soils derived from Carroll Knob Ultramafic Complex should be the most red and soils derived from the Coweeta Coleman River Formation should be the least red. This is not always the case (Tables 2 and 7). Weathering of the Tallulah Falls Formation has produced some soils that are redder than soils derived from the Carroll Knob Ultramafic Complex. Also, soils derived from the Tallulah Falls Formation are occasionally less red than those derived from the Coweeta Coleman River Formation (Table 7). Therefore, climatic and

pedologic factors between sample sites must be at least as significant as geologic factors.

The redness ratings of the Blue Ridge Front almandinerich schists are redder than the almandine-poor gneisses,
but there may be other parent rock attributes (other than
the presence of almandine garnet) influencing hematite
occurrences in the Blue Ridge Front. Gneiss, for example,
is harder and more resistant to weathering than schist
(Velbel, 1985). Therefore, the weathering of schist is more
likely to produce more products in less time than gneiss.
Also, the schists in the Blue Ridge Front study area have
much higher percentages of iron-bearing minerals to weather
to products than the gneisses (34% versus 9%, respectively,
Graham et al., 1989b; Table 2). Faster rates of rock
weathering and larger abundances of iron-bearing primary
minerals cause larger fluxes of iron(III) and therefore
favor the formation of hematite (Schwertmann, 1988).

The present study of almandine garnet weathering in the Coweeta Basin did not detect as much hematite products as did the Blue Ridge Front study. There are two possible reasons for this difference: 1) The Mössbauer spectroscopy used in the Blue Ridge Front study is a more sensitive means of measuring iron oxide abundances than is X-ray diffraction; and, 2) Mössbauer spectroscopy indicated that 70% of individual garnet grains had gone to products in the Blue Ridge Front (Graham et al., 1989b), and only watershed 2 of the Coweeta Basin (thin section C80-2-1C) contained garnet grains weathered to the same degree. Watershed 2 is

also the only Coweeta Basin sample site in which X-ray diffraction studies detected the presence of hematite.

The differences in parent rock types may also be contributing to the differences in redness ratings between the two study areas. The rocks underlying the Blue Ridge Front are fine-grained mica schists and gneisses. The rocks underlying the Coweeta Basin are coarse-grained schists, gneisses and ultramafic bodies. Smaller mineral crystal sizes yield larger surface area to volume ratios. Crystals with larger surface area to volume ratios have more surfaces to undergo weathering and therefore weather more quickly (Velbel, 1985). As noted previously, garnet grains observed in the Blue Ridge Front study do appear to be more weathered than those of the Coweeta Basin. Faster rates of weathering and production of iron(III) favor more hematitic soils such as those of the Blue Ridge Front study area (Schwertmann, 1988).

Finally, the Blue Ridge Front study site may be more hematitic than Coweeta because of differences in environmental conditions (Table 9). Coweeta receives more precipitation, has higher elevations, and has cooler temperatures than the Blue Ridge Front site. Increased precipitation and cooler temperatures favor goethitic rather than hematitic soils (Kämpf and Schwertmann, 1982b).

There are significant differences in the redness ratings of the soil samples obtained from watershed 2 of the Coweeta Basin. The two sample sites have similar parent rock mineralogy, mean annual precipitation, aspect and percent slope. The sites differ in elevation, pH, and soil

The relationship between pH and redness ratings have type. been discussed previously. Sample site A is higher in elevation, is classified as Marine, Humid Temperate and is underlain by the Chandler Series (Typic Dystrochrepts) Sample site B is classified as borderline Humid soils. Subtropical/Marine, Humid Temperate and is underlain by the Fannin Series (Typic Hapludults) soils. The differences in soil types reflect different levels of soil development. Because Chandler Series Inceptisols form on steeper, less stable slopes, they are often less mature than Fannin Series Ultisols (Swank and Crossley, 1988). As noted previously, mature soils favor the formation of iron oxides over less developed soils. Higher concentrations of iron oxides may cause larger concentrations of hematite and higher redness ratings. Kämpf and Schwertmann (1982b) found that in Ultisols and Inceptisols of south Brazil, increasing mean annual air temperature causes an increase in hematite to hematite + goethite proportions. An increase in this proportion corresponds to an increase in redness ratings. Differences in temperature and soil development, then, best explain the differences in redness ratings in watershed 2.

Watershed 34 also has differences in redness ratings. The sample sites have similar elevations, soil types, average annual precipitation, aspect, and slope. The sites differ in parent rock mineralogy, pH and percent total carbon (Tables 2, 3, and 4). Site B is underlain by the Tallulah Falls Formation and is higher in total carbon. The redder soils of site A are underlain by the Carroll Knob Ultramafic Complex. High soil organic matter content (total

carbon) favors goethite formation and yellower soils (Schwertmann, 1971; Kämpf and Schwertmann, 1982b). The Carroll Knob Ultramafic Complex has a larger percentage of iron-bearing minerals weathering to products than the Tallulah Falls Formation (Table 2). The differences in the redness ratings, then, are probably due to increased iron (Schwertmann, 1988) weathering to products in the Carroll Knob Ultramafic Complex (Table 1) and/or to differences in total carbon (Schwertmann, 1971; Kämpf and Schwertmann, 1982b).

## CHAPTER 4

## CONCLUSIONS

of the iron-bearing minerals present in the study area, only garnet and magnetite appear to be weathering to hematite. Garnet more commonly weathers to goethite. Chlorite, biotite and hornblende are also weathering to iron-rich products, but the exact composition of these products could not be determined in this study. The results of previous research (Bain, 1972; Bain, 1977; Velbel, 1984a; Velbel, 1985; Banfield and Eggleton, 1988) indicate that the iron-rich product of chlorite, biotite, and hornblende weathering is probably goethite. The redness ratings, determined from the dry Munsell Colors of NaOH-treated clays, indicate that the soils of sample site 2B are at least partially hematitic. The soils of all other sample sites are more goethitic.

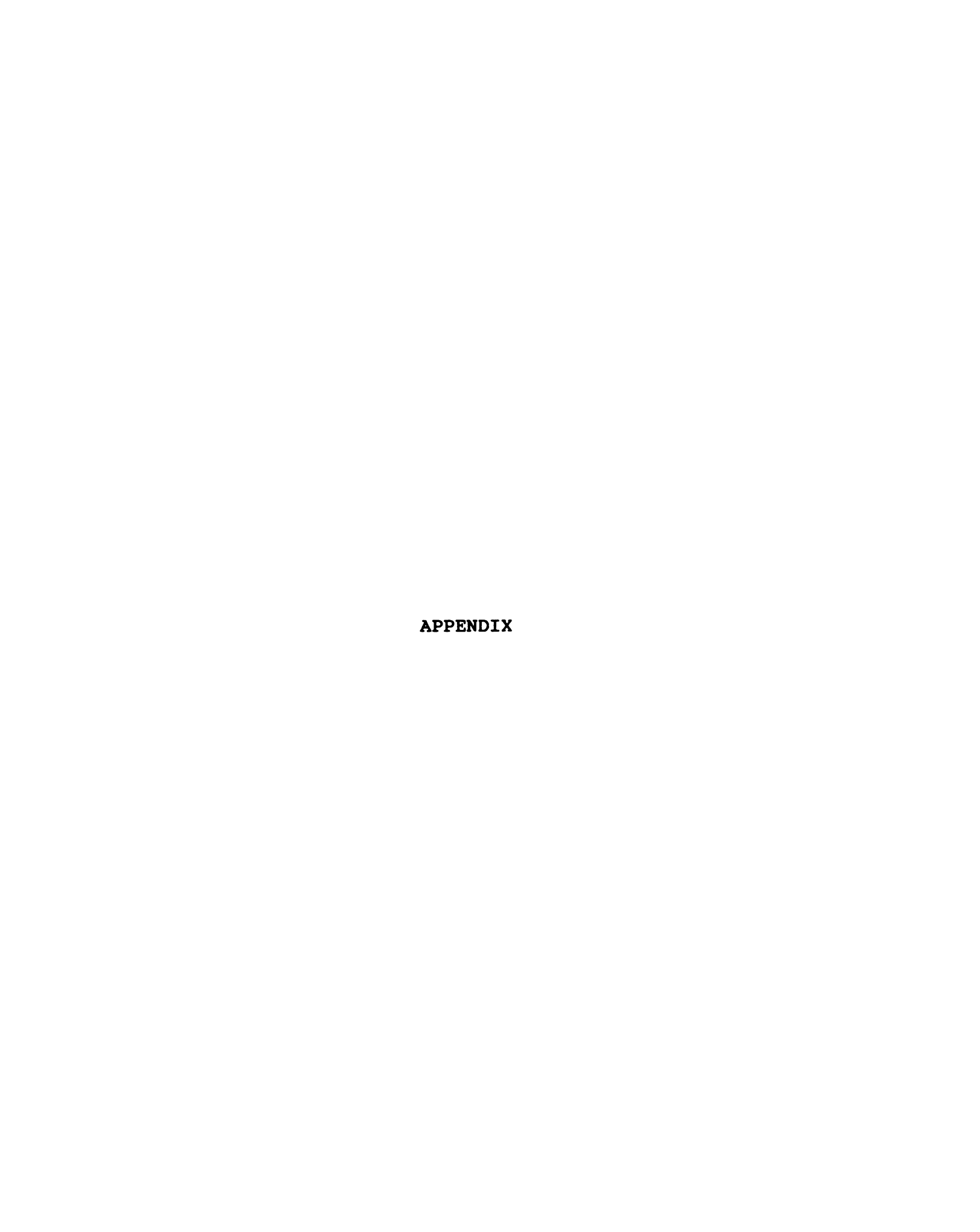
No correlation between redness ratings and the climatic, geologic, and pedologic conditions of saprolites was determined. There was also no correlation determined between redness ratings and aspect, percent total carbon, and percent slope. The correlation between pH and redness ratings differs from laboratory findings due, perhaps, the limited range of pH data points, or to masking by another environmental factor. The correlation between elevation and redness ratings in not statistically significant although a weak inverse relationship was detected. The correlation between redness ratings, percent clay, and average annual

precipitation are consistent with the results of previous studies. Although no correlation between redness ratings and percent slope was found at Coweeta, residual soils in the Blue Ridge Front site are more red than colluvial soils due to differences in soil maturity and landscape stability. There is no clear distinction between the redness ratings of controlled and manipulated study sites.

Soils underlain by the same geologic formation have a range of redness ratings suggesting that climatic and pedologic variables influence hematite occurrences at least as much as geologic variables. Within watersheds underlain by a single formation, differences in redness ratings and hematite occurrences are determined by differences in soil maturity and temperature. Within watersheds underlain by two formations, differences in redness ratings and hematite occurrences are probably determined by differing fluxes of iron(III) released by primary mineral weathering and by differences in organic matter content (percent total carbon).

Soils of this study area are more goethitic than those of the Blue Ridge Front study area (Graham et al., 1989a; b). A comparison of the two study areas indicates that the average annual precipitation, relative stability of parent rock, size of primary minerals, and temperature of the Coweeta Basin may be less favorable for hematite formation. Hematite occurrences in the Blue Ridge Front site are believed to be controlled by almandine garnet distributions, however differences in parent rock stabilities and modal

abundances of iron-bearing primary minerals may also influence these occurrences.



## Appendix

Table 1. Environmental Variables At Each of the Nine Study Sites.

	36A	18A	18B	34A	34B	2B	2A
Wtshd type	contrl						
Bdrck type	tf	tf	tf	ck	tf	tf	tf
Bdrck dpth (cm)	120	56	111	165	96	91	100
Elevation (m)	1310	823	792	1184	1097	853	991
Aspect (°)	130	235	235	180	165	135	160
% Slope	40	54	60	41	35	38	45
Precip/yr (cm)	222	194	194	201	201	177	177
Vegetation	hardwd						
Soil Type	TD	HH	TH	TD	TD	TD	TH
Soil Srs	Edv/Ch	Trimnt	Evr/Cw	Chndlr	Chndlr	Chndlr	Fannin

	17A	1A
Wtshd type	dstrbd	dstrbd
Bdrck type	tf	ccr
Bdrck dpth (cm)	58	180
Elevation (m)	869	808
Aspect°	305	265
% Slope	53	37
Precip/yr	not ava	ilable
Vegetation	wht pn	wht pn
Soil Type	TH	TH
Soil Srs	Evr/Cw	Fannin

(Swank and Crossley, 1988; Swift et al., 1988; Browning and Thomas, 1985; Hatcher 1980)

## Key

Watrsh - watershed; contrl - control watershed; bdrck - bedrock; tf - Tallulah Falls Formation; ck - Carroll Knob Ultramafic Complex; precip/yr - average annual precipitation per year; hardwd - hardwood; wht pn - white pine; TD - Typic Dystrochrept; HH - Humic Hapludult; TH - Typic Hapludult; Srs - series; Edv/Ch - Ednyville/Chestnut Series; Trimnt - Trimont Series; Evr/Cw - Evard/Cowee Series; Chandlr - Chandler Series; Fannin Series; dstrbd - manipulated watershed; ccr - Coweeta Group Coleman River Formation.

Table 2. Parent Rock Point Count Data.

	1 <b>A</b> /C	oweet	a Co	leman	Riv	ver F	Orm	atio	on To	tal -	(ccr)
Or	tz		Ep			Gnt			Cz	1	Total
25			168		77			27			530
49	ક	-	32	<b>&amp;</b>		14%			5%	1	100%
			<del></del>		2.5		+6\				
Or	tz	1	Bio	!	174	A - ( Gnt		1	Or	. 1	Total
25			284			26		1	1		561
	.5%	- !	51%			5%			0.28	:	100.7%
					36	A - (	tf)				
Ortz		Epd		Cz	Ĭ.	Bio	<u> </u>	Gn	t	Ch	Total
337		122		25		4		55		8	551
61%	ļ	19%	1	4.5%		0.7%		109	<b>t</b>	1.5%	99.7%
					182	A - (	tf)				
Ortz	↓ P	la	Ksp		)p	Bi	<u> </u>	4	Gnt	Msc	Total
310		4	97	1 .	7	13			5 ]	7	603
51%	7	<b>%</b>	16%	1 1	₽.	2	28	:	18	18	99%
					181	B <b>-</b> (	tf)				<del></del>
	Plg	Ksp	Bi		git		S	1	QΩ	Cz	Total
93	8	254	16		5	.	5		4	2	537
178  1	.5%	478	31	<b>t</b>	15	<b>k</b>	1	8	18	0.2	99.7%
					341	B <b>-</b> (					
Ortz	P1					Epd			Augi	te B	
300	22			17 34		16		1	3		27   546
55%	4 %	23	8   3	38 68	\$	3%	1 0	. 2%	0.5	8   5	5%  99.7%
						- (1	f)				
Ortz		Ms		Ksr			n_	ļ	QΩ		Total
439		14		38		a .	9		3		543
81%	1	3%	1	7%		9	ક	1 (	0.5%	ı	100.5%
30	_	1 -		C8		-1C -	- (t		_	· · · · ·	n-4-1
Ms			rtz		Gi	nt	+	F	<del>2</del> 3	<del>-                                     </del>	Total 505
14 28.	-		88 7%		-	ን 4 %	ŀ		.6%		100%
20.	<b>√</b> 0	1 3	7 70	ı	Τ,	7 O	1	J	• • •	1	1009

Table 2. Parent Rock Point Count Data Con't.

			- 0				-			· · · ·	•			
								ormat						
Hrn	Pla	Ortz	Bio	Gnt	qO	Msc	Epd	CzC	<u>h   Px</u>	Ksp	Sl	An ]	<u>Fe</u>	Total
262	119	2156	615	208	15	165	182	32 2	8   11	515	5	49	2	4364
68	3%	49%	148	5%	.3	48	4 %	. 7   .	6 .3	12%	1.1	18	.1	100.1
						Ck 5	56 -	(ck)						
P	la	H:	rn l	Vo	id	Ort		Cla	<b>y</b> l	Cl	a	1 :	rot	al
34	7	8	4	7		29		23		10	)		50	
69.	48	16	.8%	1.	48	5.8	38	4.6	8	29	ţ		10	800
						Ck 4	2C -	- (ck)	)					
	tz		la		Ch_		gC		id	1 1	1sc			tal
	80		05		39		LO	1			37			00
21	.6%	4	18	2	7.8	:	28	0.	2%	;	7.48	;	1	.00%
						Ck 7	72 -	(ck)						
	lg		rn	<del> </del>	Fe			oid	1	<u>Ortz</u>			Cot	
9			75	1	24		1	2	1	12			50	
18	.18	74	. 4%		4.8	ક	0	.48	1	2.49	<b>k</b>	1	100	1.1%
								(ck)						
	<u>Plg</u>		<u>Hrn</u>		F	<u>'e</u>		Void		Ort	Z	<del></del>		tal
	86		361		_	27	1	4	- 1	22			_	00
	17.2	88	72.2	*	5	.48	1	0.8%	l	4.4	18	}	1	.00%
	1 -							ob To		•				
Msc		tz	Hrn		Plg	_	oid	_Ch	Cla			Op	I	otal
37	17		820		729		L4	149	23			10	_ ا	2011
1.8%	8.	8	41%		36%	10.	.78	7.48	1.1	<b>%</b> 2.6	5* 0	.5*	9	9.98
			·	Bl	ue R	idae	e Fr	ont S	chis	ts				
B	io	L	Msc	Ī		h		Ortz	Ī	Gnt	1	To	ota	1
2	2%		31%			8		35%		78			308	
				Ply	D D	anh i	Fre	ont Gr	o i s	202				
				DIU	16 W.	Lugo		Jiic Gi	16TD					
В	io	1	Msc	<u> </u>		h		Ortz		anet:	itel	To	ota	1

(after Graham et al., 1990b)

Key
Qrtz - quartz; Epd - epidote; Gnt - garnet; Cz Clinozoisite; Bio - biotite; Op - opaques; Ch - chlorite;
Plg - plagioclase feldspar; Ksp - potassium feldspar; Msc muscovite; Sl - sillimanite; An - anthophyllite; Fe - iron
oxides; Px - pyroxene.

Table 3. Soil pH.

Site	Depth (cm)	Trial 1	Trial 2	Trial 3	Ave	S. Dev.
36A1	24-48	5.7	5.7		5.7	N/A
36A1	90-120	6.1	6.1		6.1	N/A
17A1	18-36	4.3	4.4	4.5	4.4	0.1
17A1	36-58	5.2	5.2		5.2	N/A
18A1	22-56	4.6	4.5		4.5	N/A
18A1	56-62	4.5	4.5		4.5	N/A
18B2	26-41	4.8	4.7		4.7	N/A
18B2	93-111	5.4	5.3		4.4	N/A
34A3	17-30	4.5	4.5		4.5	N/A
34A3	85-120	4.6	4.5	4.5	4.5	0.06
34B3	30-60	5.3	5.3		5.3	N/A
34B3	80-90	5.7	5.8	5.7	5.7	0.1
<u>1A2</u>	30-43	5.0	5.0		5.0	N/A
1A2	101-120	5.7	5.6		5.7	N/A
2A1	30-50	5.2	5.4	5.4	5.3	0.15
2A1	92-100	6.0	6.0		6.0	N/A
<u>2B2</u>	33-48	4.7	4.7		4.7	N/A
2B2	64-91	5.3	5.4		5.3	N/A

Table 4. Total Soil Carbon.

					_			
Depth	Trial 1	Trial 2	Trial 3	Ave.	S	Dev	% TC	% SD
(cm)	(q/kq)	(a/ka)	(q/kq)	(a/ka)				
24-48	8.0	10.0	10.0	9.0		1.0	0.9	0.1
90-120	2.0	2.0	2.0	2.0		0.1	0.2	0.0
18-36	11.0	12.0	10.0	11.0		1.0	1.1	0.1
36-58	7.0	6.0	7.0	6.0		0.5	0.7	0.1
22-56	10.0	11.0	11.0	11.0		0.2	1.1	0.0
56-62	19.0	21.0	20.0	20.0		0.6	2.0	0.0
26-41	5.0	4.0	4.0	4.0		0.4	0.5	0.0
93-111	3.0	2.0	2.0	3.0		0.0	0.3	0.0
17-30	25.0	25.0	25.0	25.0		0.3	2.5	0.0
85-120	2.0	3.0	2.0	2.0		0.3	0.3	0.0
30-60	37.0	36.0	38.0	37.0		1.0	3.7	0.1
80-90	6.0	7.0	6.0	6.0		0.2	0.6	0.0
30-43	9.0	9.0	8.0	8.0		0.8	0.9	0.1
101-120	2.0	2.0	2.0	2.0		0.0	0.2	0.0
30-50	3.0	3.0	3.0	3.0		0.3	0.3	0.0
92-100	1.0	1.0	1.0	1.0		0.3	0.1	0.0
33-48	6.0	6.0	7.0	7.0		0.2	0.7	0.0
64-91	2.0	2.0	2.0	2.0		0.2	0.2	0.0
	(cm) 24-48 90-120 18-36 36-58 22-56 56-62 26-41 93-111 17-30 85-120 30-60 80-90 30-43 101-120 30-50 92-100 33-48	(cm)         (g/kg)           24-48         8.0           90-120         2.0           18-36         11.0           36-58         7.0           22-56         10.0           56-62         19.0           26-41         5.0           93-111         3.0           17-30         25.0           85-120         2.0           30-60         37.0           80-90         6.0           30-43         9.0           101-120         2.0           30-50         3.0           92-100         1.0           33-48         6.0	(cm)         (g/kg)         (g/kg)           24-48         8.0         10.0           90-120         2.0         2.0           18-36         11.0         12.0           36-58         7.0         6.0           22-56         10.0         11.0           56-62         19.0         21.0           26-41         5.0         4.0           93-111         3.0         2.0           17-30         25.0         25.0           85-120         2.0         3.0           30-60         37.0         36.0           80-90         6.0         7.0           30-43         9.0         9.0           101-120         2.0         2.0           30-50         3.0         3.0           92-100         1.0         1.0           33-48         6.0         6.0	(cm)         (g/kg)         (g/kg)         (g/kg)           24-48         8.0         10.0         10.0           90-120         2.0         2.0         2.0           18-36         11.0         12.0         10.0           36-58         7.0         6.0         7.0           22-56         10.0         11.0         11.0           56-62         19.0         21.0         20.0           26-41         5.0         4.0         4.0           93-111         3.0         2.0         2.0           17-30         25.0         25.0         25.0           85-120         2.0         3.0         2.0           30-60         37.0         36.0         38.0           80-90         6.0         7.0         6.0           30-43         9.0         9.0         8.0           101-120         2.0         2.0         2.0           30-50         3.0         3.0         3.0           92-100         1.0         1.0         1.0           33-48         6.0         6.0         7.0	(cm)         (g/kg)         (g/kg)         (g/kg)         (g/kg)           24-48         8.0         10.0         10.0         9.0           90-120         2.0         2.0         2.0         2.0           18-36         11.0         12.0         10.0         11.0           36-58         7.0         6.0         7.0         6.0           22-56         10.0         11.0         11.0         11.0           56-62         19.0         21.0         20.0         20.0           26-41         5.0         4.0         4.0         4.0           93-111         3.0         2.0         2.0         3.0           17-30         25.0         25.0         25.0         25.0           85-120         2.0         3.0         2.0         2.0           30-60         37.0         36.0         38.0         37.0           80-90         6.0         7.0         6.0         6.0           30-43         9.0         9.0         8.0         8.0           101-120         2.0         2.0         2.0         2.0           30-50         3.0         3.0         3.0         3.0	(cm)         (g/kg)         (g/kg)         (g/kg)         (g/kg)           24-48         8.0         10.0         10.0         9.0           90-120         2.0         2.0         2.0         2.0           18-36         11.0         12.0         10.0         11.0           36-58         7.0         6.0         7.0         6.0           22-56         10.0         11.0         11.0         11.0           56-62         19.0         21.0         20.0         20.0           26-41         5.0         4.0         4.0         4.0           93-111         3.0         2.0         2.0         3.0           17-30         25.0         25.0         25.0         25.0           85-120         2.0         3.0         2.0         2.0           30-60         37.0         36.0         38.0         37.0           80-90         6.0         7.0         6.0         6.0           30-43         9.0         9.0         8.0         8.0           101-120         2.0         2.0         2.0         2.0           30-50         3.0         3.0         3.0         3.0	(cm)         (g/kg)         (g/kg)         (g/kg)         (g/kg)           24-48         8.0         10.0         10.0         9.0         1.0           90-120         2.0         2.0         2.0         2.0         0.1           18-36         11.0         12.0         10.0         11.0         1.0           36-58         7.0         6.0         7.0         6.0         0.5           22-56         10.0         11.0         11.0         11.0         0.2           56-62         19.0         21.0         20.0         20.0         0.6           26-41         5.0         4.0         4.0         4.0         0.4           93-111         3.0         2.0         2.0         3.0         0.0           17-30         25.0         25.0         25.0         25.0         0.3           85-120         2.0         3.0         2.0         2.0         0.3           80-90         6.0         7.0         6.0         6.0         0.2           30-43         9.0         9.0         8.0         8.0         0.8           101-120         2.0         2.0         2.0         2.0	(cm)         (g/kg)         (g/kg)         (g/kg)         (g/kg)           24-48         8.0         10.0         10.0         9.0         1.0         0.9           90-120         2.0         2.0         2.0         2.0         0.1         0.2           18-36         11.0         12.0         10.0         11.0         1.0         1.1           36-58         7.0         6.0         7.0         6.0         0.5         0.7           22-56         10.0         11.0         11.0         11.0         0.2         1.1           56-62         19.0         21.0         20.0         20.0         0.6         2.0           26-41         5.0         4.0         4.0         4.0         0.4         0.5           93-111         3.0         2.0         2.0         3.0         0.0         0.3           17-30         25.0         25.0         25.0         25.0         0.3         0.3           85-120         2.0         3.0         3.0         3.0         0.0         0.3         0.3           80-90         6.0         7.0         6.0         6.0         0.2         0.6

Table 5. Soil Particle Size Analyses.

	1 5 44 ( )	1 0 0 1	1 0 0:34	1 9 03 1
Site	Depth (cm)	% Sand	% Silt	% Clay
36A	24-48	77.5	15.0	7.5
		82.5	12.5	5.0
		av.=80.0	av.= 13.8	av.=6.3
	90-120	65.0	12.5	25.0
		85.0	10.0	20.0
		av.= 75.0	11.3	av.= 22.5
17A	18-36	62.5	22.5	20.0
		67.5	25.0	7.5
		67.5	25.0	7.5
		av.= 65.8	av.= 24.2	av.= 10.0
	36-56	55.0	25.0	20.0
		70.0	20.0	10.0
		62.5	25.0	12.5
		av.= 62.5	av.= 23.3	av.= 14.2
18A	22-56	57.5	25.0	17.5
		72.5	20.0	7.5
		65.0	21.3	13.7
	ļ	av.= 65.0	av.= 10.8	av.= 22.1
	56-62	62.5	27.5	10.0
		72.5	17.5	10.0
		65.0	20.0	12.5
		av.=67.5	av.= 21.7	av.= 10.8
18B	26-41	62.5	20.0	17.5
		45.0	32.5	22.5
	İ	64.0	18.0	18.0
		av.=57.2	av.= 23.5	av.= 19.3
	93-111	65.0	15.0	20.0
		70.0	15.0	15.0
	Ì	av = 67.5	av.= 15.0	av.= 17.5
34A	17-30	75.0	17.5	7.5
		62.5	25.0	12.5
	İ	57.5	26.2	16.3
		av = 65.0	av = 22.9	12.1
	85-120	66.3	21.3	12.5
		72.5	20.0	7.5
		av = 69.4	av = 20.6	av.= 10.0
34B	30-60	52.5	21.3	26.2
J.D				
	80-90	65.0	12.5	22.5
		80.0	15.0	5.0
		av.= 72.5	av.= 13.8	av.= 13.8
1A	30-43	65.0	20.0	15.0
	1 30 43	40.0	25.0	35.0
		57.5	25.0	17.5
	<b>†</b>	av.= 54.2	av = 23.3	av.= 22.5
	<del></del>	104 24.C	18A 53 . 3	144 66.J

Table 5. Particle Size Analyses, Con't.

Site	Depth (cm)	% Sand	% Silt	% Clay
	1			
1 <b>A</b>	101-120	65.0	20.0	15.0
	1	40.0	20.0	40.0
		60.0	17.5	22.5
		av.= 55.0	av.= 19.2	av.= 25.8
2A	30-50	62.5	27.5	10.0
		42.5	11.3	46.2
		56.3	16.2	27.5
		av.= 53.8	av.= 18.4	av.= 27.9
	92-100	63.8	7.5	27.5
	İ	82.5	12.5	5.0
		av.= 73.1	av.= 10.0	av.= 8.2
2B	33-48	42.5	22.5	35.0
		37.5	22.5	40.0
		37.5	21.3	41.2
		av.= 39.2	av.= 22.1	av.= 38.8
	64-91	47.5	17.5	35.0
		45.0	20.0	35.0
		37.5	12.5	40.0
	İ	av.= 43.3	av.= 16.7	av.= 36.7
<u> </u>	(2 0 - 0 E =		002 == 1	

sand = (2.0 - 0.5 mm), clay = (<0.002 mm), silt = (0.05 - 0.0002 mm)

Table 6. Soil Colors.

Donth	Pulk Coil	NaOU-troated	DCB-treated
(Cm)	(Mer color)		(dry color)
24-48	10YR 5/3	10YR 7/4	10YR 8/1
90-120	10YR 5/4	10YR 8/4	N/A
18-36	7.5YR 5/6	7.5YR 7/8	10YR 8/1
36-58	7.5YR 4/6	7.5YR 7/6	N/A
22-56	5YR 4/6	7.5YR 6/6	10YR 8/1
56-62	7.5YR 4/6	7.5YR 7/8	N/A
26-41	7.5YR4/6	7.5YR 7/6	N/A
93-111	7.5YR 5/8	7.5YR 7/6	N/A
17-30	5YR 4/6	7.5YR 7/8	N/A
85-120	7.5YR 5/6	7.5YR 7/6	N/A
30-60	7.5YR 3/2	7.5YR 5/4	N/A
80-96	10YR 4/3	7.5YR 7/6	N/A
30-43	7.5YR 5/8	7.5YR 7/6	N/A
101-120	7.5YR 5/8	7.5YR 7/6	N/A
30-50	7.5YR 5/8	7.5YR 6/8	N/A
92-100	10YR 5/4	7.5YR 7/6	10YR 8/1
33-58	2.5YR 4/8	5YR 7/8	N/A
64-91	5YR 4/6	7.5YR 7/6	N/A
	90-120 18-36 36-58 22-56 56-62 26-41 93-111 17-30 85-120 30-60 80-96 30-43 101-120 30-50 92-100 33-58	(cm)         (wet color)           24-48         10YR 5/3           90-120         10YR 5/4           18-36         7.5YR 5/6           36-58         7.5YR 4/6           22-56         5YR 4/6           56-62         7.5YR 4/6           93-111         7.5YR 5/8           17-30         5YR 4/6           85-120         7.5YR 5/6           30-60         7.5YR 3/2           80-96         10YR 4/3           30-43         7.5YR 5/8           101-120         7.5YR 5/8           30-50         7.5YR 5/8           92-100         10YR 5/4           33-58         2.5YR 4/8	(cm)         (wet color)         (dry color)           24-48         10YR 5/3         10YR 7/4           90-120         10YR 5/4         10YR 8/4           18-36         7.5YR 5/6         7.5YR 7/8           36-58         7.5YR 4/6         7.5YR 7/6           22-56         5YR 4/6         7.5YR 7/8           26-41         7.5YR 4/6         7.5YR 7/6           93-111         7.5YR 5/8         7.5YR 7/6           17-30         5YR 4/6         7.5YR 7/6           30-60         7.5YR 5/6         7.5YR 7/6           30-60         7.5YR 3/2         7.5YR 5/4           80-96         10YR 4/3         7.5YR 7/6           30-43         7.5YR 5/8         7.5YR 7/6           30-50         7.5YR 5/8         7.5YR 7/6           30-50         7.5YR 5/8         7.5YR 7/6           30-58         2.5YR 4/8         5YR 7/8

Table 7. Redness Ratings of NaOH-treated Clays.

2B	33-48	5.7	2B	64-91	2.1
2A	30-50	3.3	2A	92-100	0.0
1A	30-43	2.1	1A	101-120	2.1
34B	30-60	2.0	34B	80-90	2.1
34A	17-30	2.9	34A	85-120	2.1
18B	22-41	2.1	18B	93-111	2.1
18A	22-56	2.5	18A	56-62	2.1
17A	18-36	2.9	17A	36-58	2.1
36A	24-48	0.0	36A	90-130	0.0
Site	Depth	*RR	Site	Depth	*RR

\*RR =  $(10 - \dot{Y}R \text{ Hue}) \times (chroma)/(value)$ , (Torrent et al., 1983).

Table 8. Goethite and Hematite in the Blue Ridge Front Study Area.

	% Gt	% Gt + Ht	% Ht (Bt Horizons)
Non-almandine	13.4	13.4	0.0
Colluvium	14.1	14.1	0.0
	14.4	14.4	0.0
Almandine	13.3	17.1	1.6
Colluvium	14.9	19.0	0.0
30224724	16.5	20.9	0.0
	16.8	21.1	0.0
	17.1	21.2	0.0
	19.3	21.5	0.0
Non-almandine Residuum	14.2	16.1	1.9
Almandine	18.5	23.1	4.6
Residuum	19.6	23.9	5.3
Vesidam	19.9	24.9	7.9
	20.8	27.8	'''
	22.2	29.7	
		23.,	

(after Graham et al., 1989b)

Table 9. Comparison of the Coweeta Basin and the Blue Ridge Front Study Areas.

	<u>-</u>	
	Blue Ridge Front	Coweeta Basin
Mean Annual Temperature (°C)	10.0	12.6
Temperature Extremes (°C)	34.0 to -24.0	23.0 to -4.0
Mean Annual Precipitation (cm)	140.0	165.2
Elevation Range (m)	550 - 1040	675 - 1592
Slope Range (percent)	10 - 75	10 - 90

(afer Graham et al., 1989 a, b; 1990 a, b; Swift et al., 1988; Swank and Crossley, 1988)

Figure 1. Study area and sample site locations.

- \_.\_ Creek
- --- Watershed Boundary
- \_\_\_ Laboratory Boundary

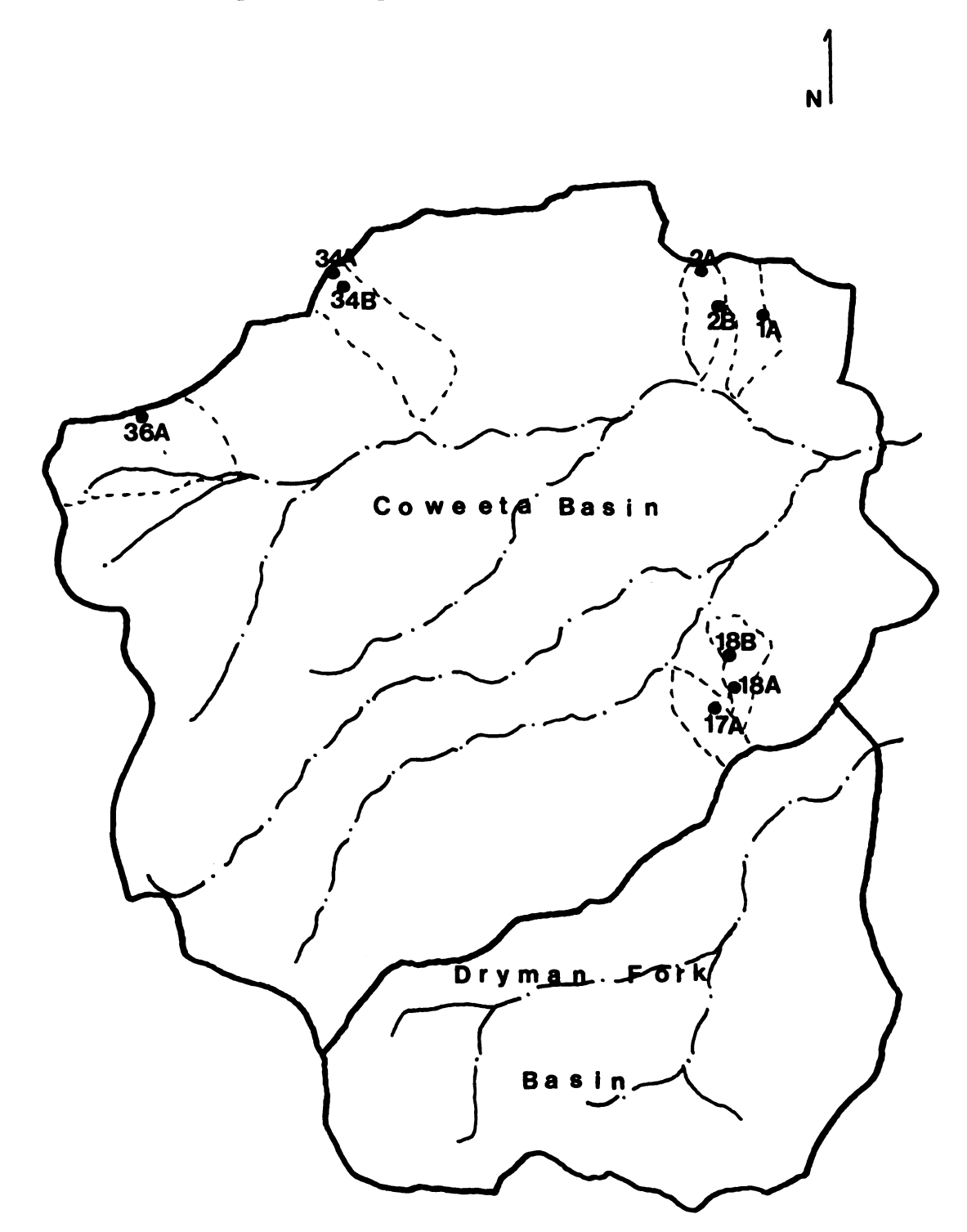
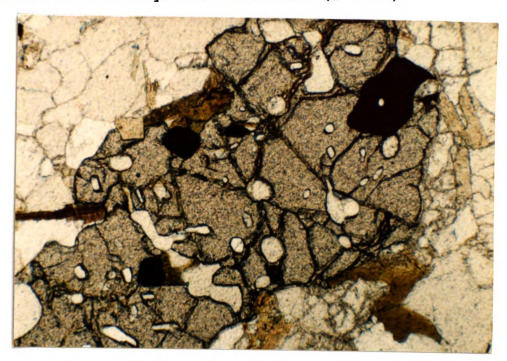


Figure 2. Embayed, inclusion-rich garnet grain with radial fractures around quartz inclusions (# 2A92).



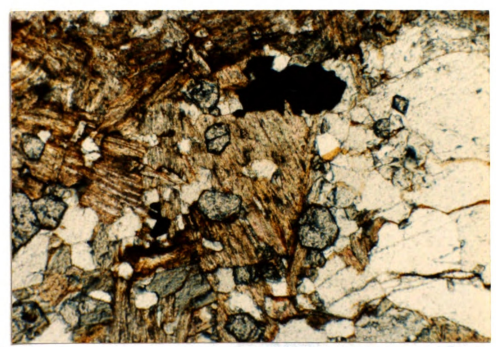


Figure 3. Continuous surface layers around euhedral, inclusion-poor garnet grains (# 36A92).

Figure 4. Fractures in garnet formed as a result of directed pressure (# 17A92).





Figure 5. Garnet weathering in contact with biotite.

(Fractures formed as a result of directed pressure. # 2A92)

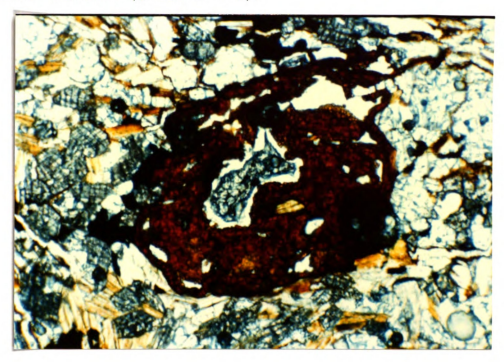
Figure 6. Limonitic surface layers in contact with garnet remnant (# C80-2-4-4).





Figure 7. Embayed, inclusion-rich garnet grain weathering in contact with chlorite (# 34B92).

Figure 8. Limonitic surface layer not in contact with garnet remnant (# C80-2-4-4).



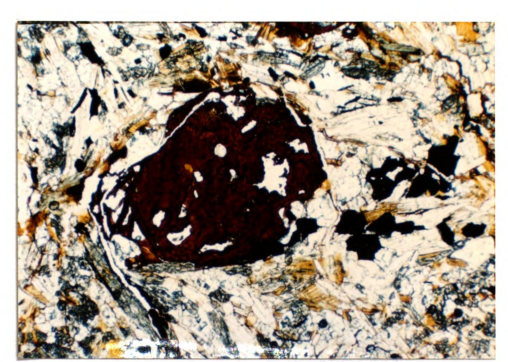
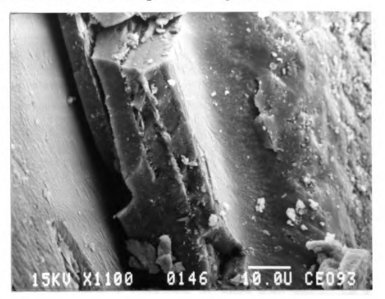


Figure 9. Limonitic pseudomorph after garnet (# C80-2-4-4).

Figure 10. "Onion skin-like" appearance of Type 1 protective surface layers on garnet.



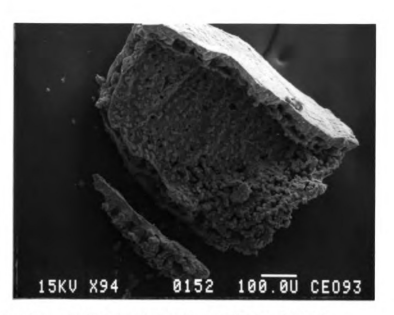
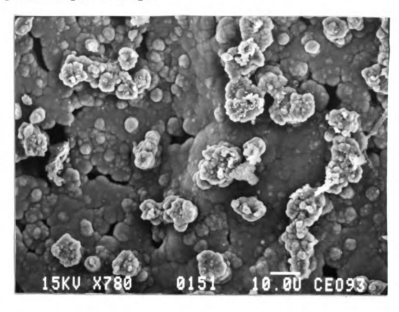


Figure 11. Garnet Type 2 surface layer.

Figure 12. Close view of garnet Type 2 surface layer showing microporosity.



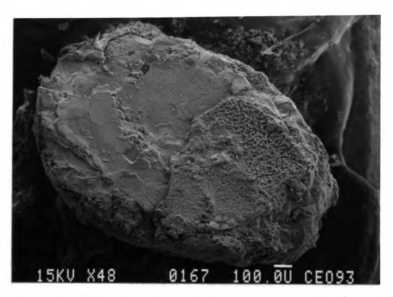


Figure 13. Inner surface of a garnet grain with a type 2 surface layer.

Figure 14. Strong parallelism in etch pits (foreground) and product "casts" (upper center) on garnet.



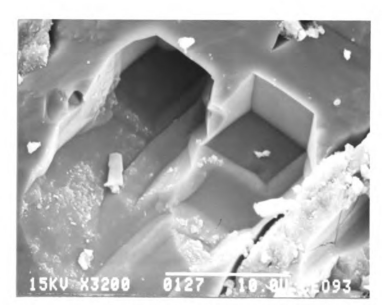
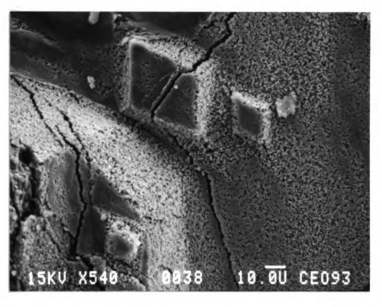


Figure 15. Dodecahedral etch pits on garnet.

Figure 16. Etch pits covered by secondary products on garnet.



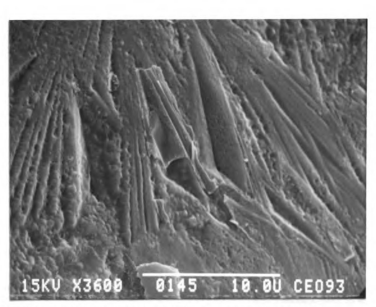
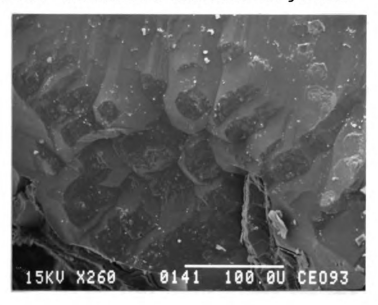


Figure 17. Elongate strings on garnet.

Figure 18. Mammilated surfaces on garnet.



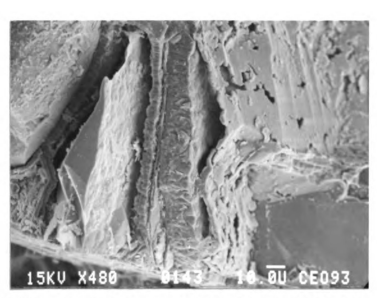
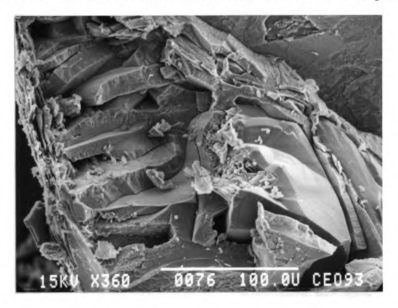


Figure 19. Boxwork and central partings on garnet.

Figure 20. Boxwork and faceted surfaces on garnet.



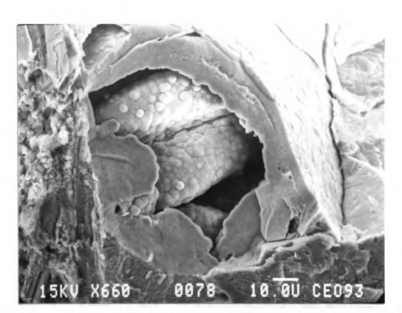
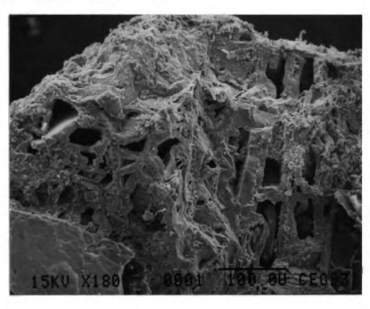


Figure 21. Boxwork and lace-like secondary products on garnet.

Figure 22. Boxwork and void space on a garnet grain removed from the upper horizons.



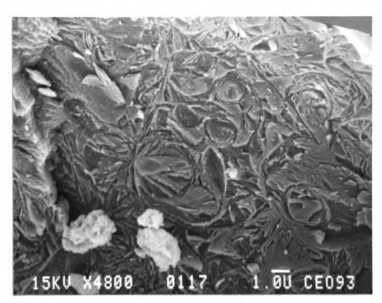
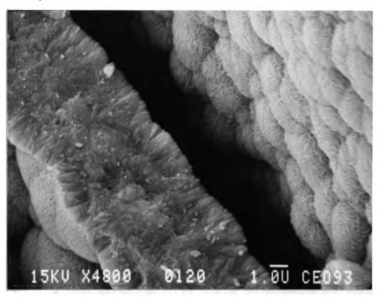


Figure 23. Lace-like secondary products on garnet.

Figure 24. Spheroidal secondary products forming boxwork septa on garnet.



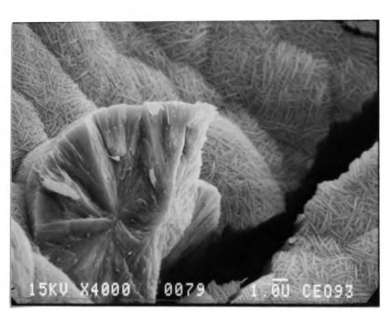


Figure 25. External and internal structure of spheroidal secondary products on garnet.

Figure 26. Skeletal secondary products forming fracture fillings on garnet.

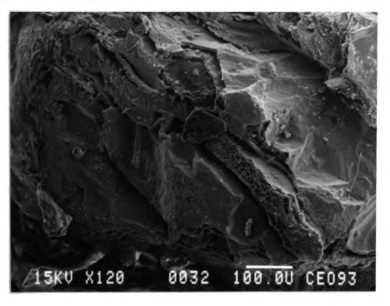


Figure 27. X-ray diffraction pattern of garnet from site 36A.

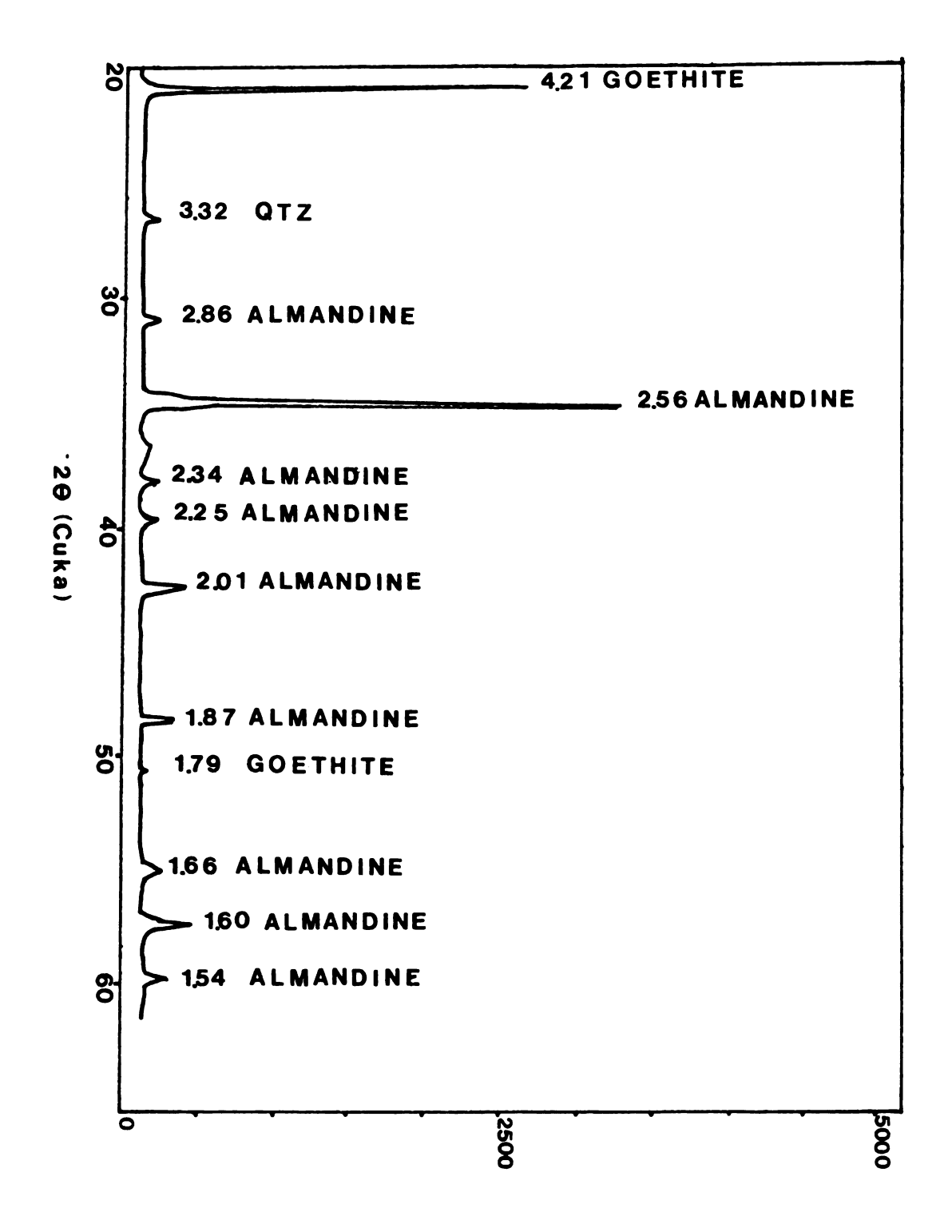


Figure 28. X-ray diffraction pattern of garnet from site 18B.

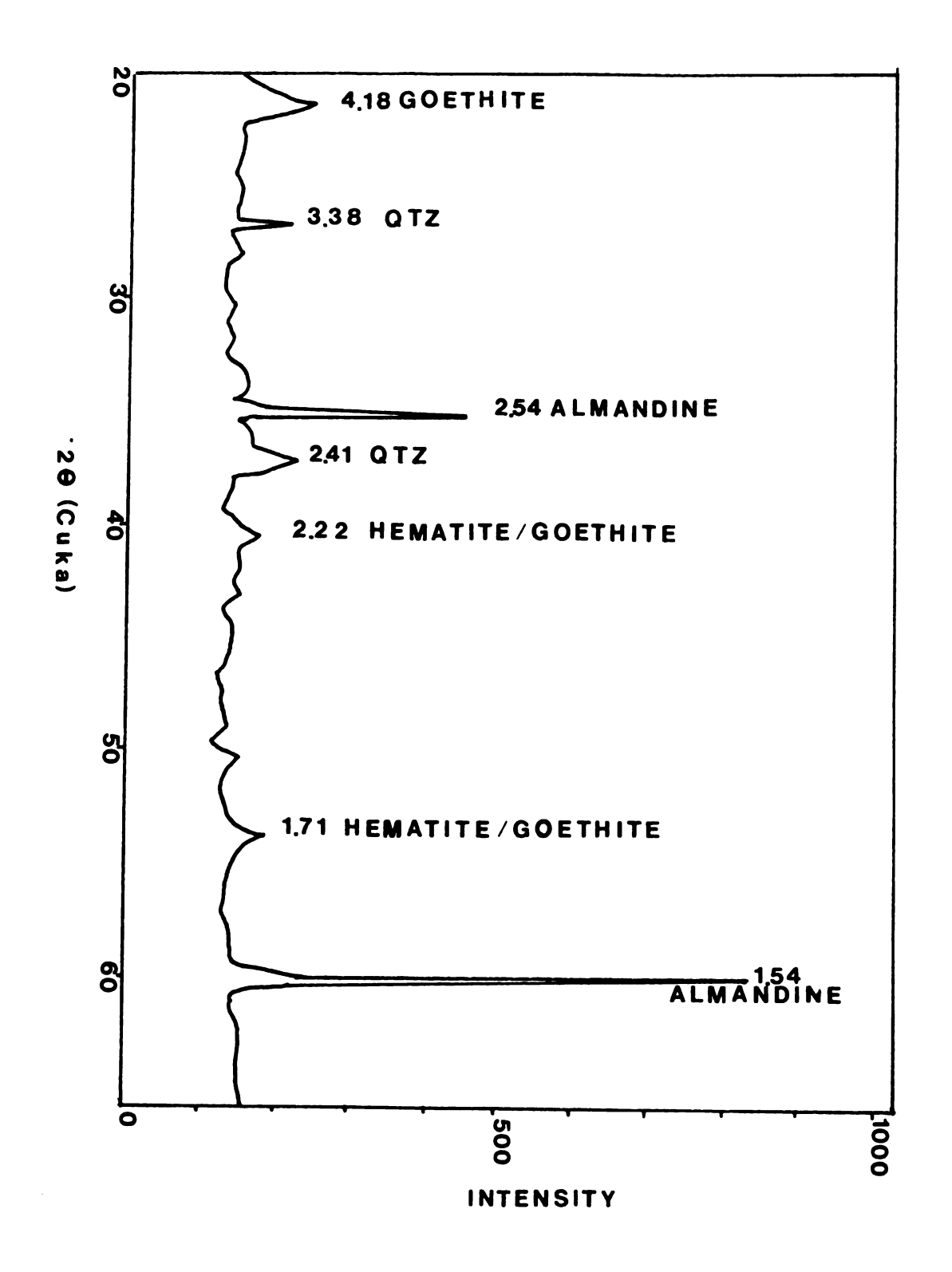
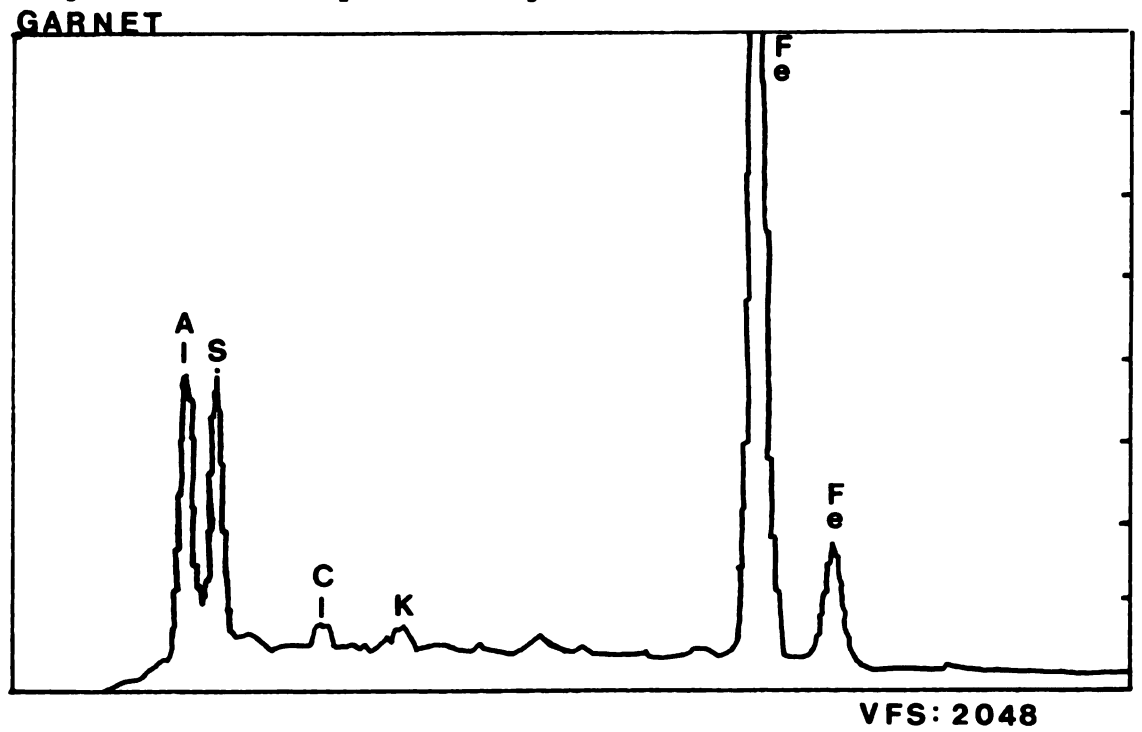


Figure 29. EDS spectra of garnet.



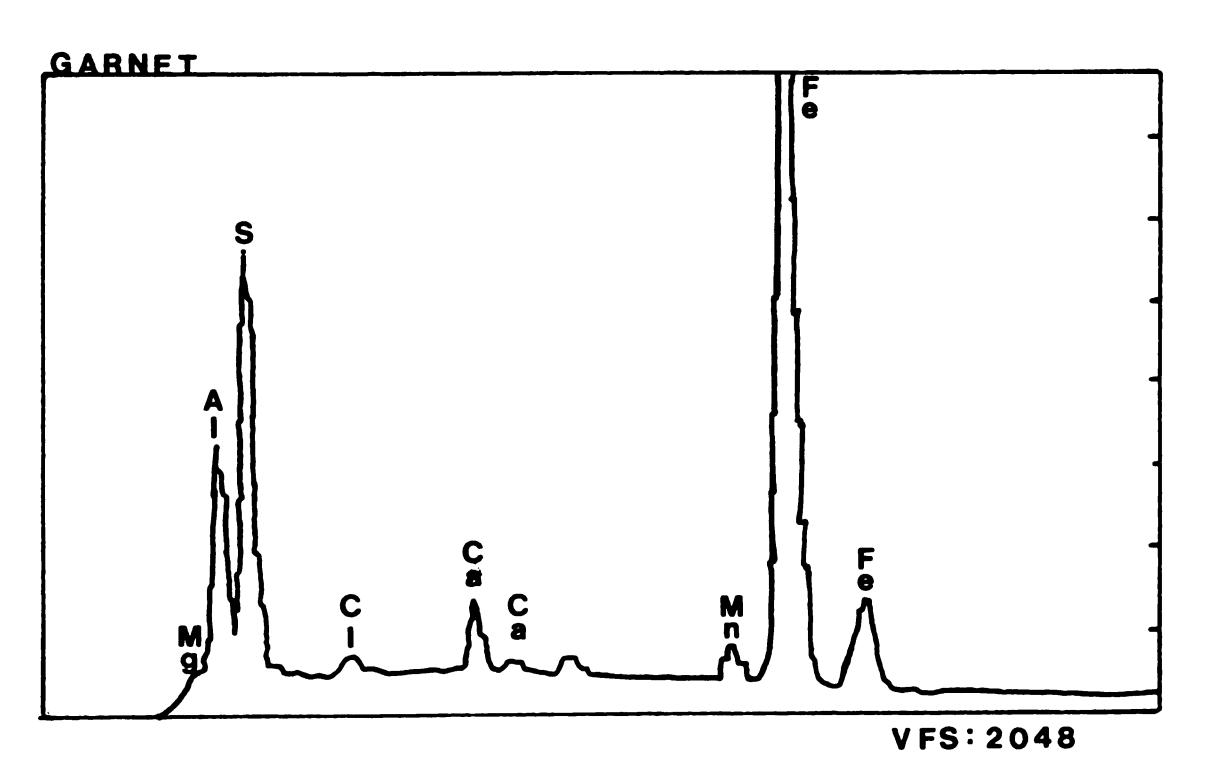
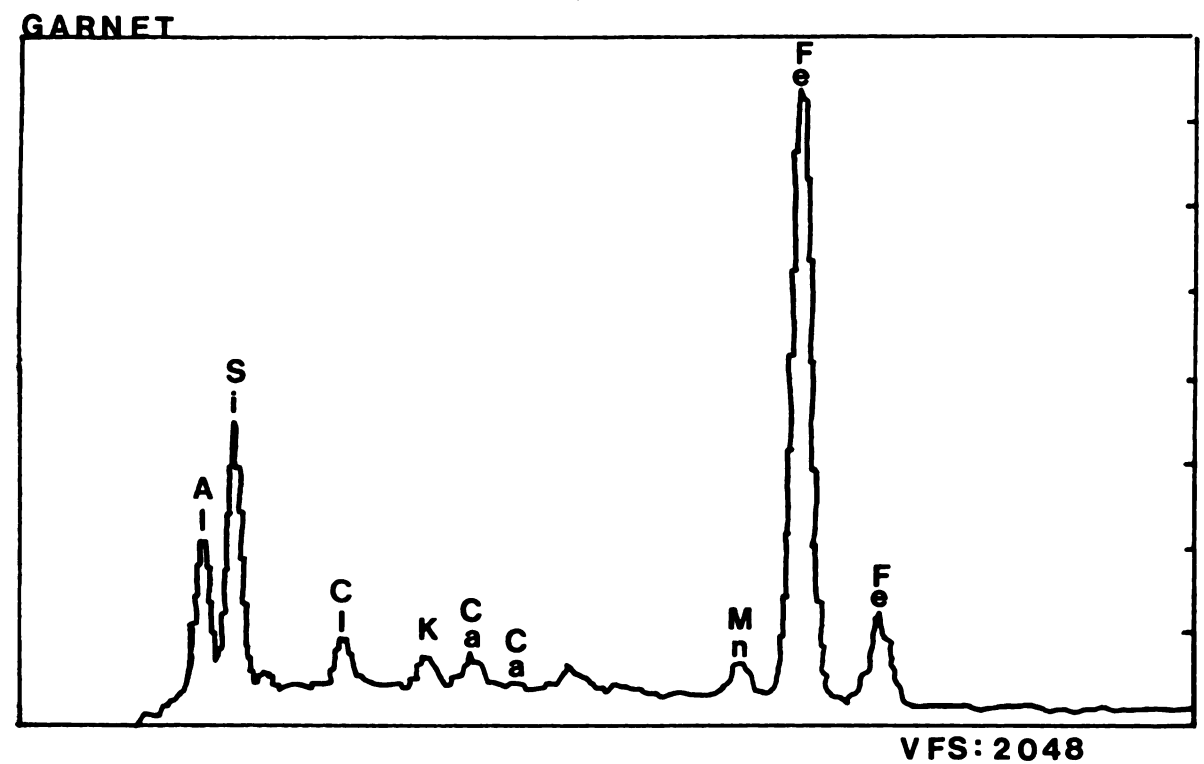


Figure 30. EDS spectra of garnet.

Figure 31. EDS spectra of garnet.



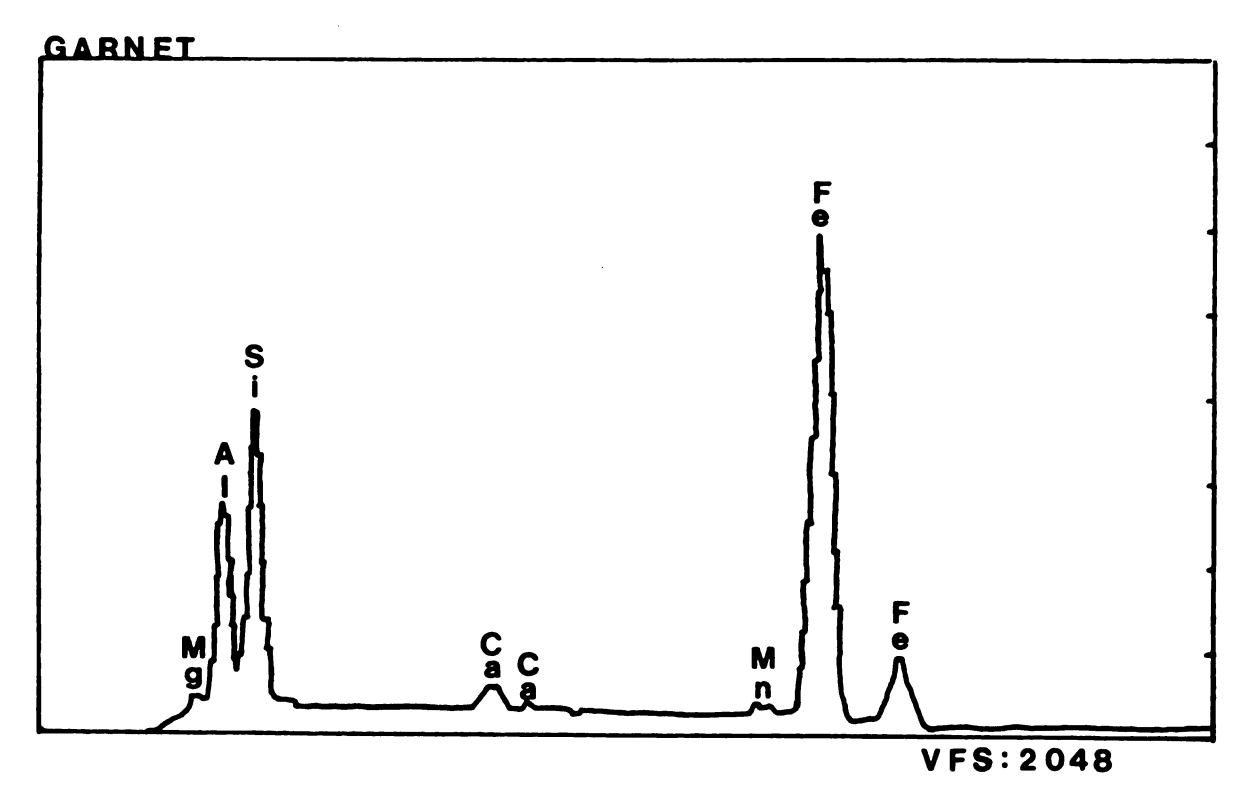
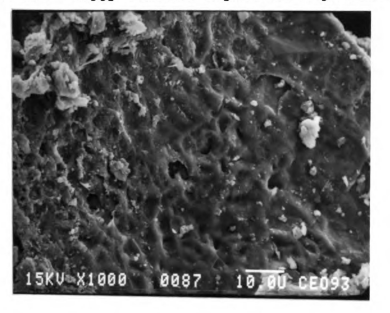


Figure 32. EDS spectra of garnet.

Figure 33. Vuggy surface layers on magnetite.



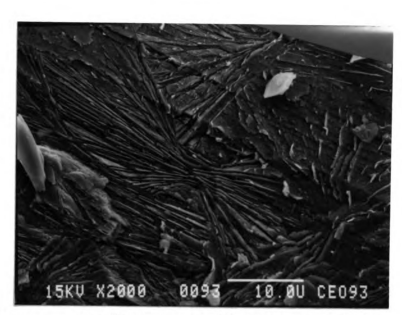


Figure 34. Exsolution lamellae on magnetite.

Figure 35. Exsolution lamellae on magnetite.



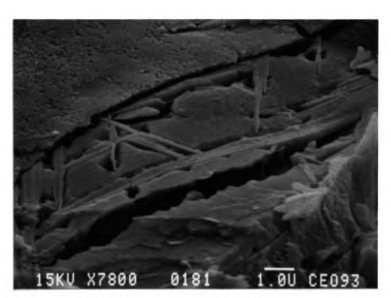
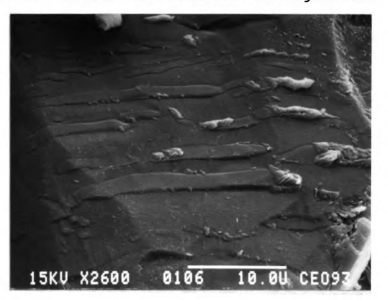


Figure 36. Exsolution lamellae on magnetite.

Figure 37. Exsolution lamellae on magnetite.



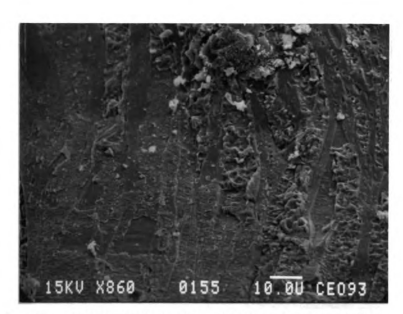


Figure 38. Exsolution lamellae on magnetite.

Figure 39. Leaf-like secondary products on magnetite.

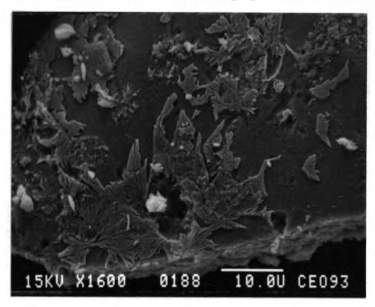
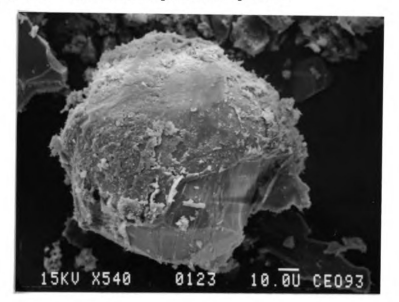




Figure 40. Lace-like secondary products on magnetite.

Figure 41. Coated magnetite grain.



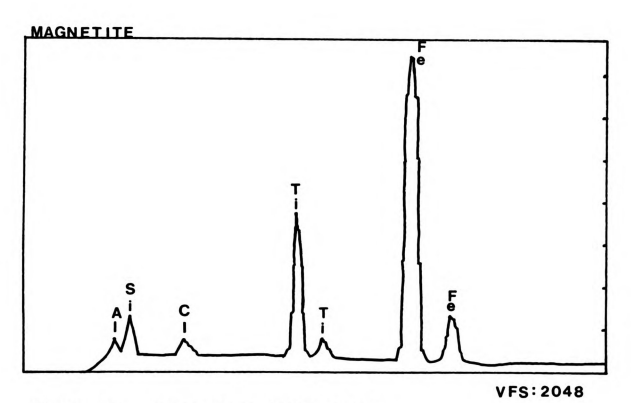


Figure 42. EDS spectra of magnetite.

Figure 43. X-ray diffraction pattern of chlorite. CHLORITE

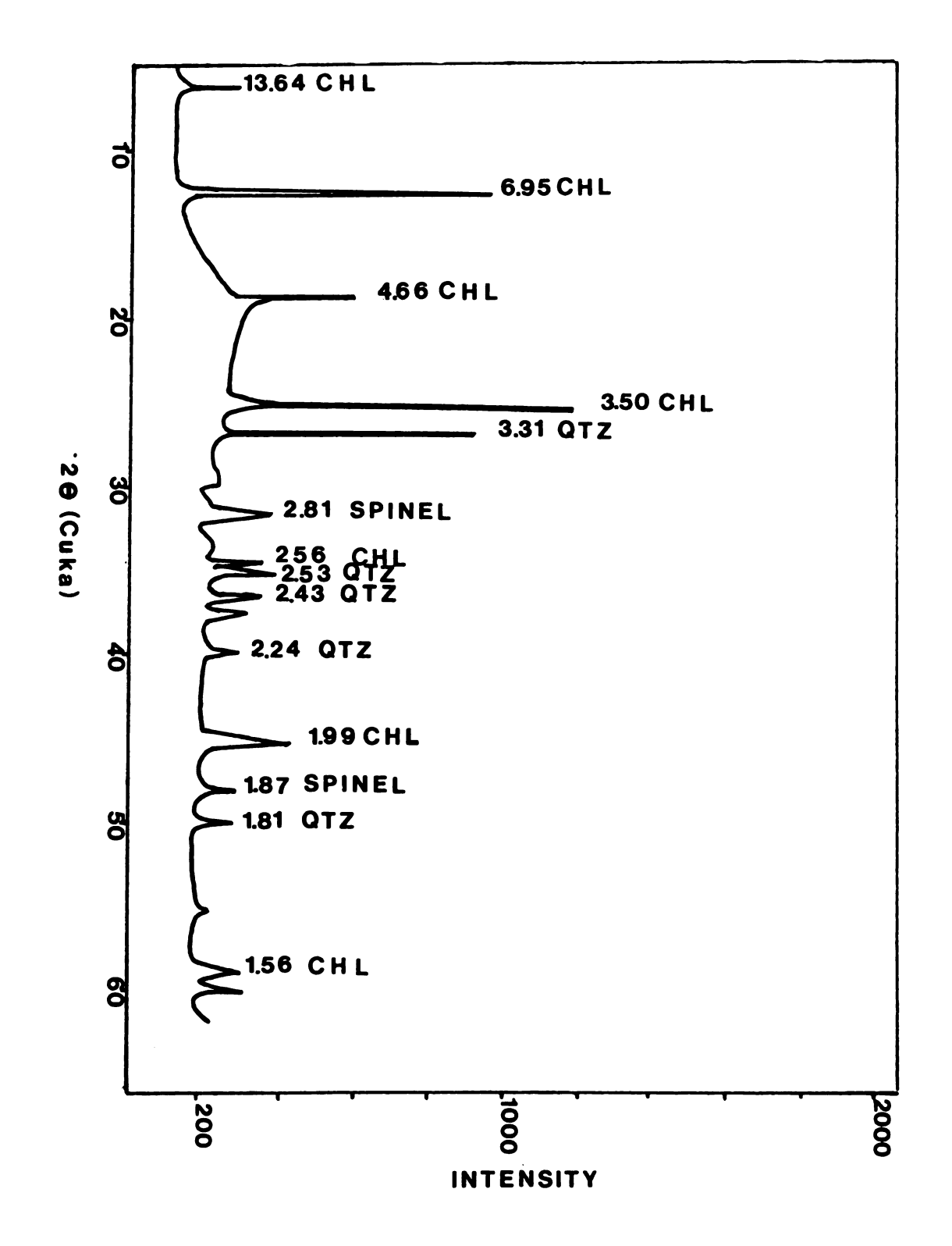


Figure 44. X-ray diffraction pattern of biotite.

## BIOTITE

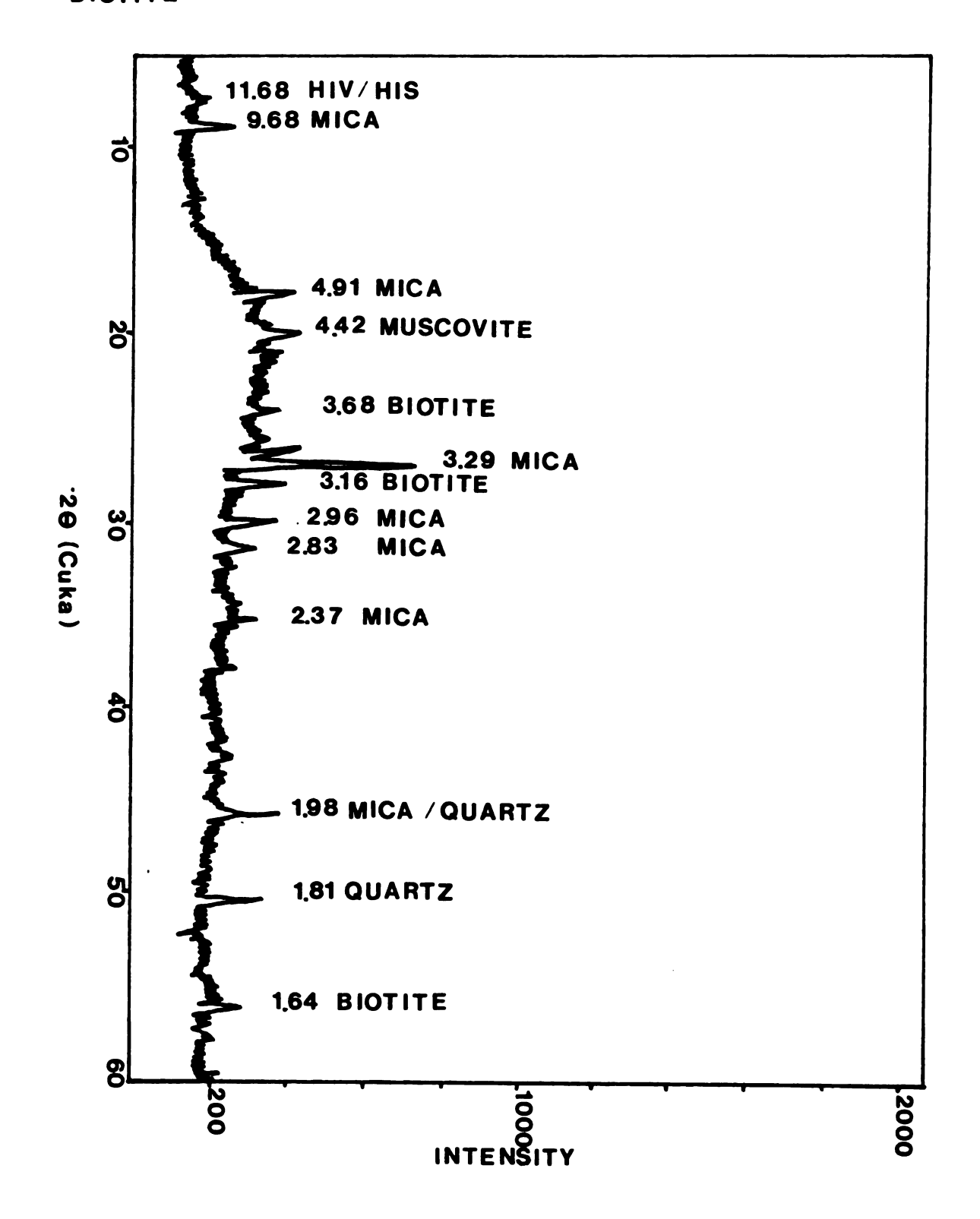
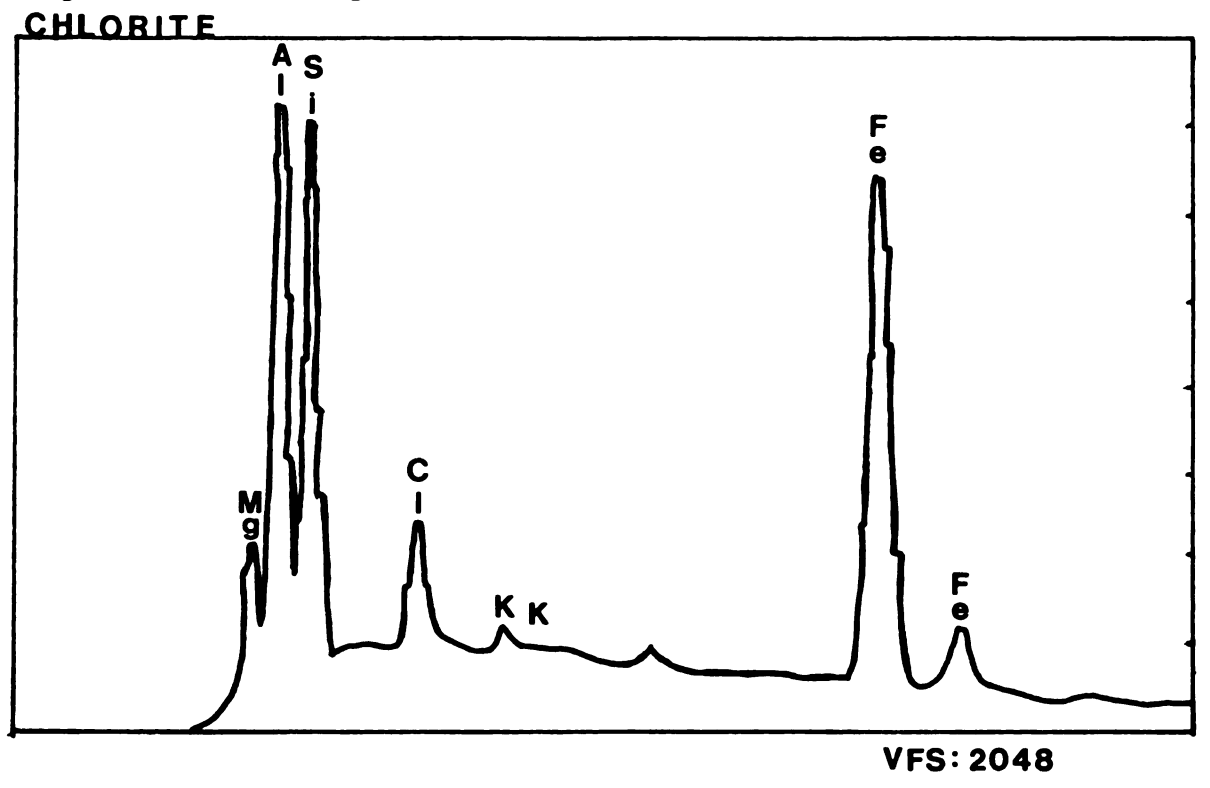


Figure 45. EDS spectra of chlorite.



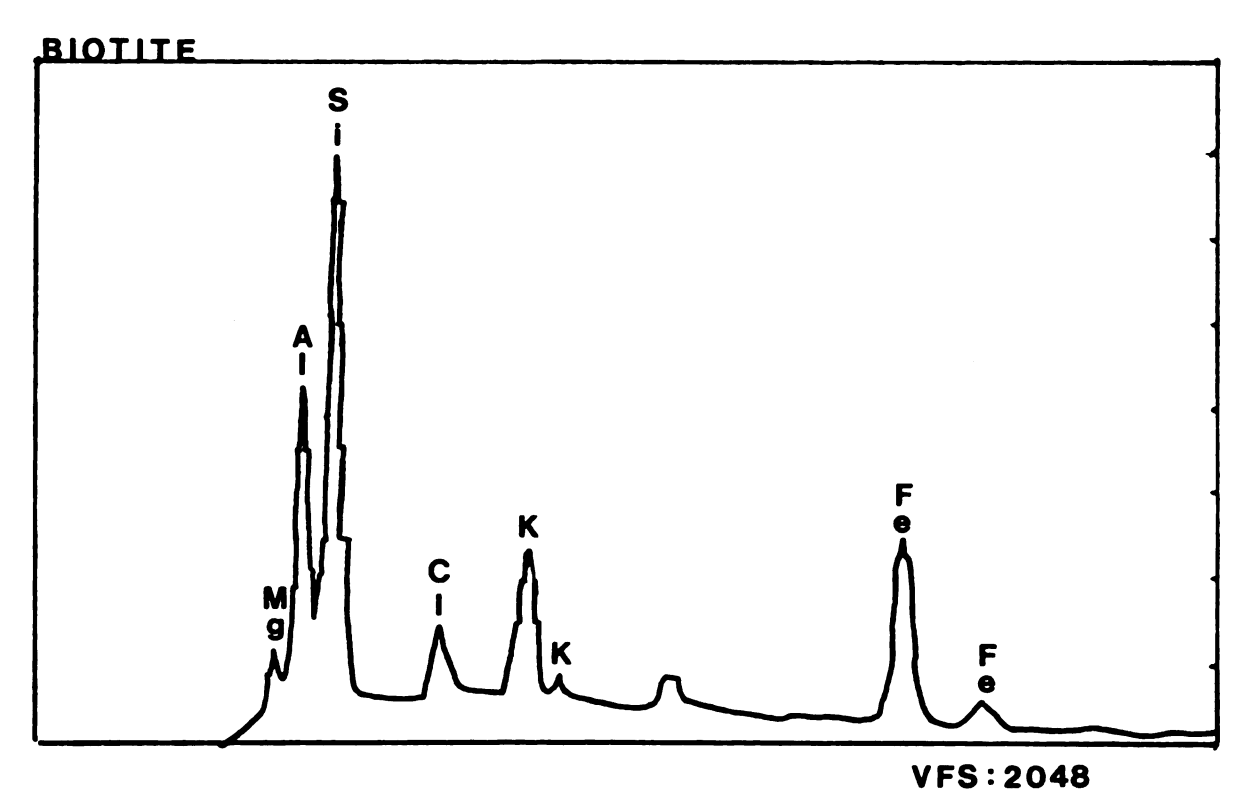


Figure 46. EDS spectra of biotite.

Figure 47. X-ray diffraction pattern of pyribole.

Amphibole/Pyroxene

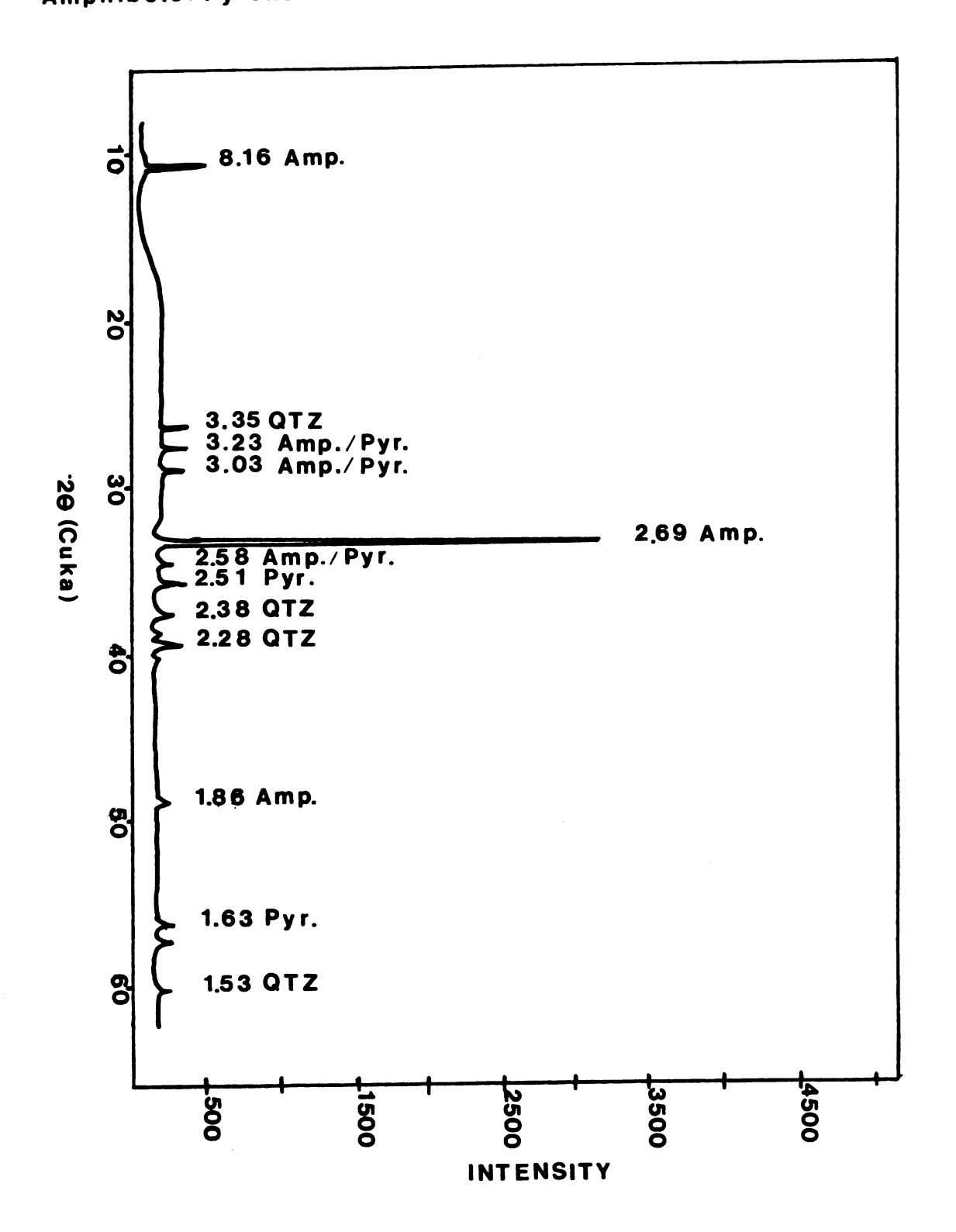


Figure 48. EDS spectra of amphibole.

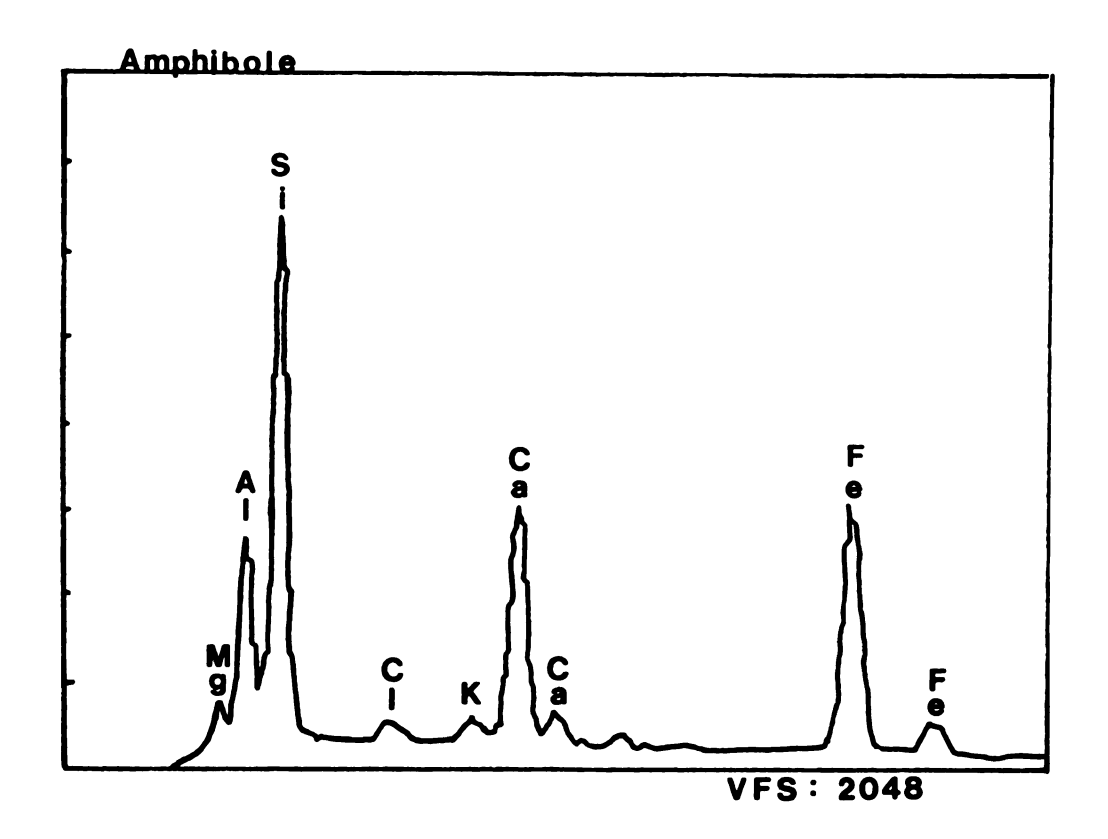
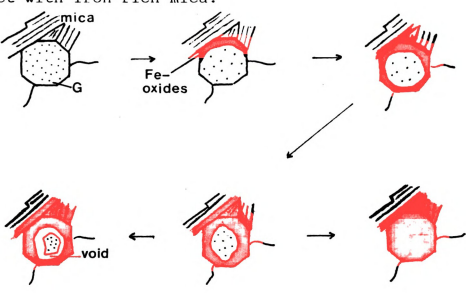


Figure 49. Schematic representation of garnet weathering in contact with iron-rich mica.



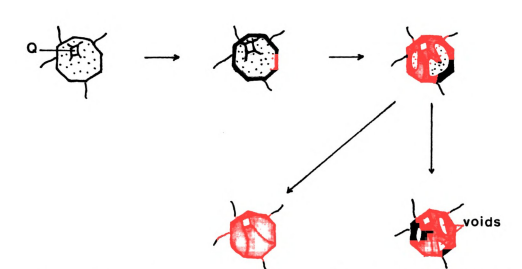
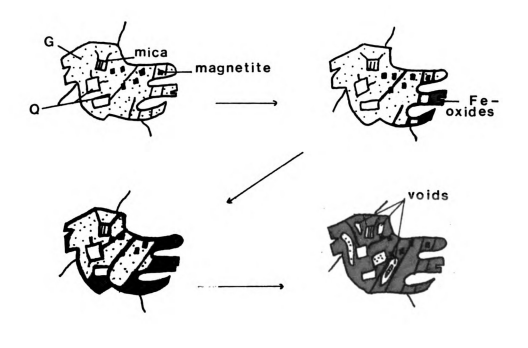


Figure 50. Schematic representation of garnet weathering without contact with iron-rich mica.

Figure 51. Schematic representation of embayed, inclusionrich garnet weathering.



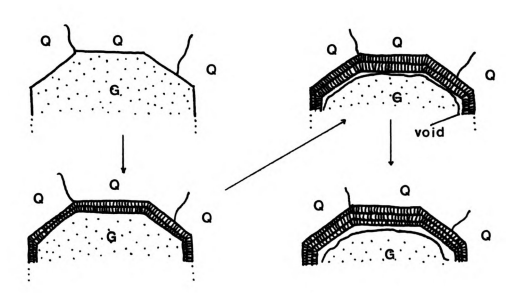


Figure 52. Schematic representation of Type 1 surface layer and peripheral void space formation.

Figure 53. Etch pits under Type 1 protective surface layer on garnet.

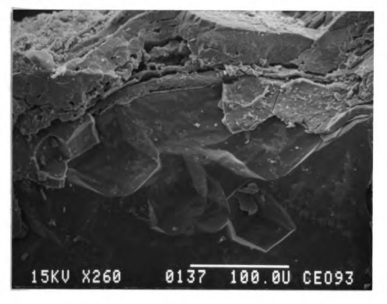


Figure 54. X-ray diffraction pattern of untreated clays

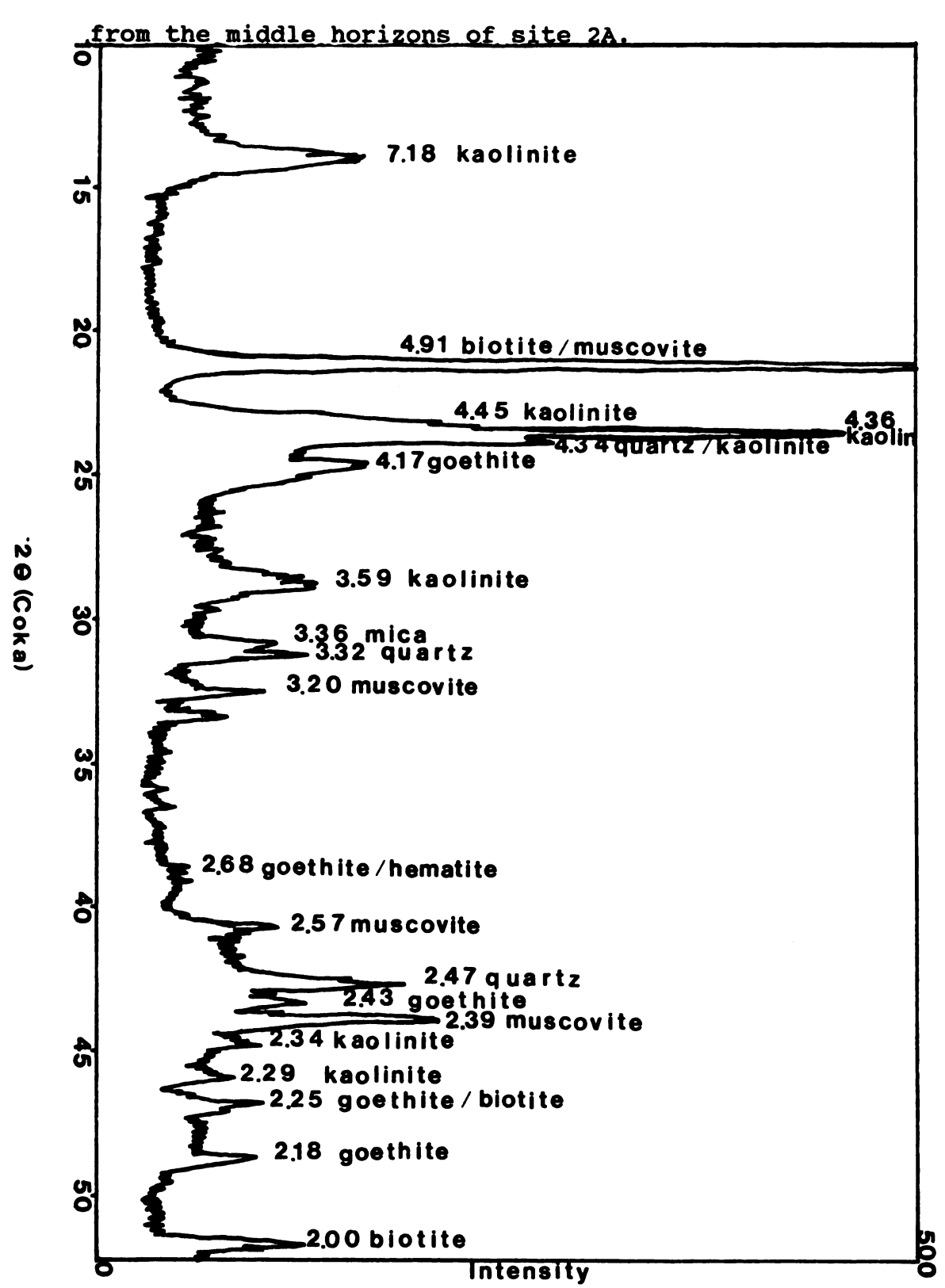


Figure 55. X-ray diffraction pattern of untreated clays from the saprolite of site 2B.

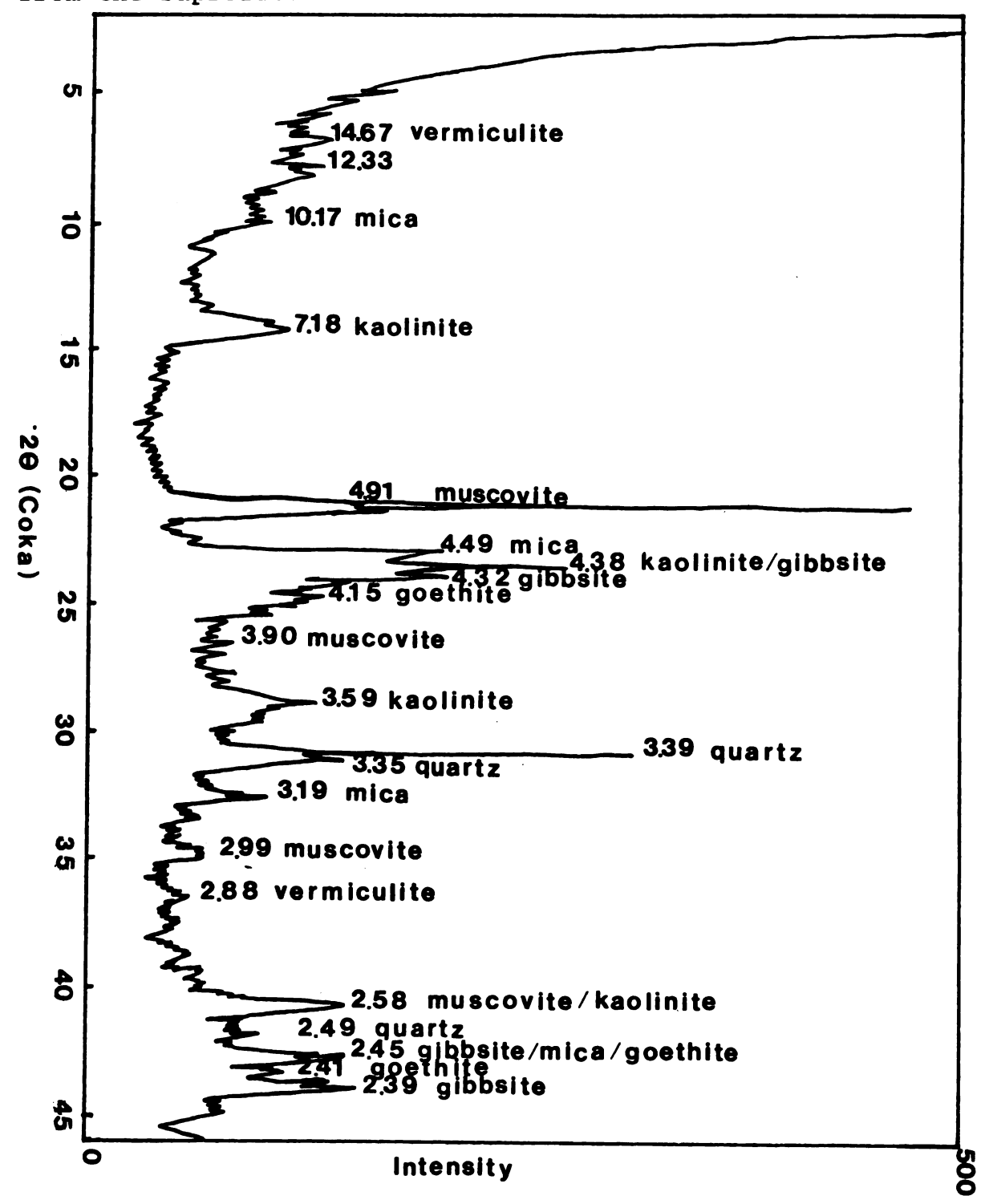


Figure 56. X-ray diffraction pattern of NaOH-treated clays from the middle horizons of site 17A.

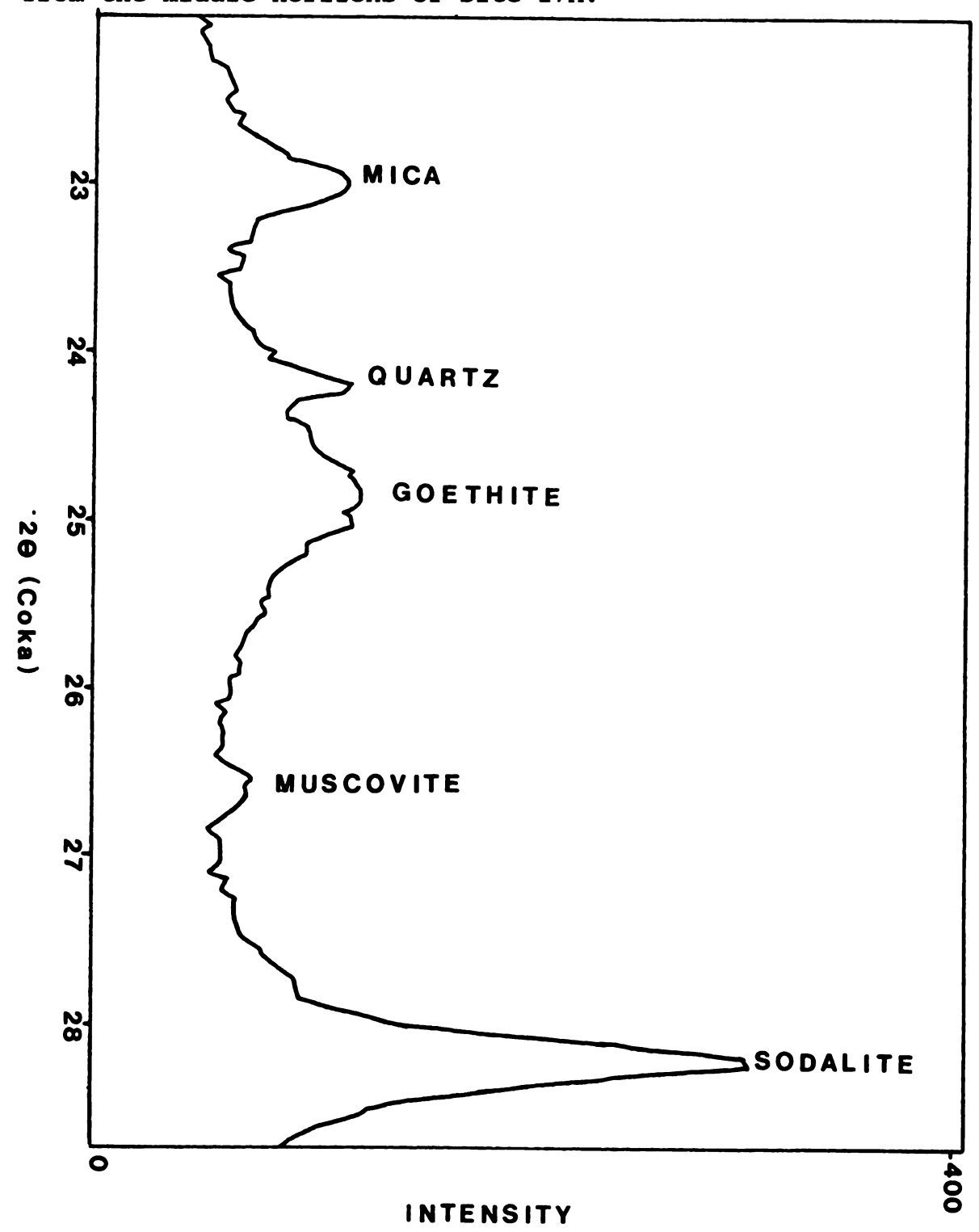


Figure 57. X-ray diffraction pattern of NaOH-treated clays from the saprolite of site 2A.

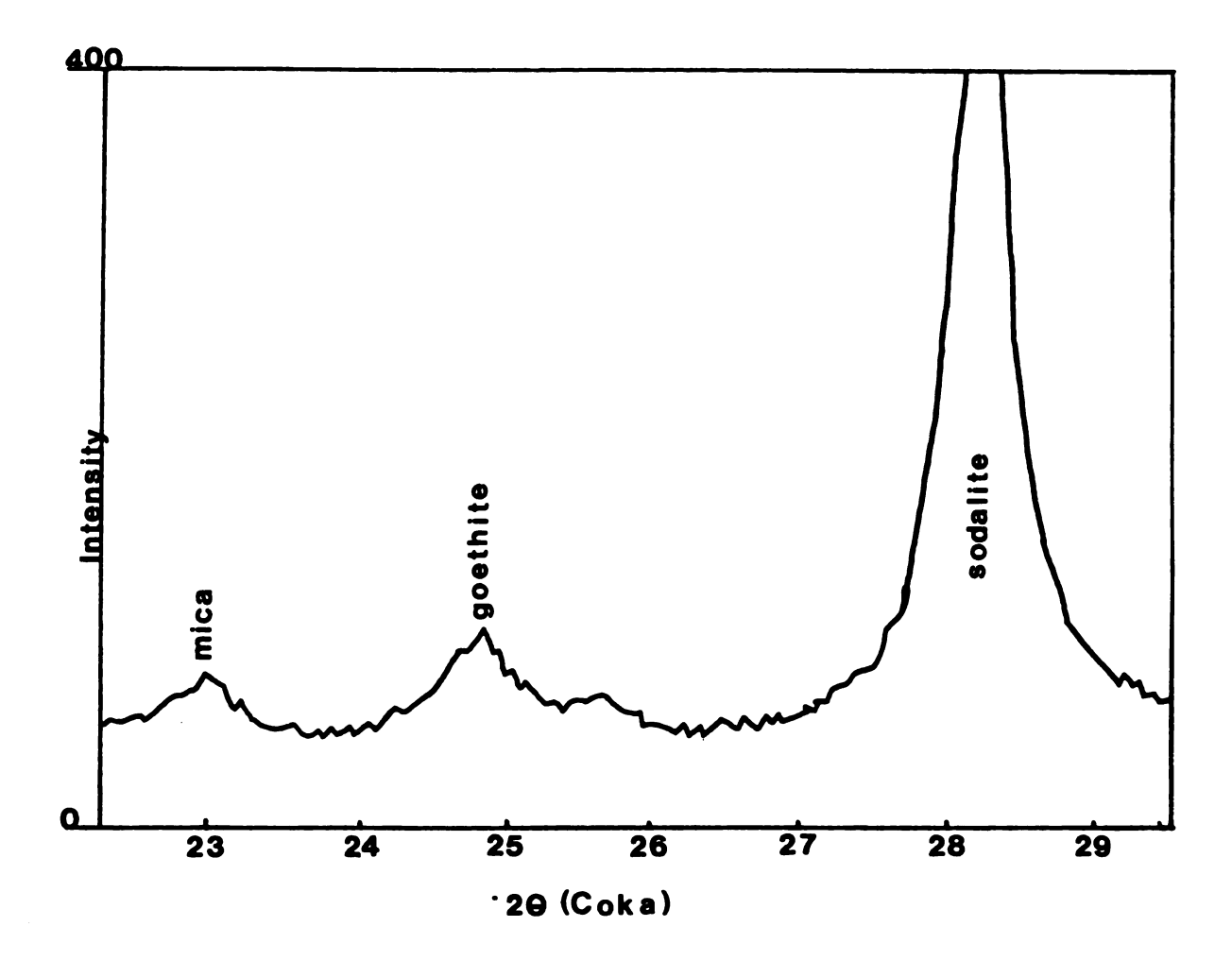


Figure 58. X-ray diffraction pattern of NaOH-treated clays from the middle horizons of site 36A.

#### 36A Middle Horizons NaOH

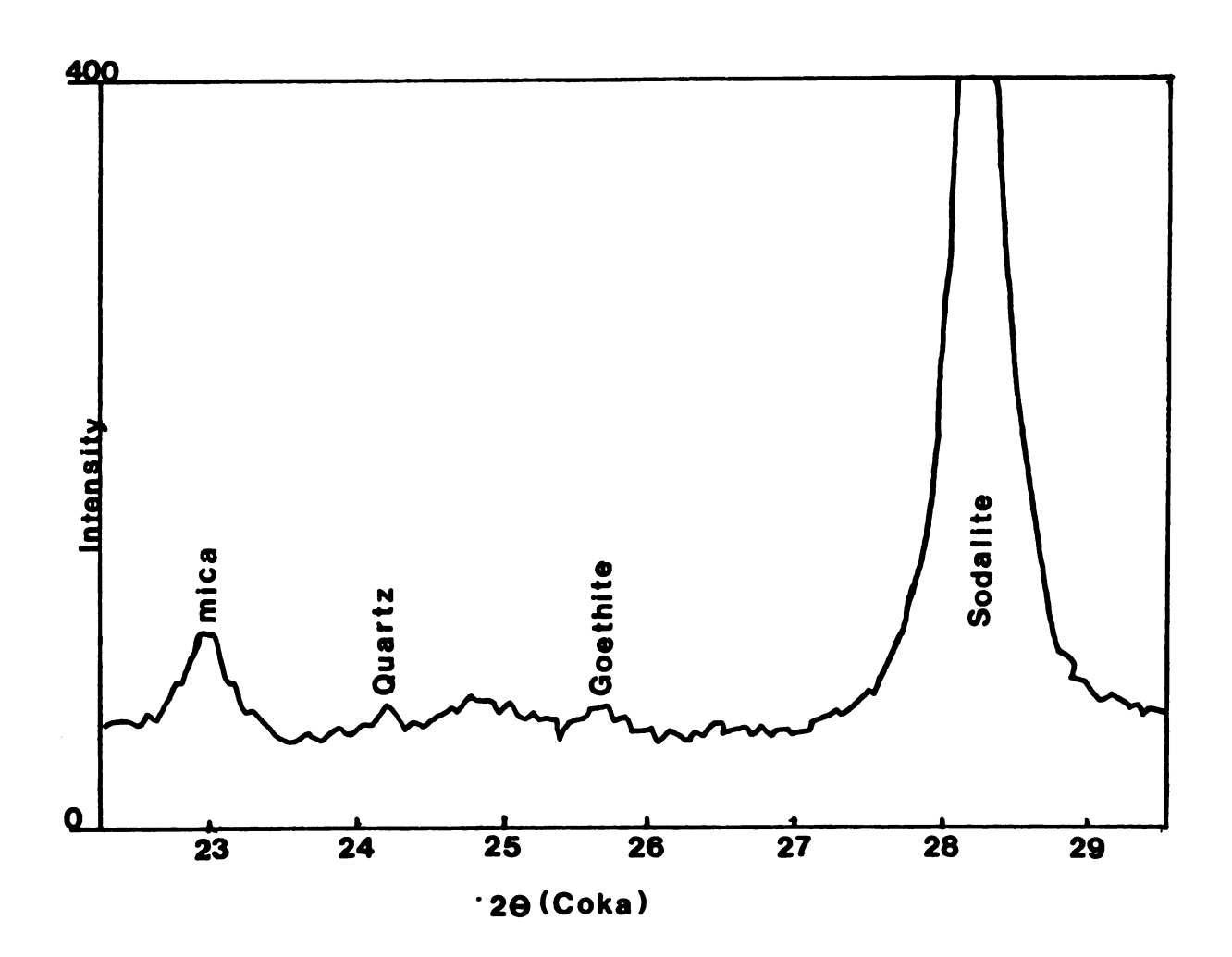


Figure 59. X-ray diffraction pattern of NaOH- and DCB-treated clays from the middle horizons of site 17A.

# 17A Middle Horizons DCB

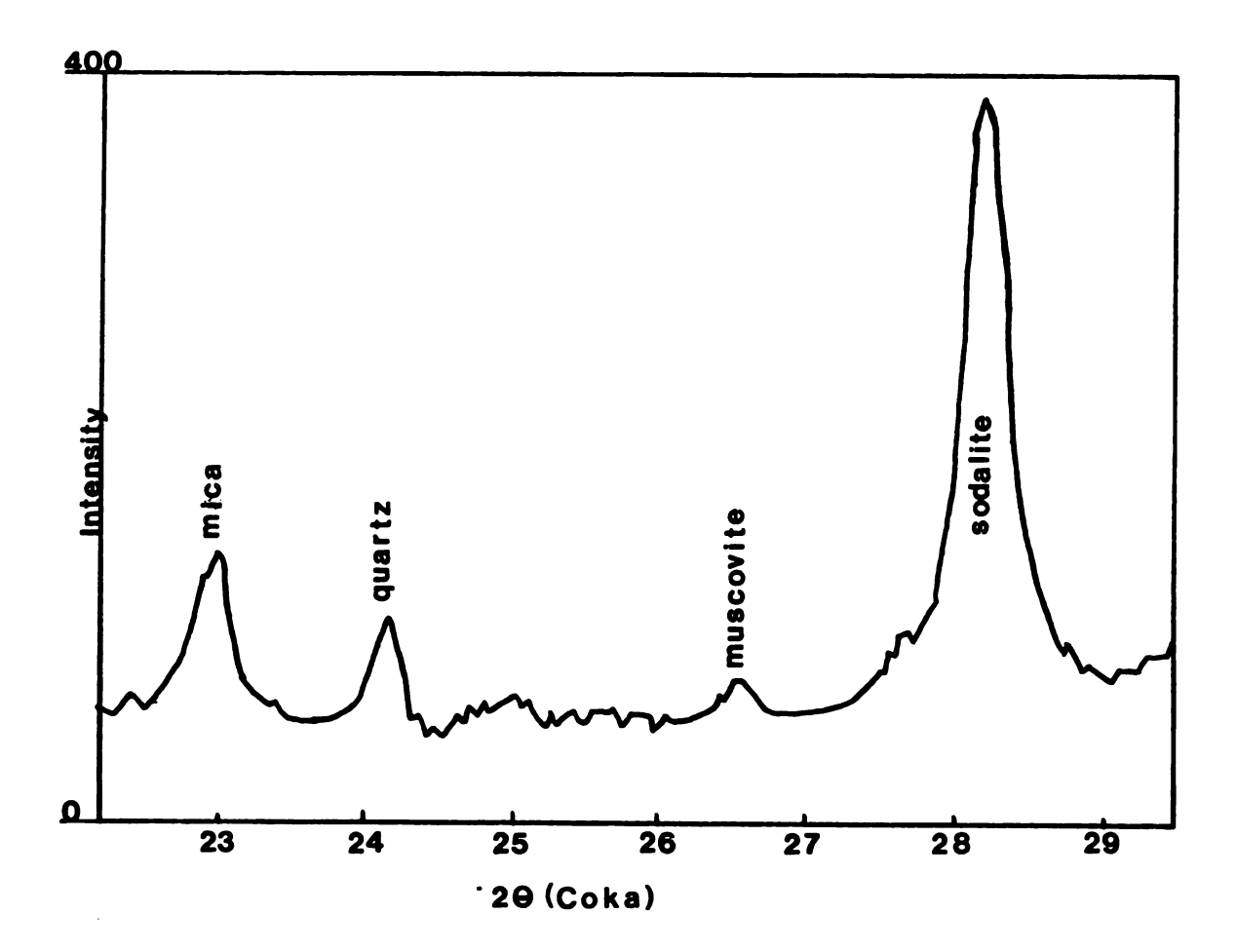


Figure 60. X-ray diffraction pattern of NaOH- and DCB-treated clays from the saprolite of site 2A.

# 2A Saprolite DCB

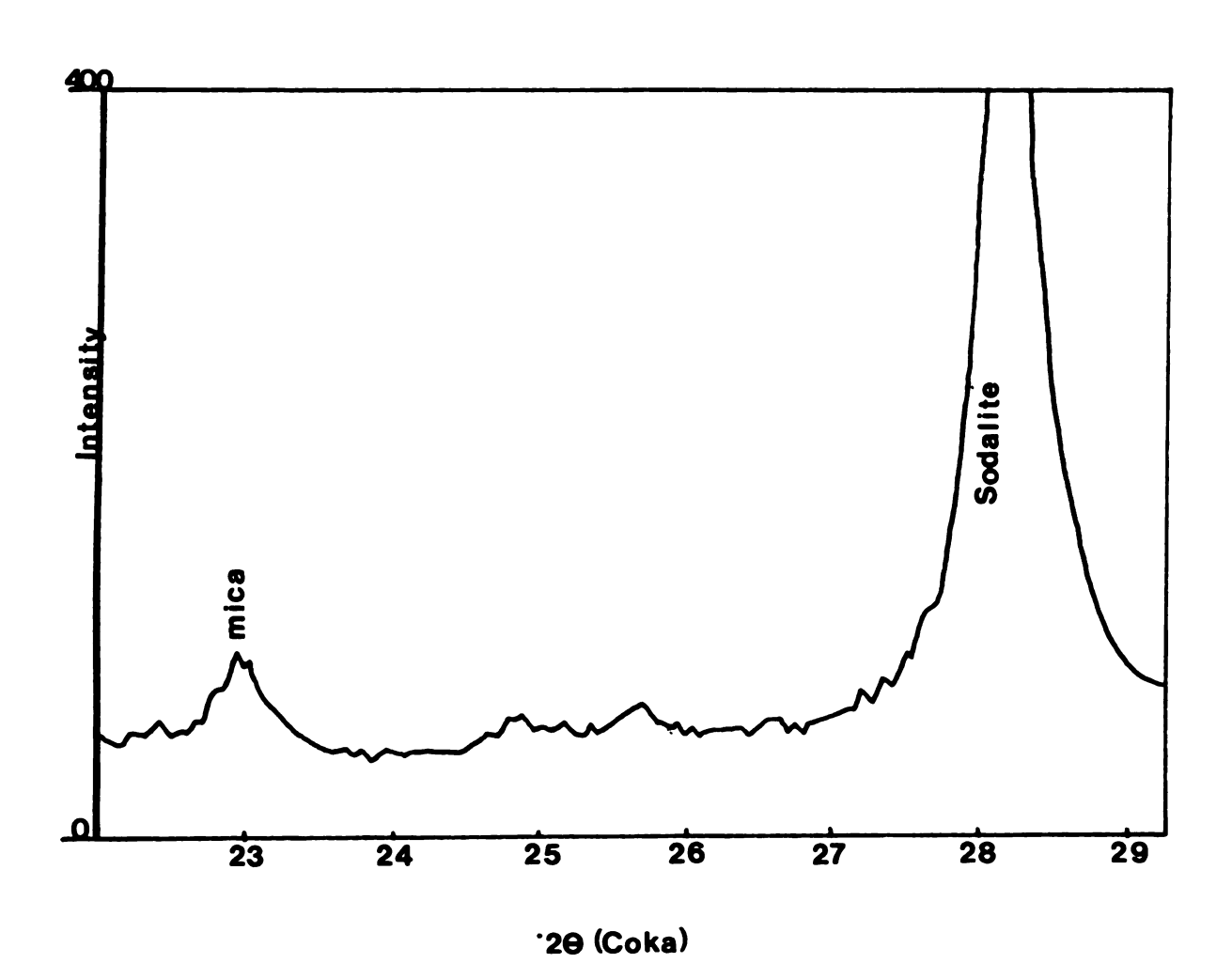


Figure 61. X-ray diffraction pattern of NaOH- and DCB-treated clays from the middle horizons of site 36A.

## 36A Middle Horizons DCB

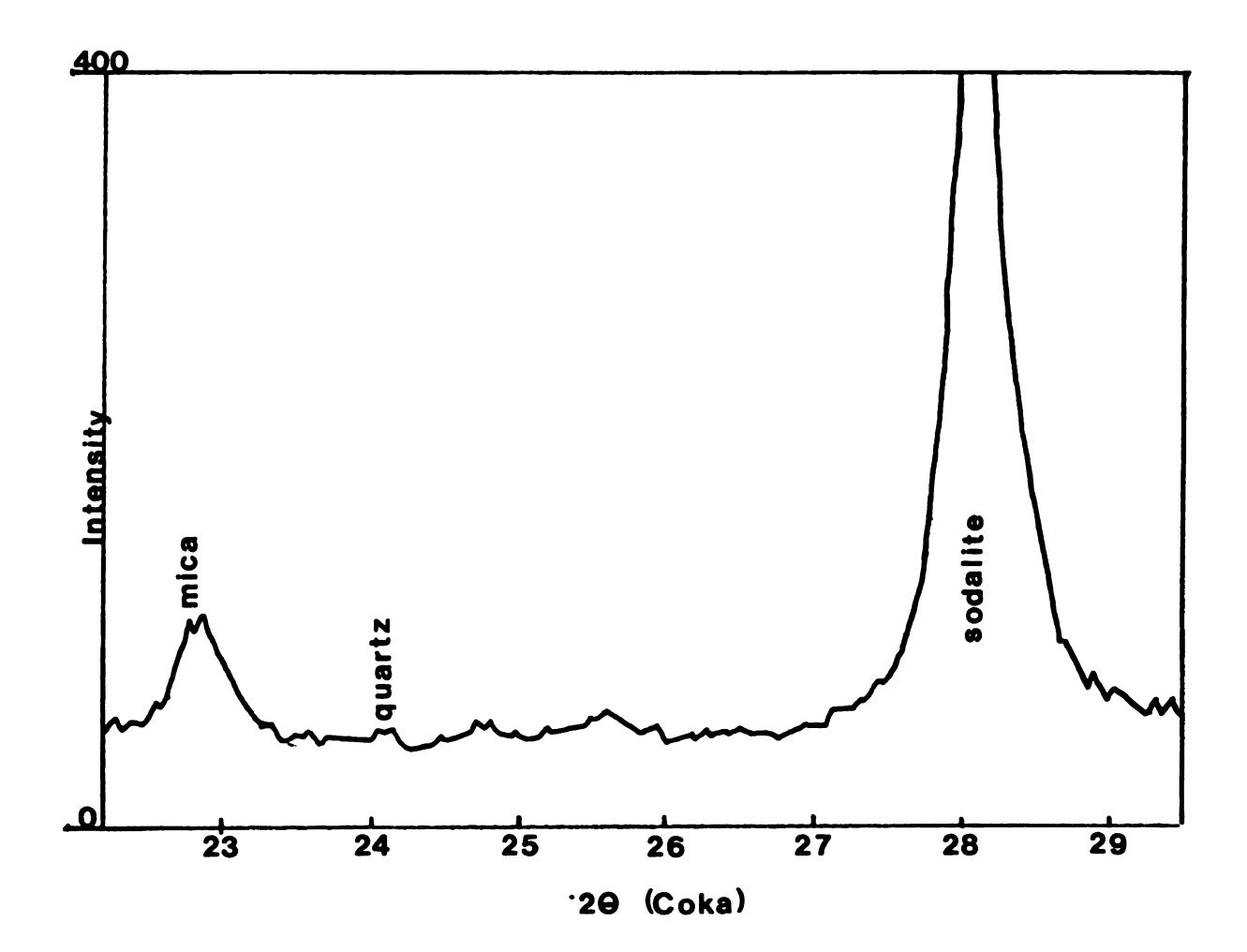


Figure 62. Redness ratings vs. aspect.

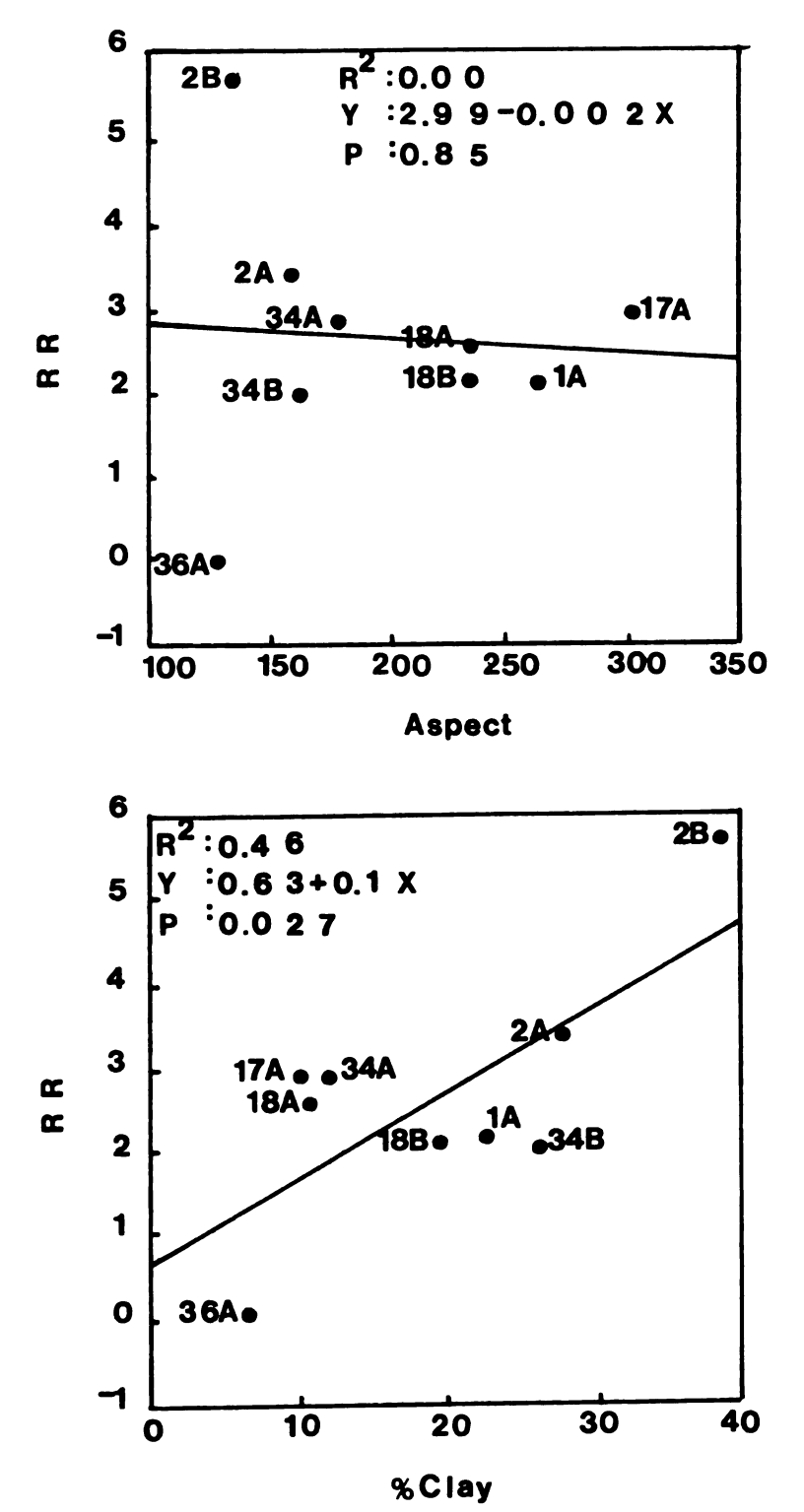
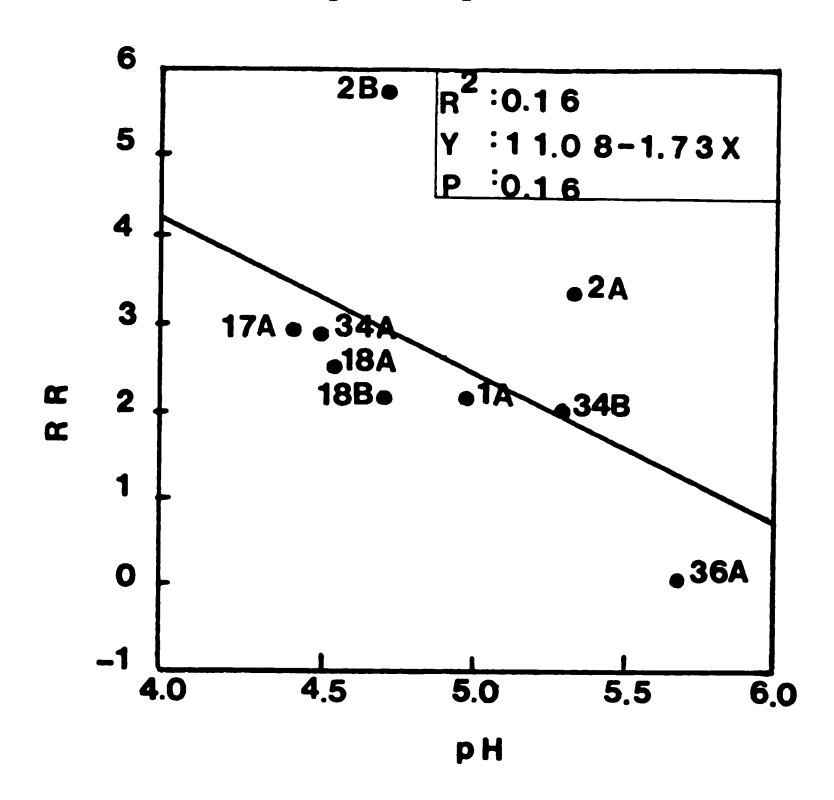


Figure 63. Redness ratings vs. clay.

Figure 64. Redness ratings vs. pH.



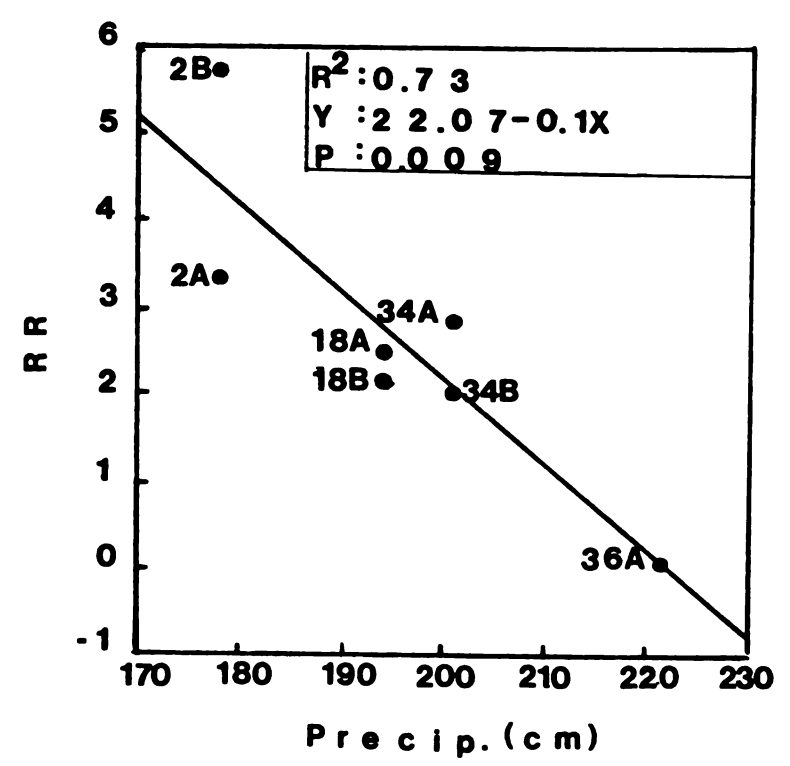
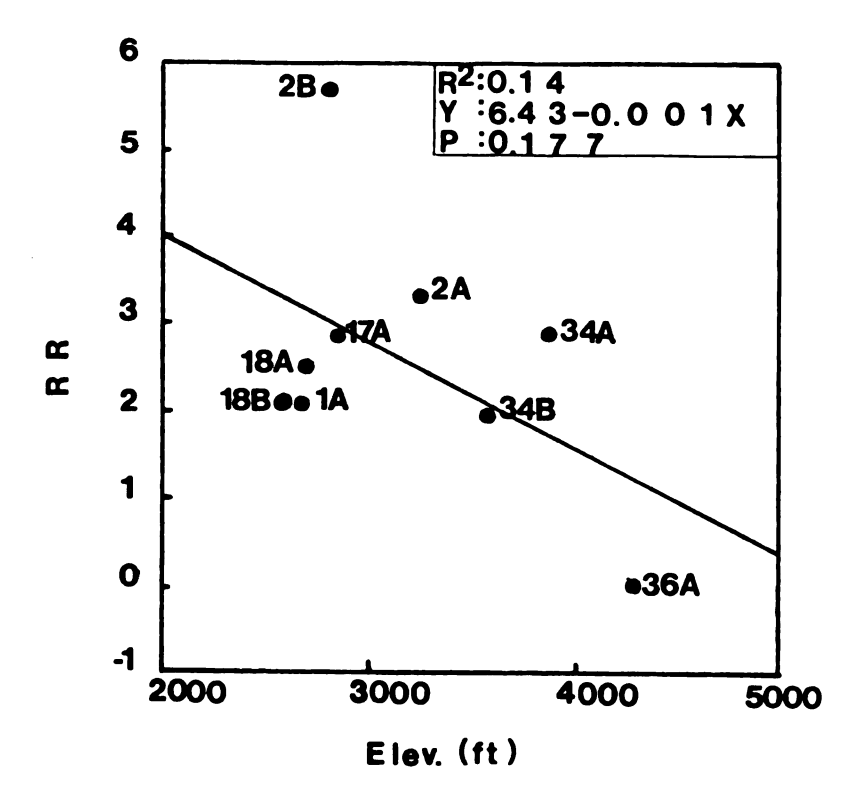


Figure 65. Redness ratings vs. mean annual precipitation.

Figure 66. Redness ratings vs. elevation.



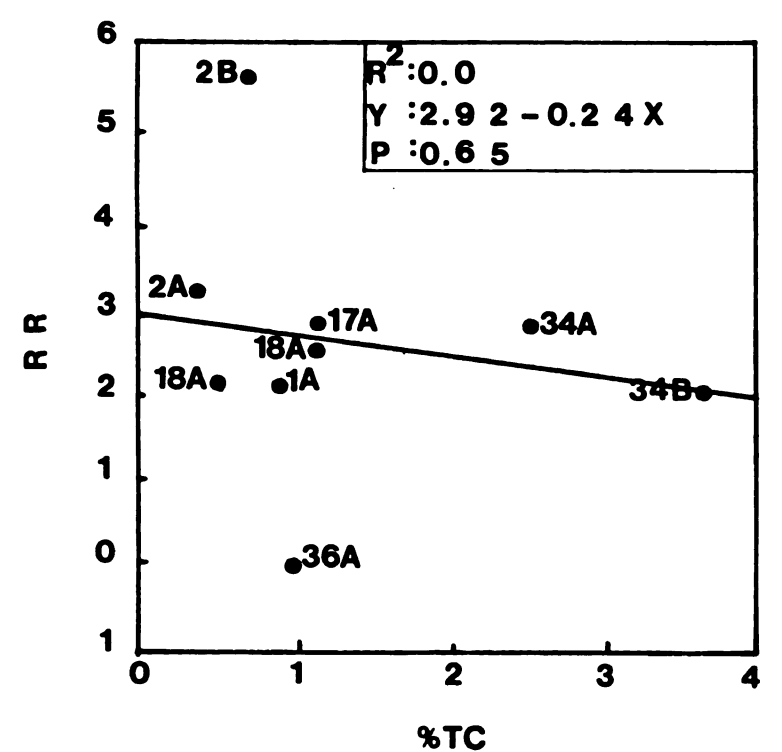
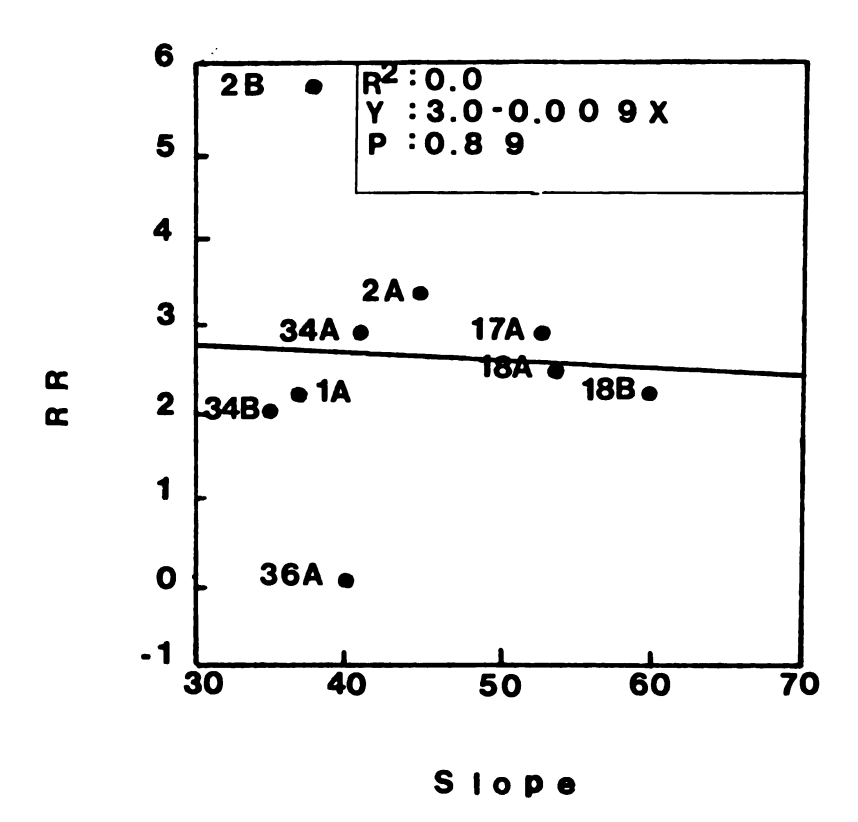


Figure 67. Redness ratings vs. total soil carbon.

Figure 68. Redness ratings vs. slope.



#### LIST OF REFERENCES

Allen, B. and Hajek, B., 1989, Mineral occurrences in soil environments. In: SSSA Book Series I: Minerals in soil environments, 2nd edition. Madison, WI: SSSA, p. 252-278.

Anand, R., and Gilkes, J., 1984a, Weathering of hornblende, plagioclase, and chlorite in meta-dolerite, Australia. Geoderma, v.34, p. 261-280.

Anand, R. and Gilkes, J. 1984b, Mineralogical and chemical properties of weathered magnetite grains from lateritic saprolite. Journal of Soil Science, v. 35, p. 559-567.

Bain, D., 1972, Oxidation of chlorites in soil clays and the effect on DTA curves. Nature, Physical Science, v. 238, p. 142-143.

Bain, D., 1977, The weathering of ferrigunous chlorite in a podzol from Argyllshire, Scotland. Geoderma, v. 17, p. 193-208.

Banfield, J. and Eggleton, R. 1988, Transmission electron microscope study of biotite weathering. Clays and Clay Minerals, v. 36, no. 1, p. 47-60.

Barshad, I., 1966, The effect of variation in precipitation on the nature of clay mineral formation in soils from acid and basic igneous rock. Proceedings of the International Clay Conference 1966 (Jerusalem), v. 1, p. 167-173.

Berner, R., 1978, Rate control of mineral dissolution under earth surface conditions. American Journal of Science, v. 278, p. 1235-1252.

Berner, R., 1981, Kinetics of weathering and diagenesis. In: Lasaga, A. and Kirkpatrick, R., (eds), Kinetics of geochemical processes. Mineralogical Society of America Reviews in Mineralogy, v. 8, p. 111-134.

Berner, R. and Schott, J. 1982, Mechanism of pyroxene and amphibole weathering II. Observations of soil grains. American Journal of Science, v. 282, p. 1214-1231.

Berner, R., Sjoberg, E., Velbel, M., and Krom, M., 1980, Dissolution of pyroxenes and amphiboles during weathering. Science, v. 207, p. 1205-1206.

Bouyoucos, G., 1962, Hydrometer method improved for making particle size analyses of soils. Agronomy Journal, v. 54, p. 464-465.

Brown, G. and Brindley, G., 1980, X-ray diffraction procedures for clay mineral identification. In: Brindley, G. and Brown, G. (eds), Crystal structures of clay minerals and their X-ray identification. London: Mineralogical Society of London, p. 305-360.

Browning, S., and Thomas, D., 1985, Soil map of Coweeta Hydrologic Laboratory. U. S. Department of Agriculture, Forest Service, Southeastern Forest Experiment Station.

Buol, S. and Weed, S., 1991, Saprolite-soil transformations in the piedmont and mountains of North Carolina. Geoderma, v. 51, p. 15-28.

Calvert, C., Buol, S., and Weed, S., 1980, Mineralogical characteristics and transformations of a rock-saprolite-soil profile in the North Carolina Piedmont II: Feldspar alteration products - Their transformation through the profile. Soil Science Society of America Journal, v. 44, p. 1104-1112.

Campbell, A., and Schwertmann, U., 1984, Iron oxide mineralogy of placic horizons. Journal of Soil Science, v. 35, p. 569-582.

Churchman, G., 1980, Clay minerals formed from micas and chlorites in some New Zealand soils. Clay Minerals, v. 15, p. 59-76.

Coleman, N., Le Roux, F. and Cady, I., 1963, Biotite-hydrobiotite-vermiculite in soils. Nature, v. 198, p. 409-410.

Correns, C. and Von Englehardt, W., 1938, Neue Untersuchungen über die Verwitterung des Kalifeldspates. Chemie der Erde, v. 12, p. 1-22.

Cressey, B., 1979, Electron microscopy of serpentinite textures. Canadian Mineralogist, v. 17, 741-756.

Embrechts, J. and Stoops, G., 1982, Microscopical aspects of garnet weathering in a humid tropical environment. Journal of Soil Science, v. 33, p. 535-545.

Fischer, W., 1971, Modellversuche zur Bildung und Auflösung von Goethit und amophen Eisenoxiden im Boden. Dissertation, T. U. München.

Fischer, W. and Schwertmann, U., 1975, The formation of hematite from amorphous iron(III) hydroxide. Clays and Clay Minerals, v. 23, p. 33-37.

Fitzpatrick, R., 1988, Iron compounds as indicators of pedogenic processes: Examples from the southern hemisphere. In: Stucki, J., et al. (eds), Iron in soils and clay minerals. New York: Reidel Publishing Co., p. 351-396.

Ghabru, S., Mermut, A., St. Arnaud, R., 1989, Characterization of garnets in a Typic Cryoboralf (Gray Luvisol) from Saskatchewan, Canada. Soil Science of America Journal, v. 53, no.2, p. 575-582.

Gilkes, R. and Little, I., 1972, Weathering of chlorite and some associations of trace elements in Permian phyllites in southeast Queensland. Geoderma, v. 7, p. 233-247.

Gilkes, J. and Suddhiprakarn, A., 1979, Magnetite alteration in deeply weathered adamellite. Journal of Soil Science, v. 30, p. 357-361.

Graham, R., Weed, S., Bowen, L. and Buol, S., 1989a, Weathering of iron-bearing minerals in soils and saprolite on the North Carolina Blue Ridge Front: I. Sand-size primary minerals. Clays and Clay Minerals, v. 37, no. 1, p. 19-28.

Graham, R. Weed, S., Bowen, L., and Buol, S., 1989b, Weathering of iron-bearing minerals in soils and saprolite of the North Carolina Blue Ridge Front: II. Clay Mineralogy. Clays and Clay Minerals, v. 37, no. 1, p. 29-40.

Graham, R., Daniels, R., and Buol, S., 1990a, Soil geomorphic relations on the Blue Ridge Front: I. Regolith types and slope processes. Soil Science Society of America Journal, v. 54, p. 1362-1367.

Graham, R., Daniels, R., and Buol, S., 1990b, Soil geomorphic relations on the Blue Ridge Front: II. Soil Characteristics and Pedogenesis. Soils Science Society of America Journal, v. 54, p. 1367-1377.

Haggerty, S., 1991, Oxide textures - A mini-atlas. In: Lindsley, D. (ed), Oxide Minerals: Petrographic and Magnetic Significance. Chelsea, MI: Mineralogical Society of America, Reviews in mineralogy, v. 25, p. 129-219.

Hansley, P., 1987, Petrologic and experimental evidence for the etching of garnets by organic acids in the Upper Jurassic Morrison Formation, northwestern New Mexico. Journal of Sedimentary Petrology, v. 57, no. 4, p. 666-681.

Hatcher, R., 1980, Geologic map of the Coweeta Hydrologic Laboratory, Prentiss Quadrangle, North Carolina. State of North Carolina, Department of Natural Resources and Community Development.

Hatcher, R., 1988, Bedrock geology and regional geologic setting of Coweeta Hydrologic Laboratory in the Eastern Blue Ridge. In: Swank, W. and Crossley, D. (eds), Forest hydrology and ecology at Coweeta, Ecological Studies 66. New York: Springer-Verlag, p. 81-92.

Helgeson, H., 1971, Kinetics of mass transfer among silicates and aqueous solutions. Geochimica et Cosmochimica Acta, v. 35, p. 421-469.

Helgeson, H., 1972, Kinetics of mass transfer among silicates and aqueous solutions: Correction and clarification. Geochimica et Cosmochimica Acta, v. 36, p. 1067-1070.

Joint Committee on Powder Diffraction Standards (eds), 1980, Mineral powder diffraction file: Data book. JCPDS, p. 364, 406, 491, 492, 582, 590, 667-669, 754-756, 898. JCPDS: Swarthmore, PN.

Joint Committee on Powder Diffraction Standards (eds), 1980, Mineral powder diffraction file: Search Manual. JCPDS: Swarthmore, PN., 467pp.

Kämpf, N. and Schwertmann, U., 1982a, The 5-M-NaOH concentration treatment for iron oxides in soils. Clay and Clay Minerals, v. 30, no. 6, p. 401-408.

Kämpf, N. and Schwertmann, U., 1982b, Goethite and hematite in a clino-sequence in southern Brazil and their application in classification of kaolinitic soils. Geoderma, v. 29, p. 27-39.

Langmuir, D., 1971, Particle size effect on the reaction goethite = hematite + water. American Journal of Science, v. 271, p. 147-156.

Lasaga, A., and Blum, A., 1986, Surface chemistry, etch pits and mineral water reactions. Geochimica et Cosmochimica Acta, v. 50, p. 2363-2379.

Luce, R., Bartlett, R. and Parks, G., 1972, Dissolution kinetics of magnesium silicates. Geochimica et Cosmochimica Acta, v. 36, p. 35-50.

Mehra, O. and Jackson, M., 1960, Iron oxide removal from soils and clays by a dithionite-citrate-bicarbonate system buffered with sodium bicarbonate. Clays and Clay Minerals, v. 7, 317-327.

Meunier, A. and Velde, B., 1979, Biotite weathering in granites of western France. In: Mortland, M. and Farmer, V., (eds), Proceedings of the International Clay Conference, Oxford (1978), p. 405-415.

Mohr, E., von Baren, F. and Schuylenborgh, J., 1972, Tropical soils, 3rd edition, p. 433-450.

Morris, R. 1980, A textural and mineralogical study of the relationship of iron ore to banded iron-formation in the Hamersley Iron Province of Western Australia. Economic Geology, v. 75, p. 184-209.

Nahon, D., Janot, C., Karpoff, A., Paquet, H. and Tardy, Y., 1977, Mineralogy, petrography, and structures of iron crusts (ferricretes) developed on sandstones in the western part of Senegal. Geoderma, v. 19, p. 263-277.

Nesse, W., 1986, Introduction to optical mineralogy. Oxford: Oxford University Press, 325pp.

Schwertmann, U., 1971, Transformations of hematite to goethite in soils. Nature, v. 232, p. 624-625.

Schwertmann, U., 1985, The effect of pedogenic environments on iron oxide minerals. In: SSSA Advances in Soil Sciences, v.I (1985), p. 171-200.

Schwertmann, U., 1988, Occurrence and formation of iron oxides in various pedoenvironments. In: Stucki, J., et al. (eds), Iron in soils and clay minerals. New York: Reidel Publishing Co., p. 267-308.

Schwertmann, U. and Lentze, W., 1966, Bodenfarbe und Eisenoxidform. Z. Pflanzenern., Düng., Bodenkunde, v. 115, p.209-214.

Schwertmann, U. and Murad, E., 1983, The effect of pH on the formation of goethite and hematite from ferrihydrite. Clays and Clay Minerals, v. 31, p. 277-284.

Schwertmann, U., Schulze, D., and Murad, E., 1982, Identification of ferrihydrite in soils by dissolution kinetics, differential X-ray diffraction and Mössbauer spectroscopy. Soil Science Society of America Journal, v. 46, p. 869-875

Schwertmann, U. and Taylor, R., 1989, Iron oxides. In: SSSA Book Series I: Minerals in soil environments, 2nd edition. Madison, WI: SSSA, p. 379-438.

Soil Conservation Service, 1967, Soil Survey laboratory methods and procedures for collecting soil samples: Soil Survey Investigations Report No. 1, U. S. Department of Agriculture, 50pp.

Swank, W. and Crossley, I., 1988, Introduction and site description. In: Swank, W. and Crossley, D. (eds), Forest hydrology and ecology at Coweeta, Ecological Studies 66. New York: Springer-Verlag, p. 3-15.

Swift, L., Cunningham, G., and Douglass, J., 1988, Climatology and hydrology. In: Swank, W. and Crossley, D. (eds), Forest hydrology and ecology at Coweeta, Ecological Studies 66. New York: Springer-Verlag, p. 35-55.

Tazaki, K. and Fyfe, W., 1987, Primitive clay precursors formed on feldspar. Canadian Journal of Earth Science, v. 24, p. 506-527.

Taylor, R., 1987, Non-silicate oxides and hydroxides. In: Newman, A. (ed), The Chemistry of Clays and Clay Minerals. Essex: Longman Group LTD., p. 129-201.

Tchoubar, C., 1965, Formation de la kaolinite à partir d'albite alterée par l'eau à 200°C. Étude en microscope et diffraction electroniques. Le Bulletin de la Société Française et de Minéralogie Cristallographie, v. 88, p. 483-518.

Torrent, J. and Schwertmann, U., 1987, Influence of hematite on the color of red beds. Journal of Sedimentary Petrology, v. 57, no. 4, 682-686.

Torrent, J., Schwertmann, U., Fechter, H., and Alferez, F., 1983, Quantitative relationships between soil color and hematite content. Soil Science, v. 136, p. 354-358.

Torrent, J., Schwertmann, U. and Schulze, D., 1980, Iron oxide mineralogy of some soils of two river terrace sequences in Spain. Geoderma, v. 23, p. 191-208.

Velbel, M., 1984a, Natural weathering mechanisms of almandine garnet. Geology, v. 12, p. 631-634.

Velbel, M., 1984b, Mineral transformations during rock weathering, and geochemical mass-balances in forested watersheds of the Southern Appalachians. Ph. D. dissertation, Yale University: unpublished, 175pp.

Velbel, M. 1985, Geochemical mass balances and weathering rates in forested watersheds of the southern Blue Ridge. American Journal of Science, v. 285, p. 904-930.

Velbel, M., 1989, Weathering of hornblende to ferruginous products by a dissolution-reprecipitation mechanism: Petrography and stoichiometry. Clays and Clay Minerals, v. 37, no. 6, p. 515-524.

Velbel, M., 1993, Formation of protective surface layers during silicate-mineral weathering under well-leached oxidized conditions. American Mineralogist, v. 78, p. 405-414.

Walker, G., 1949, The decomposition of biotite in the soil. Mineralogy Magazine, v. 28, p. 693-703.

Wendt, A., D'Arco, P., Goffé, B., and Oberhänsli, R., 1993, Radial cracks around  $\alpha$ -quartz inclusions in almandine: Constraints on the metamorphic history of the Oman Mountains. Earth and Planetary Science Letters, v. 114, p. 449-461.

Wicks, F. and Whittaker, E., 1977, Serpentine textures and serpentinization. Canadian Mineralogist, v. 15, p. 446-458.

Wilson, M., 1966, The weathering of biotite in some Aberdeenshire soils. Mineralogy Magazine, v. 35, p. 1080-1093.

Wollast, R., 1967, Chemical weathering of some primary rock-forming minerals. Soil Science, v. 119, p. 349-355.

Yapp, C., 1983, Effects Of ALOOH-FeOOH solid solution on goehtite-hematite equilibrium. Clays and Clay Minerals, v. 31, p. 239-240

